Measurement of the Total Photoproduction Cross Section at the Electron Proton Collider HERA at $W_{\gamma p}$ of 200 GeV

Inaugural–Dissertation

zur
Erlangung der philosophischen Doktorwürde
vorgelegt der
Philosophischen Fakultät II
der

Universität Zürich

von

Hans Peter Beck

aus Neuenkirch LU und Menznau LU

begutachtet von Prof. Dr. Peter Truöl
und Prof. Dr. Ulrich Straumann

Zürich 1996

Für Zdena,
Nastassja und Vanessa

Zusammenfassung

Mit dem H1 Detektor an der Hadron–Elektron–Ring–Anlage HERA am Deutschen Elektronen Synchrotron DESY in Hamburg wurde der totale Wirkungsquerschnitt (Reaktionsstärke) für Photon–Proton Reaktionen bei einer Schwerpunktsenergie von 200 GeV gemessen. Die Messung beruht auf Daten, die während einer kurzen Periode am Ende der Datennahme 1994 unter speziellen Bedingungen aufgezeichnet wurden.

Kapitel 1 gibt Einblick in die Physik von hochenergetischen Elektron–Proton Reaktionen und zeigt den Zusammenhang zur Photoproduktion, welche es erlaubt, Photon–Proton Reaktionen am Speicherring HERA zu Untersuchen. Es zeigt sich, dass bei hohen Energien Photonen, die Quantenteilchen des Lichts, eine reichhaltige Struktur aufweisen, die derjenigen von Hadronen ähnelt.

Kapitel 2 & 3 erklären die technischen Komponenten des HERA Speicherrings und des H1 Detektors.

Messungen mit grossen Apparaten wie der H1 Detektor können dann und nur dann erfolgreich durchgeführt werden, wenn die charakteristischen Eigenschaften der einzelnen Komponenten hinreichend genau bekannt sind. Kapitel 4 zeigt deshalb, wie das Verständnis für den z–Vertex Trigger, eine Vorrichtung zur schnellen, totzeitfreien Erkennung von Elektron–Proton Kollisionen, aus den Daten gewonnen wurde und für die kollaborationsweite Nutzung zugänglich gemacht wurde.

Die eigentliche Messung des totalen Wirkungsquerschnitts ist im letzten Kapitel beschrieben. Bei einer mittleren Schwerpunktsenergie von 200 GeV wurde ein Wert von

$$\sigma_{\text{tot}}^{\gamma p} = 165 \pm 2 \pm 10 \ \mu\text{b}$$

ermittelt. Wobei der erste Fehler rein statistischer Natur ist und der zweite eine Schätzung der systematischen Fehler angibt. Eine detailierte Analyse der Daten in geeigneten kinematischen Bereichen ermöglichte eine Unterteilung der Photoproduktionsdaten in elastische, Photon diffraktive, Proton diffraktive, doppelt diffraktive und nicht diffraktive Ereignisse.

Abstract

The H1 detector located at the hadron–electron–ring–accelerator HERA at the Deutsches Elektronen Synchrotron DESY in Hamburg, Germany was used to measure the total cross–section of photon–proton reactions at a center of mass energy of 200 GeV. The measurement relies on data taken using special conditions during a short period near the end of the 1994 data taking period.

Chapter 1 gives an introduction into the physics of high energy electron–proton reactions and reveals the relation to photoproduction, which allows to study photon–proton reactions at the HERA storage ring. It points out, that at large energies, photons, the quantum particles of light, reveal a rich structure resembling the one of hadrons.

Chapter 2 & 3 explain the technical components of the HERA storage ring and the H1 detector.

Measurements performed with a large scale apparatus, such as the H1 detector are then and only then successful if the individual sub–components are adequately known. For that reason, Chapter 4 explains how the characteristics of the z–Vertex trigger, a device for fast, dead time free identification of electron–proton reactions, were deduced from the data and how this knowledge has been made available for use within the whole H1 collaboration.

The measurement of the total cross section is explained in chapter 5. For an average center of mass energy of 200 GeV a value of

$$\sigma_{\text{tot}}^{\gamma p} = 165 \pm 2 \pm 10 \ \mu\text{b}$$

has been obtained. The first error is statistical, the second an estimate of the systematical errors. A detailed analysis of the data in adequate kinematical regions enabled a decomposition of the total cross section into elastic, photon diffractive, proton diffractive, double diffractive and non–diffractive contributions.

Contents

List of Figures

List of Tables

Chapter 1

Physics of high energy electron proton collisions

1.1 Introduction

The HERA collider provides an unique opportunity to study the final state of both photoproduction and deep inelastic scattering (DIS)[†] interactions at high energy and small Bjorken–x. 27.5 GeV electrons collide on 820 GeV protons, yielding a center of mass energy $\sqrt{s}$ of 300 GeV. This allows to study DIS interactions for Bjorken–x values down to $\sim 10^{-4}$ [1, 2] and photoproduction collisions at center of mass energy of up to ~ 250 GeV [3, 4, 5].

At HERA, weak interactions processes ($W^{\pm}$ and Z^0 exchange), albeit of high physical interests, play only a minor rôle due to the Q^{-4} dependence of the cross section, with respect to the huge bulk of photoproduction events, in which the electron scatters through small (large) angles, emits a quasi–real (highly virtual) photon, which then interacts with the proton. Only at very high momentum transfer ($Q^2 \sim 10^4$ GeV^2) weak interactions become visible [6].

Traditionally, the process of photon proton interactions is divided into two separate classes depending on the virtuality Q^2 of the photon: photoproduction (low Q^2) and DIS (high Q^2). In the latter, the proton interacts with highly virtual photons with Q^2 typically larger than a few GeV^2. The main reason for such a distinct separation is the different theoretical approach to describe photoproduction and DIS. DIS is considered as a tool, where the point–like virtual photon directly probes the partonic contents of the proton, which is described by perturbative quantum chromodynamics (pQCD). On the other hand, photoproduction has turned out to be very similar to hadron–hadron collisions

---

[†]Commonly used abbreviations can be found in the index on page 128.

showing the features of soft low–transverse momentum $p_\perp$ processes, such as elastic and diffractive hadronic final state production [7, 8] and shadowing on nuclear targets [9, 10]. This is usually described with the vector meson dominance model (VMD) [11], where the photon is assumed to fluctuate into a vector meson before interacting with the proton. Additional mechanism, such as the direct coupling of the photon to quarks in the proton and pointlike contributions, where the photon splits in a $q\bar{q}$ pair are needed to accommodate to finer details as measured in data [4]. These are usually referred as generalized VMD models (gVMD) [12].

The measurement of cross sections always gave inputs in the understanding of the principles of particle reactions and thus provides a glimpse into the deeper structure of matter. Measuring the cross section of photoproduction events at HERA reveals therefore an insight into the contents of the photon and of the proton respectively.

The photon, as originated in the early times of quantum mechanics, was first regarded as a structureless particle, with which a very successful prediction of spectral lines was possible and many processes, such as the photoelectric effect or Compton scattering could be described. As the scale of available energies increased, it was found, that through an interaction with the Coulomb field, the photon can materialize into a pair of electrons, $\gamma \leftrightarrows e^+e^-$. This phenomenum was the earliest manifestation of photon structure. A physical particle contains not only its bare particle state, but also contributions from all possible states coupled to it through interactions. With further increasing of impact energies into the multi GeV range, even more degrees of freedom of the so defined inner structure of the photon can be excited and a hadronic behavior of the photon, among its bare electromagnetic coupling, shows up.

The striking evidence for an universal rise of the total cross sections with impact energy for hadron–hadron collisions, and therefore expected also for photon–proton collisions, as nicely demonstrated by Donnachie and Landshoff [13], directly opens the way back to an old interpretation within the Regge theory [14, 15] using the language of pomeron exchange [16]. This started a rush for the embedding of the old pomeron language into the actual framework of pQCD.

1.2   Kinematics

The high energy electron proton collision process $e + p \rightarrow l + X$ as produced at HERA is illustrated in fig 1.1. e and p are the incoming electron and proton, the scattered lepton and the hadronic final state are denoted by l and X. Only two independent variables are needed to describe the overall event kinematics, e.g. measuring energy and angle of the scattered lepton determines all other global variables. This becomes evident after some

variables have been defined: $P_e \equiv (E_e, \mathbf{p_e})$ and $P_l \equiv (E_l, \mathbf{p_l})$ are the four-vectors of the incoming and scattered lepton and $P \equiv (E_P, \mathbf{p_P})$ that of the incoming proton. The sum of all four-vectors in the hadronic final state is given as $P_H \equiv (E_H, \mathbf{p_H})$. All four-vectors given are defined in the H1 laboratory frame (lab), where the incoming proton defines the $+z$–axis. The angle ϑ of the scattered lepton is measured between the proton line ($+z$–axis) and the scattered lepton. The scattering angle ϑ of a lepton which hardly interacts with the proton is therefore close to π. The total invariant mass squared (s) of the system is given as the square of the sum of the four-vectors of the incoming or outgoing particles:

$$s = (P_e + P)^2 = (P_l + P_H)^2 \cong 4 \cdot E_e E_P \tag{1.1}$$

The '$\cong$' sign means that the particle masses are neglected which is a good approximation at HERA energies.
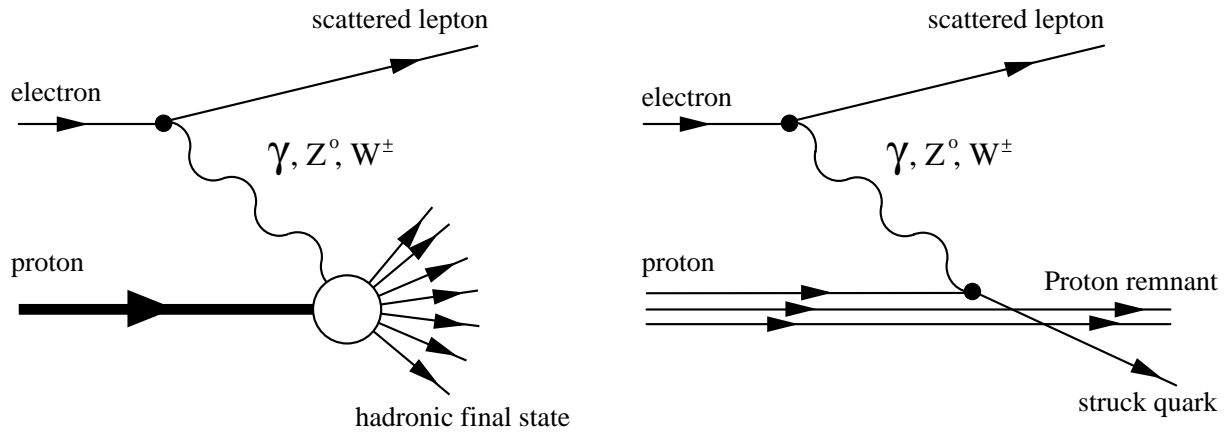
Figure 1.1: Deep inelastic scattering at HERA.
left: without further assumptions on a underlying proton structure.
right: in the quark parton model.

It is convenient to use Lorentz–invariant variables (x,y and Q^2). Their definitions and the relation to the above defined frame dependent variables are:

$$Q^2 \equiv -q^2 \equiv -(p_e - p_l)^2 = -(P - P_H)^2 \quad \overset{\text{lab}}{=} \quad 4E_e E_l \cos^2 \frac{\vartheta}{2} \tag{1.2}$$

$$y \equiv \frac{q \cdot P}{p_e \cdot P} = \frac{2P \cdot q}{s} \quad \overset{\text{lab}}{=} \quad 1 - \frac{E_l}{Ee} \sin^2 \frac{\vartheta}{2} \tag{1.3}$$

$$x \equiv \frac{Q^2}{2P \cdot q} \quad \overset{\text{lab}}{=} \quad \frac{E_e E_l \cos^2 \frac{\vartheta}{2}}{E_p(E_e - E_l \sin^2 \frac{\vartheta}{2})} \tag{1.4}$$

The four–vector $q = (p_e - p_l)$ is space–like ($q^2 < 0$), which ensures the momentum transfer variable Q^2 to be positive. x is the dimensionless Bjorken scaling variable which measures

in the parton model the fraction of the proton's momentum carried by the struck quark. y, also dimensionless, measures the relative energy loss of the electron in the rest frame of the proton. The right hand side of above equations is valid in the H1 laboratory frame, after neglecting all particle masses, $E_e, E_p \gg m_e, m_p$. The left hand side, of course, are exact definitions, valid in any frame.

x, y and Q^2 are not independent, they obey following relation:

$$Q^2 = xys \tag{1.5}$$

It is easy to show, that x and y are always in the range $0 \le x, y \le 1$. Another important quantity is the invariant mass W of the hadronic system:

$$W^2 \equiv (q + P)^2 = Q^2 \frac{1-x}{x} + m_p^2 \quad \overset{\text{lab}}{=} \quad m_p^2 + 4 \cdot \left[E_P E_e - E_P E_l \sin^2 \frac{\vartheta}{2} - E_e E_l \cos^2 \frac{\vartheta}{2} \right] \tag{1.6}$$

with m_p being the protons rest mass. W^2 ranges from m_p^2 to s.

1.3   Cross sections and structure functions

The inclusive deep inelastic cross section for neutral current electron proton scattering as a function of two of the above defined kinematical variables (e.g. x and Q^2) can be written, using three structure functions F_1, F_2 and F_3 depending on x and Q^2, as follows [6]:

$$\frac{\mathrm{d}^2 \sigma_{NC}(e^\pm p)}{\mathrm{d}x\, \mathrm{d}Q^2} = \frac{4\pi\alpha^2}{xQ^4} \left[y^2 x F_1(x, Q^2) + (1-y) F_2(x, Q^2) \mp \left(y - \frac{y^2}{2} \right) x F_3(x, Q^2) \right] \tag{1.7}$$

It is very common to introduce a fourth structure function F_L which is a linear combination of F_1 and F_2:

$$F_L \equiv F_2 - 2x F_1 \tag{1.8}$$

In the standard parton model, with charged, massless spin–1/2 partons (no gluons) and no intrinsic transverse momenta of the partons, $F_L(x, Q^2)$ vanishes (Callan–Gross relation [17]). Higher order QCD effects change this relation and F_L gets proportional to α_s, the strong coupling constant of QCD.

A measurement of F_L therefore probes directly the gluonic content of the proton. Rewriting the cross section yields:

$$\frac{\mathrm{d}^2 \sigma_{NC}(e^\pm p)}{\mathrm{d}x\, \mathrm{d}Q^2} = \frac{2\pi\alpha^2}{xQ^4} \left[\left(1 + (1-y)^2 \right) F_2 - y^2 F_L \mp (2y - y^2) x F_3(x, Q^2) \right] \tag{1.9}$$

The structure functions are in the standard parton model calculated as the probability of finding a quark (antiquark) with momentum fraction x of the proton times a coupling to the exchange boson summed over all flavors in the proton:

$$F_1^{L,R}(x, Q^2) = \frac{1}{2x} \cdot F_2^{L,R}(x, Q^2) \tag{1.10}$$

$$F_2^{L,R}(x, Q^2) = \sum_{\text{flavors}} \left[xq_f(x, Q^2) + x\bar{q}_f(x, Q^2) \right] A_f^{L,R}(Q^2) \tag{1.11}$$

$$xF_3^{L,R}(x, Q^2) = \sum_{\text{flavors}} \left[xq_f(x, Q^2) - x\bar{q}_f(x, Q^2) \right] B_f^{L,R}(Q^2) \tag{1.12}$$

The coupling coefficients A_f and B_f are, according to electro–weak theory, different for left– (L) and right–handed (R) electrons (positrons). With e_f being the electric charge of a parton of flavor f in units of the electron charge ($e_e = -1$), $\nu_f = [T_{3f} - 2e_f \sin^2 \theta_W]/\sin 2\theta_W$ and $a_f = T_{3f}/\sin 2\theta_W$ being the neutral current vector and axial–vector couplings, expressed in terms of the third component of the weak isospin ($T_3 = -\frac{1}{2}$ for e_L^- and d_L like flavors, $T_3 = \frac{1}{2}$ for u_L like flavors and $T_3 = 0$ for right–handed electrons and quarks) and with $P_Z = Q^2/(Q^2 + M_Z^2)$ being the ratio of the Z^0 and γ propagators, they can be written as follows:

$$A_f^{L,R}(Q^2) = e_f^2 - 2e_f(\nu_e \pm a_e)\nu_f P_Z + (\nu_e \pm a_e)^2(\nu_f^2 + a_f^2)P_Z^2 \tag{1.13}$$

$$B_f^{L,R}(Q^2) = \mp 2e_f(\nu_e \pm a_e)a_f P_Z \pm 2(\nu_e \pm a_e)^2 \nu_f a_f P_Z^2 \tag{1.14}$$

where $\pm$ corresponds to left (L) and right (R) handed electrons (right (R) and left (L) handed positrons). The cross section for arbitrarily polarized electron (positron) beam is obtained as the weighted average of these pure left– and right–handed cross sections.

At low Q^2 ($Q^2 \ll M_Z^2$), all terms proportional to P_Z can be safely neglected and only pure γ–exchange plays a rôle. The coefficients A_f and B_f become:

$$A_f = e_f^2, \qquad B_f = 0$$

and therefore:

$$F_2(x, Q^2) = \sum_{\text{flavors}} \left[xq_f(x, Q^2) + x\bar{q}_f(x, Q^2) \right] e_f^2 \tag{1.15}$$

$$F_3(x, Q^2) = 0 \tag{1.16}$$

The total differential cross section formula reduces to:

$$\frac{\mathrm{d}^2\sigma(e^\pm p)}{\mathrm{d}x\,\mathrm{d}Q^2} = \frac{2\pi\alpha^2}{xQ^4} \left[(1 + (1-y)^2)F_2(x, Q^2) - y^2 F_L(x, Q^2) \right] \tag{1.17}$$

This cross section is (as it ought to be, as long as the assumption of single photon exchange holds) symmetric under charge exchange (i.e. identical for e^+p and e^-p reactions) and independent of the helicity state of the incoming electron. Therefore, no further distinction will be made below.

1.4   Photon proton scattering

Formula (1.17) describes neutral current electron proton scattering over a large kinematical range in the (x, Q^2)–plane, where massive boson exchange can be neglected $(Q^2 \ll M_Z^2)$. In this region, only photon exchange has to be considered and the rôle of the incoming electron reduces to be a source of (virtual) photons, which are interacting with the proton. It is possible to rewrite ep–scattering in terms of a photon–proton reaction. The cross sections for photon–proton reactions for photons with energy ν and virtuality q^2 can be written as follows [18]:

$$\sigma_T(\nu, q^2) = \frac{4\pi^2 \alpha}{\nu} W_1(\nu, q^2) \tag{1.18}$$

$$\sigma_L(\nu, q^2) = \frac{4\pi^2 \alpha}{\nu} \left[\left(1 - \frac{\nu^2}{q^2} \right) W_2(\nu, q^2) - W_1(\nu, q^2) \right] \tag{1.19}$$

where σ_T and σ_L are the cross sections for transverse and longitudinal polarized photons and $W_1(\nu, q^2)$ and $W_2(\nu, q^2)$ are the only two independent terms of the most general form of the hadronic tensor $W^{\mu\nu}$, which is constructed out of the metric tensor $g^{\mu\nu}$ and the momenta p and q. It describes the hadronic current in the $ep \to eX$ reaction[†]. As the photon is not explicitly considered to be on its mass shell (q^2 not vanishing) , also longitudinal polarized photons have to be taken into account. In these formulas, only the mass of the electron has been neglected, the proton mass m_p is present. It is not possible to calculate the total differential cross section $\sigma_{tot}^{\gamma p}(\nu, q^2)$ by just taking the sum of the above two formulas, as the flux for the incoming photons is only defined for real photons. For the virtual photon flux, a conventional choice[††] has been used. Anyhow, in the limit of vanishing virtuality the correct total cross section is obtained, $\sigma_T \xrightarrow{q^2 \to 0} \sigma_{tot}^{\gamma p}$ and $\sigma_L \xrightarrow{q^2 \to 0} 0$.

For a comparison with DIS electron proton scattering (formula (1.17)), the $W_{1,2}$ have to

---

[†]The matrix element to construct the cross section is calculated out of the hadronic current $W^{\mu\nu}$ and the QED leptonic current $L_{\mu\nu}^e$: $d\sigma \sim |\mathfrak{M}^2| = L_{\mu\nu}^e W^{\mu\nu}$, or in the language of *real* photon–proton reaction, with the polarization vector ε^μ of the photon: $\sigma_{tot}^{\gamma p} = \frac{4\pi^2 \alpha}{\nu} \varepsilon^{\mu *} \varepsilon^\nu W_{\mu\nu}$.

[††]The flux for *real* photons is simply ν, as it has been used in above's definition for both, transversal and longitudinal photon cross section. An other convention is to use $\nu + \frac{q^2}{2m_p}$ instead of ν. This is the Hand–convention [19]. Both conventions are identical in the limit of negligible virtuality. Using this convention would cause a factor of $(1 - x)$ in the forthcoming formulae (equations (1.22)–(1.28)), which relate the structure functions F_i with the photon cross sections $\sigma_{T,L}$. Such differences in kinematical factors are of course entirely absorbed in the definition of σ_L and σ_T.

be translated:

$$m_p W_1(\nu, q^2) \to F_1(\nu, q^2) = \left| \frac{\partial \nu}{\partial x} \cdot \frac{\partial q^2}{\partial Q^2} - \frac{\partial \nu}{\partial Q^2} \cdot \frac{\partial q^2}{\partial x} \right| \cdot F_1(x, Q^2) \qquad (1.20)$$

$$\nu W_2(\nu, q^2) \to F_2(\nu, q^2) = \left| \frac{\partial \nu}{\partial x} \cdot \frac{\partial q^2}{\partial Q^2} - \frac{\partial \nu}{\partial Q^2} \cdot \frac{\partial q^2}{\partial x} \right| \cdot F_2(x, Q^2) \qquad (1.21)$$

with

$$x = \frac{Q^2}{2pq} = \frac{Q^2}{2m_p \nu} \qquad \text{and} \qquad Q^2 = -q^2$$

$F_{1,2}(x, Q^2)$ are independent of Q^2 at sufficiently large x where the photon just probes single spin–1/2 partons in the proton (Bjorken scaling). However, as soon as gluons are probed inside the proton, Bjorken scaling ends and again a Q^2–dependence of the structure functions $F_{1,2}$ is seen. A possible but so far purely hypothetical substructure of the quarks would also emerge as a scaling violation.

Rewriting of σ_T and σ_L yields:

$$\sigma_T(x, Q^2) = \frac{4\pi^2 \alpha}{Q^2} \cdot 2x F_1(x, Q^2) \qquad (1.22)$$

$$\sigma_L(x, Q^2) = \frac{4\pi^2 \alpha}{Q^2} \left[\left(1 + \frac{4m_p^2 x^2}{Q^2} \right) F_2(x, Q^2) - 2x F_1(x, Q^2) \right] \qquad (1.23)$$

Solving equations (1.22) and (1.23) for F_1 and F_2 yields:

$$F_1(x, Q^2) = \frac{Q^2}{4\pi^2 \alpha} \cdot \frac{1}{2x} \sigma_T(x, Q^2) \qquad (1.24)$$

$$F_2(x, Q^2) = \frac{Q^2}{4\pi^2 \alpha} \left(1 - \frac{4m_p^2 x}{ys} \right) (\sigma_T(x, Q^2) + \sigma_L(x, Q^2)) \qquad (1.25)$$

Above formula (1.23) contains the Callan–Gross relation without having neglected the proton mass m_p:

$$F_L(x, Q^2) \equiv \left(1 + \frac{4m_p^2 x^2}{Q^2} \right) F_2(x, Q^2) - 2x F_1(x, Q^2) \qquad (1.26)$$

$$= \frac{Q^2}{4\pi^2 \alpha} \sigma_L(x, Q^2) \qquad (1.27)$$

This definition of F_L is identical to the old definition (cf. equation (1.8)) as soon as the proton mass m_p is neglected. Additionally, F_L is proportional to the longitudinal part of the photon cross section and therefore vanishes if the proton is probed with real (purely transversly polarized) photons only. Therefore, F_L is called the *longitudinal structure function*.

After a variable transformation, neglecting the proton's rest mass m_p and making use of definition (1.26) for F_L, the total differential electron proton cross section (1.17) can now be written as a function of y and Q^2 for single photon exchange in terms of the transversal and longitudinal photon cross sections $\sigma_T(y, Q^2)$ and $\sigma_L(y, Q^2)$:

$$\frac{\mathrm{d}^2\sigma(e^\pm p)}{\mathrm{d}y\mathrm{d}Q^2} = \frac{\alpha}{2\pi} \cdot \frac{1}{yQ^2} \cdot \left[(1 - (1-y)^2)\sigma_T(y, Q^2) + 2(1-y)\sigma_L(y, Q^2)\right] \tag{1.28}$$

The first term in above formula (1.28), which is proportional to σ_T, yields directly the Weizsäcker–Williams approximation [20, 21] for the photon flux of quasi–real photons.

To circumvent the problems with the convention, which is used to define the flux for virtual photons, the ratio R of the longitudinal to the transversal cross section is introduced, which is independent of any normalization factors:

$$R(x, Q^2) \equiv \sigma_L/\sigma_T \tag{1.29}$$

$$= \left(1 + \frac{4m_p^2 x}{Q^2}\right) \frac{F_2(x, Q^2)}{2xF_1(x, Q^2)} - 1 \tag{1.30}$$

$$= \frac{F_L(x, Q^2)}{2xF_1(x, Q^2)} \tag{1.31}$$

The relation between the total photoproduction cross sections of transversely and longitudinal polarized virtual photons and the structure function F_2 is then the following:

$$\sigma_T(x, Q^2) = \frac{4\pi^2\alpha}{Q^2} \left(1 + \frac{4m_p^2 x^2}{Q^2}\right) \frac{1}{1 + R(x, Q^2)} \cdot F_2(x, Q^2) \tag{1.32}$$

This relation[†] can be used to parameterize the total photoproduction cross section [22, 23, 13].

1.5   Photoproduction

Photoproduction physics is defined in the limit of vanishing Q^2, where *quasi real* photons interact with the proton. In that limit the contribution from longitudinal polarized photons can be safely neglected:

$$Q^2 \approx 0 \quad \Rightarrow \quad \sigma_L = 0, \quad R = 0 \quad \text{and} \quad F_L = 0$$

[†]Care has to be taken according the convention used which defines the photon cross section; reference [22], for instance, reads with an additional factor $(1 - x)$ as follows:
$$\sigma_T(x, Q^2) = \frac{4\pi^2\alpha}{Q^2} \frac{1}{1-x} \left(1 + \frac{4m_p^2 x^2}{Q^2}\right) \frac{1}{1 + R(x, Q^2)} \cdot F_2(x, Q^2).$$

The Bjorken scaling variable x vanishes as well (from (1.6)):

$$x = \frac{Q^2}{Q^2 + W^2 - m_p^2} \approx \frac{Q^2}{W^2} \approx 0$$

Equation (1.2) implies, that the scattering angle ϑ is close to π (cf. p. 3). This leads the variable y to become simply:

$$y \stackrel{\text{lab}}{=} 1 - \frac{E_e'}{E_e}\sin^2\frac{\vartheta}{2} \;=\; 1 - \frac{E_e'}{E_e} + \frac{Q^2}{4E_e^2} \;\approx\; 1 - \frac{E_e'}{E_e} \tag{1.33}$$

y stays finite, as the energy of the scattered electron is smaller than the incoming electron energy. The invariant mass of the hadronic system W^2 is at the same time the invariant mass of the photon–proton system. Equation (1.6) together with (1.5) yields:

$$W_{\gamma p}^2 = W^2 = ys(1-x) + m_p^2 \approx ys \tag{1.34}$$

In this limit, the transverse photoproduction cross section $\sigma_T(x, Q^2)$ can be identified with the total photoproduction cross section $\sigma_{\text{tot}}^{\gamma p}$, which depends only on one kinematical variable (usually $W_{\gamma p}$, the invariant mass of the γp–system). Using equation (1.32), the total cross section for *real* photon-proton reaction can now be written as follows[†]:

$$\sigma_{tot}^{\gamma p}(W_{\gamma p}) \;=\; \left.\frac{4\pi^2\alpha}{Q^2}F_2(x, Q^2)\right|_{Q^2=0} \tag{1.35}$$

which implies that $F_2(x, Q^2) \sim Q^2$ in the limit of $Q^2 \to 0$, as the cross section is a finite quantity [23]. This restricts the choice of possible functions to parameterize F_2.

For a measurement of the total photoproduction cross section $\sigma_{\text{tot}}^{\gamma p}$ above formula is not very helpful, as one has to measure the proton structure function F_2 in the limit of $Q^2 = 0$. A better choice is to refer to the differential cross section as given in equation (1.28). Rewriting this formula in the limit of real photoproduction leads to the first dominating term (Weizsäcker–Williams approximation [20, 21]) in following equation:

$$\frac{\mathrm{d}^2\sigma(ep)}{\mathrm{d}y\mathrm{d}Q^2} \;=\; \frac{\alpha}{2\pi}\frac{1}{Q^2}\left(\frac{(1-(1-y)^2)}{y} - \frac{2(1-y)}{y}\frac{Q_{\text{min}}^2}{Q^2}\right)\cdot\sigma_{\text{tot}}^{\gamma p}(ys) \tag{1.36}$$

The second term, proportional to Q_{min}^2 has been neglected so far, as Q_{min}^2 is proportional to the electron mass squared. This term contributes $6-7\%$ to the total photoproduction cross section at HERA energies [24, 25, 26].

$Q_{\text{min}}^2 = m_e^2 y^2/(1-y)$ is the minimal photon virtuality at fixed y, which corresponds to an electron, which just deposits some energy in the proton, but without being deflected by the $ep \to eX$ reaction.

[†]Again, according the convention used for the (virtual) photon flux, care has to be taken on a possible factor $(1-x)$.

1.6   The physical photon

For a further understanding of photon–proton scattering, it is necessary to take other aspects into account, besides the study of proton structure functions. Photon–proton interactions can most effectively be understood in the frame work of hadron–hadron reactions. The most obvious similarity of photon and hadron interactions is the behavior of the total cross section versus impact energy, which is illustrated in fig 1.2.
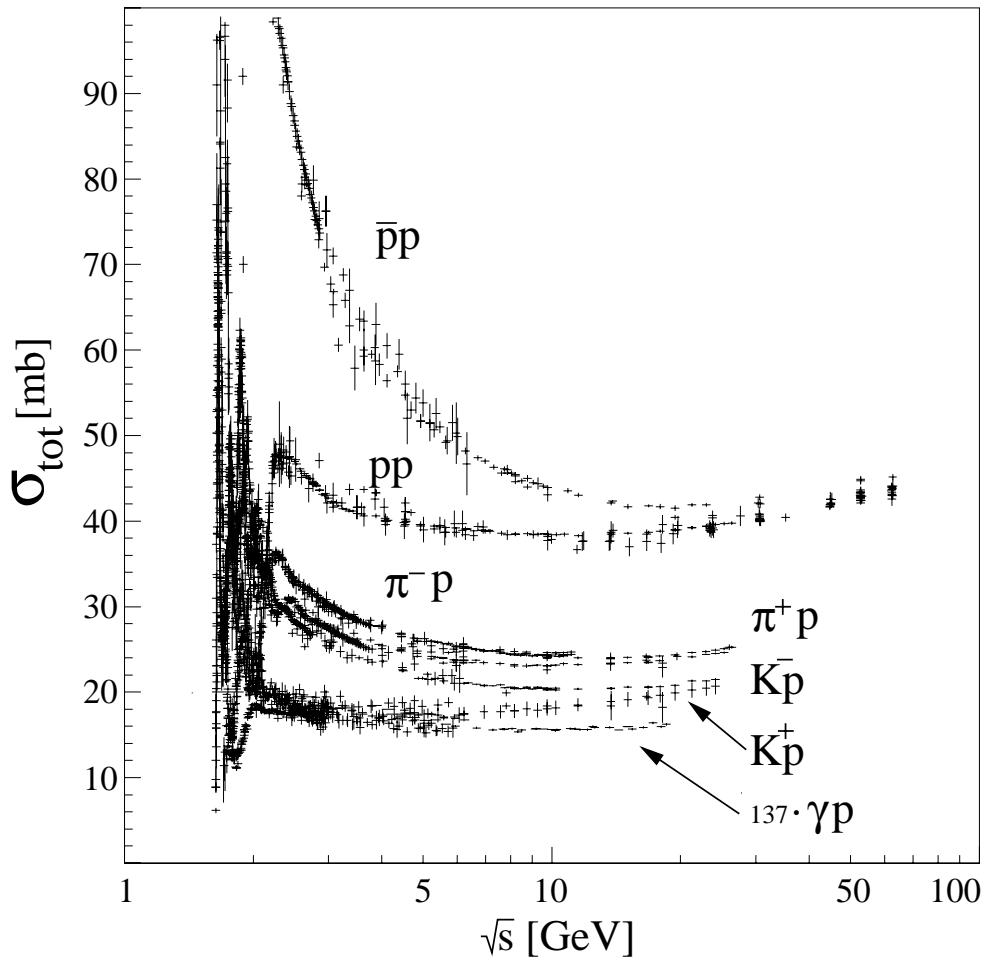
Figure 1.2: Total cross sections for various particles on proton targets versus center–of–mass energy. Beyond the resonance region at low energies a structure less universal rise of the cross section is seen. According to the Pomeranchuk theorem, the cross sections for hadron–proton interactions are, in the asymptotic limit of high energies, the same as for anti–hadron–proton interactions [27]. The photon–proton cross sections have been multiplied with a factor of $1/\alpha_{em}$. (Compilation of data points from the Particle–Data–Group [28].)

Both photon–proton and hadron–proton reactions show resonances at low energies, and level out and become structureless above a few GeV, apparently tending to a slow universal rise at high energies. The photon total cross section is smaller than the hadronic one by a factor approximately equal to the fine structure constant.

There is one important difference. Whereas the total elastic cross section ($hp \rightarrow h'p'$) in purely hadronic collisions is typically 15-20% of the total cross section ($hp \rightarrow X$), as illustrated in fig 1.3, this is not the case for the purely elastic electromagnetic process of proton–Compton scattering ($\gamma p \rightarrow \gamma'p'$), where this fraction is in the order of α_{em}. This difference is compensated by diffractive photoproduction of neutral vector mesons V ($\gamma p \rightarrow Vp$) , most prominently the ρ^0. The fraction of photoproduction events attributable to V production is in the order of σ_{el}/σ_{tot} for hadronic collisions.

The slope parameter b [†] for $hp \rightarrow h'p'$ scattering is within the measurement the same as for elastic V production in photoproduction events $\gamma p \rightarrow \rho^0 p'$ [29].
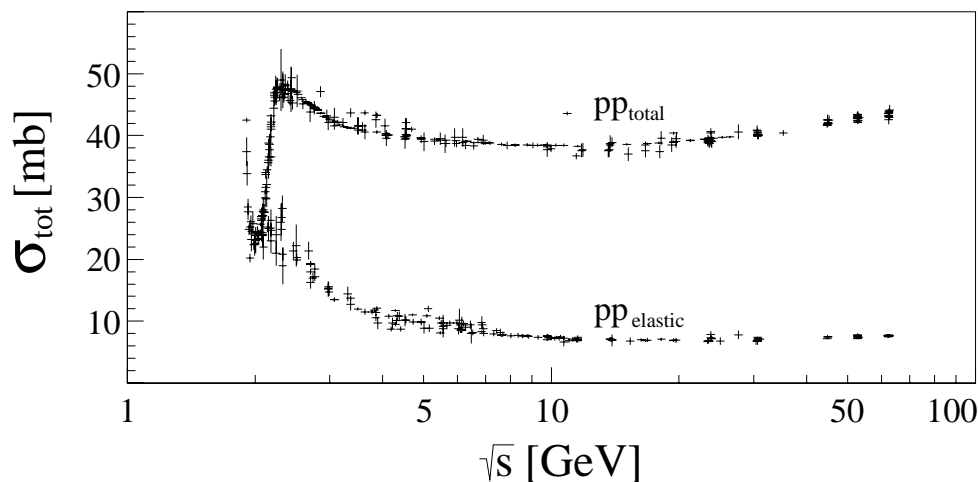
Figure 1.3: Total and elastic cross section for proton–proton interactions versus center–of–mass energy. Below the threshold for additional particle production both the total and the elastic cross section are the same. At higher energies, the elastic cross section contributes typically 15-20% to the total cross section. This is typical for all hadron–hadron collisions.(Compilation of data points from the Particle–Data–Group [28].)

These observations lead to the formulation of the *Vector Meson Dominance* model (VMD) [11], where the physical photon is understood as a superposition of a bare photon $|\gamma_b\rangle$ and a small (order of $\sqrt{\alpha}_{em}$) hadronic component $\sqrt{\alpha}_{em} |h\rangle$:

$$|\gamma\rangle = \sqrt{Z_3} |\gamma_b\rangle + c\sqrt{\alpha}_{em} |h\rangle \tag{1.37}$$

[†]See section 1.7 for a definition of the slope paramater b.

Where $Z_3 = 1 - c^2\alpha$ assures proper normalization of $|\gamma\rangle$ and c is of $\mathcal{O}(1)$. The photon is therefore allowed to fluctuate into a $q\bar{q}$–state forming a light meson, which then interacts with the proton. The state $|h\rangle$ must have the same quantum numbers as the photon, $J^{PC} = 1^{--}, Q = B = S = 0$, which is fulfilled for neutral vector mesons in their $q\bar{q}$ ground state. The restrictive assertion that the bare component $|\gamma_b\rangle$ does not interact at all with hadrons and that the three vector mesons ρ^0, ω and ϕ are the sole hadronic constituents of the photon, is the VMD hypothesis in its most naïve form. This gives:

$$c\sqrt{\alpha}_{em} |h\rangle = \sum_{V=\rho^0,\omega,\phi} \frac{e}{f_V} |V\rangle \tag{1.38}$$

The factor $(e/f_V)^2 = 4\pi\alpha_{em}/f_V^2$ gives the probability for the transition $\gamma \to V$. Fits to low energy data yields the coefficients $f_V^2/4\pi$ to be 2.20 for ρ^0, 23.6 for ω and 18.4 for ϕ [11]. These couplings imply that the photon can be found about 0.4% of the time in its VMD state. Most of the time, the photon is still a point like particle, $1 - Z_3 \ll 1$. It is only because the hadronic $\rho^0 p$ cross section is so much larger than the direct γp one, that the γp cross section is dominated by the VMD contributions.

This rigid assumption only holds for soft (low–$p_\perp$) physics. Fixed–target photoproduction is rather well described. Significant differences are expected at higher energies. To accommodate to HERA energies, extensions over the rigid VMD approach are necessary and lead to generalized VMD (gVMD) models.

In the first possible extension a non-vanishing bare photon–proton interaction is introduced, leading to so called *direct* events, wherein the photon interacts directly with a parton from the proton. This mechanism is illustrated in fig 1.4a.

A second extension introduces fluctuations of the photon into heavier $q\bar{q}$ states and by virtue of QCD corrections, states with additional gluon and $q\bar{q}$ pairs are included: $|q\bar{q}gg\rangle$, $|q\bar{q}q\bar{q}\rangle$ etc. These fluctuations no longer interact as a single particle, only the partonic content of the fluctuation interacts with the proton, which often leads to a high–$p_\perp$ topology in these events. Such a partonic content of the photon leads to a description of the photon with help of a structure function. The measurement of this structure function, which contains the gluon and quark densities within the photon is a further topic of HERA physics [30]. This mechanism leads to so called *anomalous* events, and is illustrated in fig 1.4c. Together with the standard VMD events, such events are referred to as *resolved* events, as the photon first fluctuates into an intermediate state, which then interacts. The remaining part of the photon fluctuation, not involved in the hard scattering, leads to a *photon remnant*, which is an important feature in the event–topology of resolved photoproduction events.

A third possible extension would be to introduce fluctuations into lepton–pairs: $|e^+e^-\rangle, |\mu^+\mu^-\rangle$ or $|\tau^+\tau^-\rangle$. Since these leptonic states would not undergo strong interactions their contributions can be safely neglected.
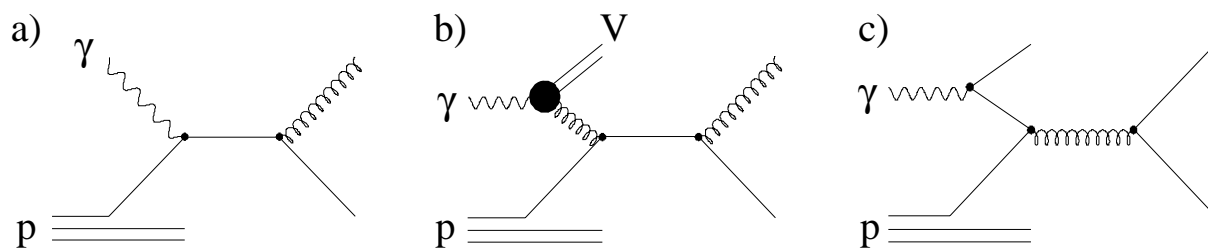
Figure 1.4: Examples for interactions of a quasi–real photon with a proton: a) direct γp–interaction, b) and c) resolved γp–interactions, with b) showing the genuine VMD case and c) the anomalous contribution. Whereas straight lines refer to quarks, wiggly lines to photons and curly lines to gluons.

The total photoproduction cross section therefore decomposes into a direct, a VMD and an anomalous part [12]:

$$\sigma_{\text{tot}}^{\gamma p}(s) = \sigma_{\text{direct}}^{\gamma p}(s) + \sigma_{\text{VMD}}^{\gamma p}(s) + \sigma_{\text{anomalous}}^{\gamma p}(s) \tag{1.39}$$

1.7 Hadronic physics

As the photon often interacts like a hadron in photon–proton scattering, some aspects of hadronic physics will be discussed now, before we return to photon–proton reactions.

In hadronic physics, which describes scattering phenomena between hadrons, usually several different event classes, such as elastic, diffractive and non–diffractive, are distinguished. Elastic processes are those processes, where the scattered particles stay intact, i.e. $a + b \rightarrow a + b$. Diffractive processes, allow one or both incoming hadrons to dissociate, which means that the hadron turns into an excited state of mass M_X, which then decays into its final state. No quantum–numbers[†] are exchanged between the reacting particles, i.e. $a + b \rightarrow X + b$ for single diffractive dissociation and $a + b \rightarrow X_1 + X_2$ for double diffractive dissociation. What remains is called non–diffractive processes, i.e. $a + b \rightarrow X$.

Elastic scattering, diffractive dissociation and the total cross section of hadron–hadron interactions show some universal features independent of the hadron type involved in the reactions. Examples are the shrinking of the forward elastic scattering peak with increasing energy (see fig 1.5), the $1/M_X^2$ behavior of diffractive dissociation (see fig 1.6) and the rising of the total cross section at high energies (see fig 1.2).

The most simple picture which is able to explain some of these aspects is the *black disk* model, in which diffraction of a (particle) wave on a small black disk of radius R is studied.

[†]Only *internal* quantum–numbers, such as charge, spin, isospin, strangeness, ... of the reacting hadrons are meant.
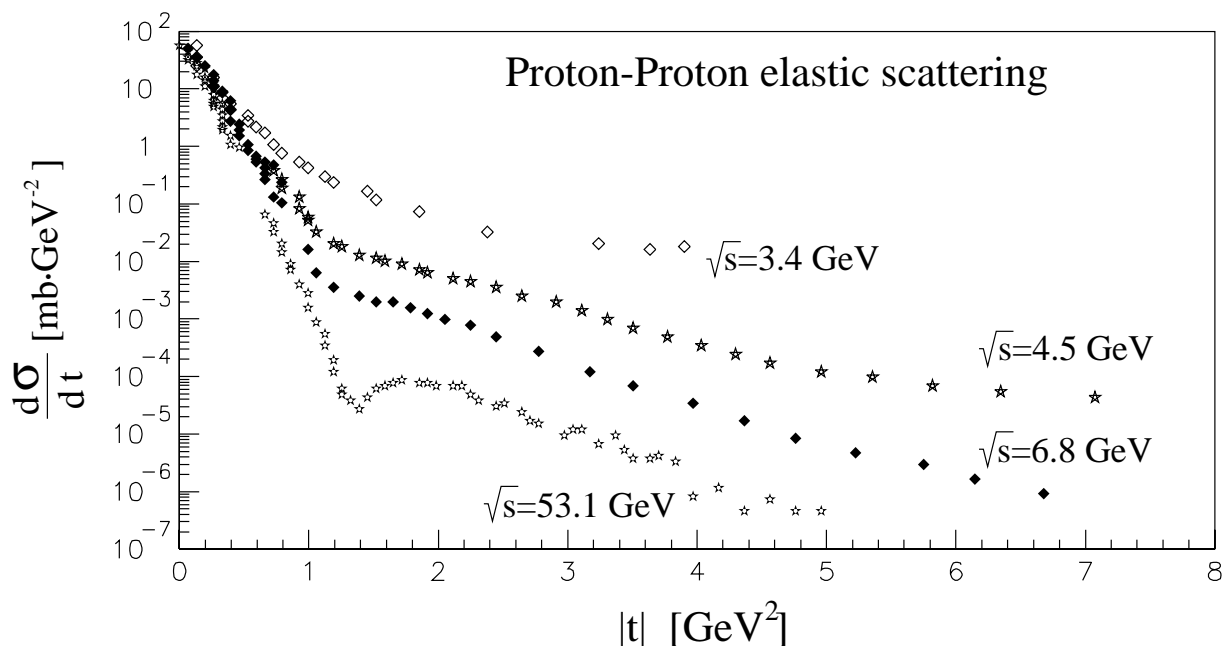
Figure 1.5: Proton–proton elastic differential cross section versus four–momentum transfer squared at various center–of–mass energies. With increasing energy, the peak at low values of t gets narrower (shrinkage) and a classical interference pattern (diffraction) shows up (from ref. [31]).

The intensity of light passing a black disk as a function of the scattering angle ϑ is given by:

$$\frac{I}{I_0} = \frac{[2J_1(x)]^2}{x} \approx 1 - \frac{R^2}{4}(k\vartheta)^2 \quad \text{for} \quad \vartheta \ll 1 \tag{1.40}$$

where k is the wave number of the photon, R is the radius of the black disk, $x = kR\sin\vartheta \approx kR\vartheta$ and $J_1(x)$ being the first order Bessel–function. For small values of x, the Bessel–function $J_1(x)$ may be approximated by an exponential, whereas for larger values of x, the Bessel–function undergoes the maxima and minima characteristical for diffractive phenomena.

The angular or t distribution ($t \approx -(p\vartheta)^2$; $\vartheta \ll 1$) as obtained from the collision of two hadrons with momentum p (p measured in their center–of–mass system), where t is the four–momentum transfer squared between the two hadrons and ϑ is the angle of the scattered hadron with respect to the incoming hadron, is strikingly similar to the diffraction pattern resulting from diffraction of light by a small black disk, as can be seen in fig 1.5 which shows the differential cross section $\mathrm{d}\sigma/\mathrm{d}t$ for elastic $pp \to pp$ scattering.

As the energy increases, the forward elastic peak becomes visibly exponential and a secondary diffraction maximum appears. For small values of $|t|$, the differential cross section
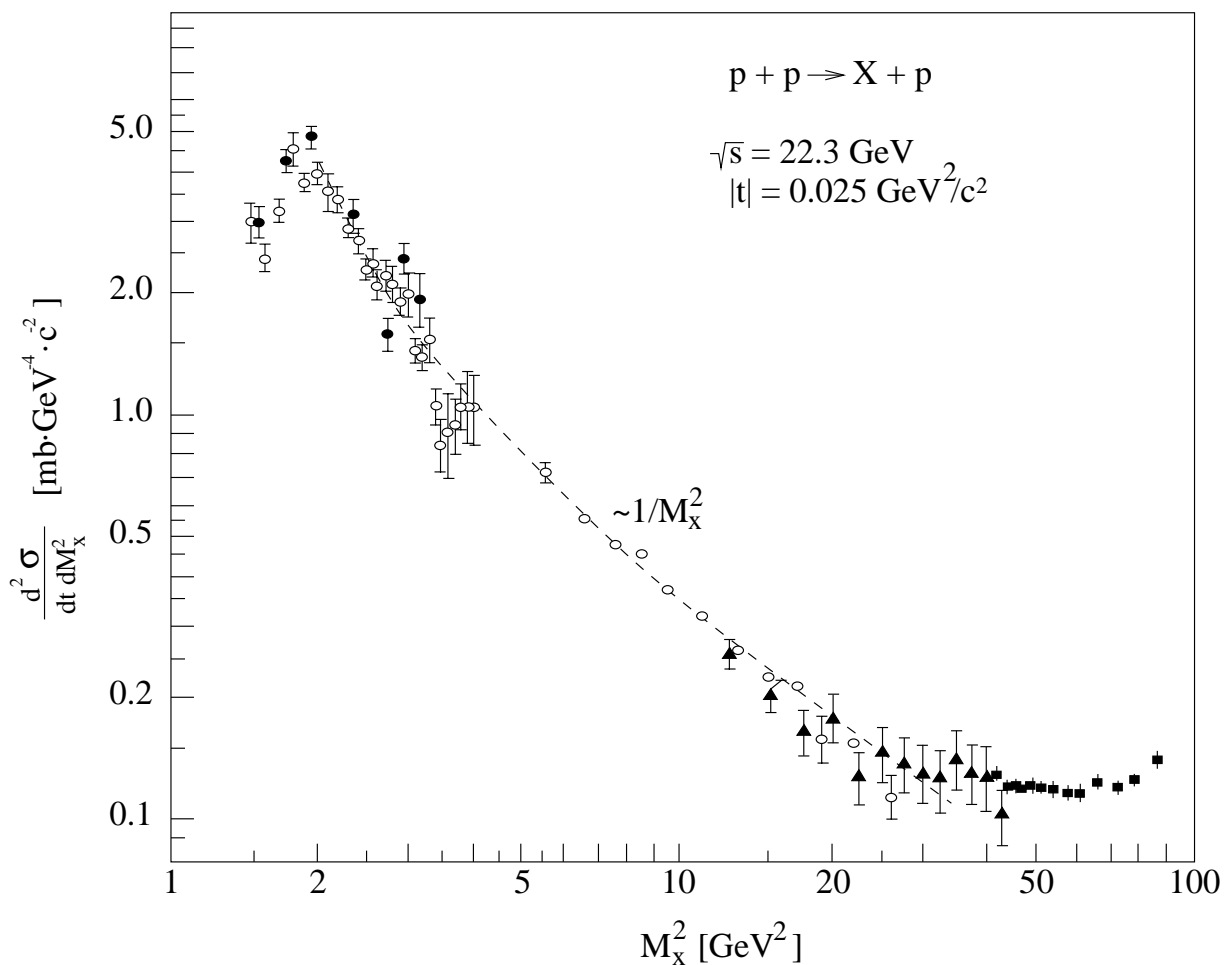
Figure 1.6: Proton–proton single diffractive dissociation differential cross section versus excitation mass M_X at fixed center of mass energy of $\sqrt{s} = 22.3$ GeV and fixed four–momentum transfer $|t| = 0.025$ GeV^2/c^2. The differential cross section first undergoes a resonant region with $M_X \gtrsim m_p$, at $M_X \approx 5$ GeV^2 a diffractive continuum region with the typical $1/M_X^2$ dependence is seen. Very large values of M_X^2 are no longer attributable to diffractive dissociation and a violation of the $1/M_X^2$ dependence is seen. (from ref. [32]).

can therefore be written as follows:

$$\frac{\frac{\mathrm{d}\sigma}{\mathrm{d}t}}{\left(\frac{\mathrm{d}\sigma}{\mathrm{d}t}\right)_{t=0}} = e^{bt} \approx 1 - b(k\vartheta)^2 \quad \text{for} \quad \vartheta \ll 1 \tag{1.41}$$

where k is the wave number of the incident particle and b, the slope parameter, is a so far not further specified variable, chosen such to describe the data at best. A comparison of equations (1.40) and (1.41) leads to a relationship between the interaction radius (the

radius of the black disk) and the slope parameter b.

$$b = \frac{1}{4}R^2 \qquad (1.42)$$

For $R = 1/m_\pi$, which is a typical radius of strong interactions, equation (1.42) yields $b = 12.5\ \mathrm{GeV}^{-2}$ which fits well with the measurements [29]. The slope parameter b itself is a function of center–of–mass energy squared s and for larger values of t also a function of t, as can be seen in fig 1.5, therefore $b = b(s, t)$.

Additionally, the black–disk model gives an easy interpretation for the total cross section, which is simply the area of the disk for elastic scattering and the same amount for inelastic scattering:

$$\sigma_{\mathrm{tot}} = \sigma_{\mathrm{el.}} + \sigma_{\mathrm{inel.}} = \pi R^2 + \pi R^2 = 2\pi R^2 \qquad (1.43)$$

For the total cross section, equation (1.43) yields: $\sigma_{\mathrm{tot}} = 126$ mb.

Both results, the ratio between elastic and total cross section as well as the absolute value of the total cross section itself are qualitatively described by the black disk model, the missing factor 2-3 to describe also quantitatively the data is hidden in the underlying structure of the target hadron which is not treated at all within the black disk model.

1.8   Regge theory

For a further understanding of hadron–hadron interactions, some aspects of Regge theory [14, 15, 16] are pointed out.

The Regge model was constructed in the late 1950's, before the arrival of QCD. Hadron–hadron scattering $(a + b \rightarrow c + d)$ was then often described by a single virtual particle exchange with appropriate quantum numbers (for example a pion or a rho) in analogy to QED with single photon exchange. Associated with the virtual exchange particle of free mass m is a propagator term in the scattering amplitude of the form $f(q^2) \sim g^2/(q^2 - m^2)$, with g being some coupling constant, or in the Mandelstam representation $f(t) \sim g^2/(t - m^2)$. As the exchange particle is virtual (space–like) the four-momentum transfer squared is negative, $t < 0$ and the propagator stays finite. The propagator $f(t)$ is therefore relevant at small momentum transfer $|t|$ only and does not contribute at large values of $|t|$.

In Regge theory, this particle exchange is generalized to so called *Regge–pole* exchange. Regge pole exchange describes the exchange of states with appropriate quantum–numbers and different virtuality t and spin α. The relation between t and α is called the *Regge trajectory*, $\alpha(t)$ (see fig 1.7). The value of the trajectory function for $t = 0$ is called the

intercept. The trajectory $\alpha(t)$ is an analytic interpolation between particles of different spins and all other internal quantum numbers being identical. Figure 1.7, therefore shows four different trajectories, ρ–ρ_3–ρ_5, ω–ω_3, f_2–f_4–f_6 and a_2–a_4–a_6. It is remarkable, that all four trajectories follow one single fit, the reggeon–trajectory. Whenever a trajectory passes through an integer for bosonic Regge–poles or half–integer for fermionic Regge–poles, ($\alpha(t) = n$ or $\frac{n+1}{2}$) there should exist a particle of spin n (or $\frac{n+1}{2}$) and mass $m = \sqrt{t}$.
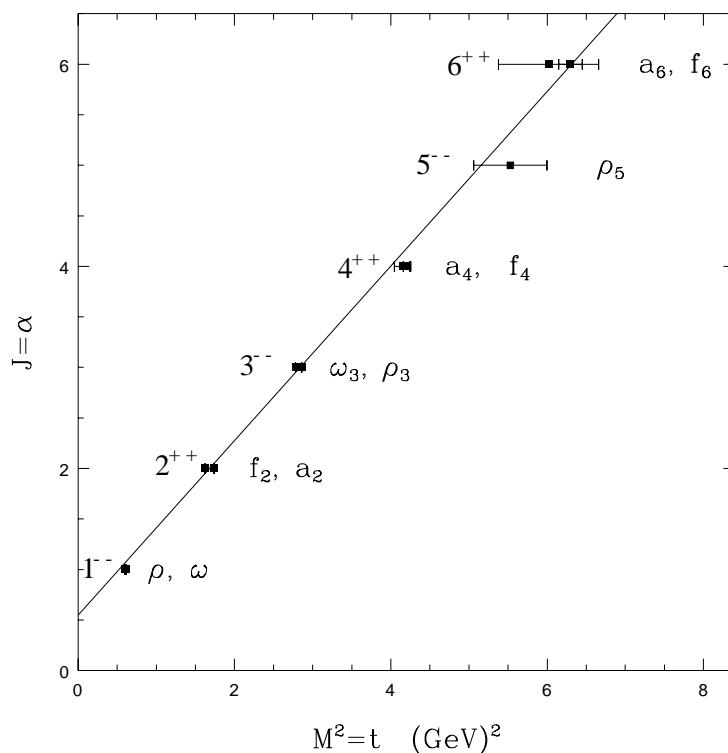
Figure 1.7: Regge trajectory - spins α of the particles ρ, ω, f_2, a_2 and their excitations are plotted against their squared masses t.

The Regge–pole carrying the quantum–numbers of the vacuum and describing diffractive scattering is called the *pomeron*. It is related to the Pomeranchuk theorem for asymptotic behavior of total cross sections [27] (see fig 1.2), which is why it was given the name pomeron. Other Regge–poles are called *reggeons*.

The name Regge–*pole* arises from the analysis of the analytic structure of the scattering amplitude. The exchange of states as described above leads to a pole in the scattering amplitude, more precisely in its partial wave amplitude. From the scattering amplitude, expressed in terms of Regge-trajectories, diffractive cross sections can be calculated with help of the the optical theorem, which relates the total cross section to the imaginary part

of the scattering amplitude at $t = 0$:

$$\sigma_{\text{tot}}^{ab \to X} = \sum_{\substack{k \\ \text{Regge-Poles}}} \beta_{ak}(0)\beta_{ab}(0)s^{[\alpha_k(0)-1]} \tag{1.44}$$

$$\frac{\mathrm{d}\sigma_{\text{elastic}}^{ab \to ab}}{\mathrm{d}t} = \sum_{\substack{k \\ \text{Regge-Poles}}} \frac{\beta_{ak}^2(t)\beta_{bk}^2(t)}{16\pi} s^{2[\alpha_k(t)-1]} \tag{1.45}$$

$$s\frac{\mathrm{d}^2\sigma^{ab \to Xb}}{\mathrm{d}t\,\mathrm{d}M_X^2} = \sum_{\substack{k,l \\ \text{Regge-Poles}}} \frac{\beta_{ak}(0)\beta_{bl}^2(t)g_{kll}(t)}{16\pi s} \left(\frac{s}{M_X^2}\right)^{2\alpha_l(t)} \left(M_X^2\right)^{\alpha_k(0)} \tag{1.46}$$

where $\beta(t)$ and $g(t)$ are functions of t and the hadrons and Regge-poles involved. The center–of–mass energy s has to be thought of as a normalized quantity, such as s/s_0 with s_0 being 1 GeV^2. The most prominent Regge trajectories are:

Pomeron $\qquad\qquad \alpha_{\mathbb{P}}(t) = \alpha_{\mathbb{P}}(0) + \alpha'_{\mathbb{P}}(t)\,t \;\equiv\; 1 + \Delta + \alpha'_{\mathbb{P}}(t)\,t \qquad$ (1.47)

Reggeon $\qquad\qquad \alpha_{\mathbb{R}}(t) \approx 0.55 + 0.86\,t \qquad\qquad\qquad\qquad\qquad\qquad$ (1.48)

Pion $\qquad\qquad\quad\; \alpha_{\pi}(t) \approx 0 + 0.9\,t \qquad\qquad\qquad\qquad\qquad\qquad\qquad$ (1.49)

All trajectories have intercepts less than unity except the Pomeron, which has an intercept slightly above one, $\alpha_{\mathbb{P}}(0) = 1.0808$, thus $\Delta = 0.0808$ [13], for $\alpha'(t)$ a value of 0.25 GeV^{-2} has been fitted [13]. This implies from equations (1.44)–(1.46), that all cross sections are dominated by the Pomeron–trajectory at high center–of–mass energies, as all other contributions die out with increasing energy $\sim s^{-0.4525}$ [13]. The cross sections listed above are then in the limit of large s:

$$\sigma_{\text{tot}}^{ab \to X}(s) \quad = \quad \beta_{a\mathbb{P}}(0)\beta_{b\mathbb{P}}(0)s^{\Delta} \;=\; \text{const} \cdot s^{\Delta} \tag{1.50}$$

$$\frac{\mathrm{d}\sigma_{\text{elastic}}^{ab \to ab}(s,t)}{\mathrm{d}t} \quad = \quad \frac{\beta_{a\mathbb{P}}^2(t)\beta_{b\mathbb{P}}^2(t)}{16\pi} s^{2\alpha'(t)\,t}\,s^{2\Delta} \tag{1.51}$$

$$\overset{\text{small } t}{=} \frac{\sigma_{\text{tot}}^2}{16\pi}e^{bt} \quad \text{with} \quad b(s,t) = b_0(t) + 2\alpha'(t)\ln s$$

$$\frac{\mathrm{d}^2\sigma^{ab \to Xb}(s,M_X^2,t)}{\mathrm{d}t\,\mathrm{d}M_X^2} \quad = \quad \frac{\beta_{a\mathbb{P}}(0)\beta_{b\mathbb{P}}^2(t)g_{\mathbb{P}\mathbb{P}\mathbb{P}}(t)}{16\pi M_X^2} \left(\frac{s}{M_X^2}\right)^{\Delta + 2\alpha'(t)\,t} s^{\Delta} \tag{1.52}$$

$$\overset{\text{small } t}{=} \frac{\text{const}}{M_X^2}e^{b_D t} \quad \text{with} \quad b_D(s,t) = b_{D,0}(t)$$
$$+ (\Delta + 2\alpha'(t))\ln\frac{s}{M_X^2} + \Delta\ln s$$

Thus, under Pomeron dominance, the total cross section rises slightly with energy. The rise is universal, which means it does not depend on the hadrons involved in the process. The forward (small t) elastic and diffractive dissociation peaks show the typical t–dependence of e^{bt} and shrink logarithmically with s. The diffractive dissociation cross section is independent of s and varies as $\sim 1/M_X^2$ [†].Not only the rise of the cross section is universal, but also the shrinkage is a property of the Pomeron–trajectory only. The b–slope parameters $b_0(t)$ and $b_{D,0}(t)$ are functions of $\beta_{a\mathbb{P}}, \beta_{b\mathbb{P}}$ and $g_{\mathbb{PPP}}$ and are therefore different for elastic and diffractive dissociation and depend also on the hadrons involved into the process.

The double diffractive dissociation process $a + b \rightarrow X_1 + X_2$ (DD) can be understood in terms of single diffractive dissociation (SD) and elastic scattering (EL) using a factorization ansatz [33]:

$$\frac{\mathrm{d}^3\sigma_{\mathrm{DD}}^{ab\rightarrow X_1 X_2}}{\mathrm{d}t\,\mathrm{d}M_{X_1}^2\,\mathrm{d}M_{X_2}^2} = \frac{\frac{\mathrm{d}^2\sigma_{\mathrm{SD}}^{ab\rightarrow X_1 b}}{\mathrm{d}t\,\mathrm{d}M_{X_1}^2} \cdot \frac{\mathrm{d}^2\sigma_{\mathrm{SD}}^{ab\rightarrow a X_2}}{\mathrm{d}t\,\mathrm{d}M_{X_2}^2}}{\frac{\mathrm{d}\sigma_{\mathrm{EL}}^{ab\rightarrow ab}}{\mathrm{d}t}} \tag{1.53}$$

Using the e^{bt} dependence derived above for both single diffractive dissociation and for elastic scattering yields after integration over t:

$$\frac{\mathrm{d}^2\sigma_{\mathrm{DD}}^{ab\rightarrow X_1 X_2}}{\mathrm{d}M_{X_1}^2\,\mathrm{d}M_{X_2}^2} = k\,\frac{1}{\sigma_{\mathrm{EL}}^{ab\rightarrow ab}}\,\frac{\mathrm{d}\sigma_{\mathrm{SD}}^{ab\rightarrow X_1 b}}{\mathrm{d}M_{X_1}^2}\,\frac{\mathrm{d}\sigma_{\mathrm{SD}}^{ab\rightarrow a X_2}}{\mathrm{d}M_{X_2}^2} \tag{1.54}$$

with $k = \dfrac{r^2}{2r - 1}$; $r = \dfrac{b_{\mathrm{SD}}}{b_{\mathrm{EL}}}$.

Further integration over M^2 gives the double diffraction dissociation cross section:

$$\sigma_{\mathrm{DD}} = k\frac{\sigma_{\mathrm{SD}}^2}{\sigma_{\mathrm{EL}}} \tag{1.55}$$

where σ_{SD} and σ_{EL} are the cross sections for single diffractive dissociation and for elastic scattering. As the factor k is independent of s and t, this relation is universal and the contribution of double diffractive dissociation is calculable once the factor k is determined.

For proton–proton interactions, r has been measured to be $r \approx 2/3$ and hence $k \approx 4/3$ [34].

1.9   How far can cross sections rise?

From equation (1.50) one learns that the total cross section in principle rises up to infinity, if only the collision energy becomes high enough.

[†]Taking the $\ln M_X$ dependence out of b_D, for single diffractive dissociation, yields to a $1/M_X^{2+2\Delta}$ dependence of the differential cross section.

The unitarity condition, which follows from probability conservation, demands that for each partial–wave belonging to a fixed angular momentum l in the scattering amplitude, the outgoing intensity can not be greater than the intensity of the corresponding incoming wave. This restricts the total cross section, which can be depictured again using the black–disk model: $\sigma_{\mathrm{tot}} \leq 4\pi R^2$. A rising cross section is therefore equivalent to a growing disk. A more specific bound has been found by Froissart and Martin [35, 36]. From unitarity and analyticity of partial–waves they derive an asymptotic limit for the total cross section:

$$\sigma_{\mathrm{tot}} \leq C \ln^2 s \tag{1.56}$$

where $C = 60$ mb. Or equivalently, in the asymptotic limit of high energies, the black disk can expand at most with the radius not growing faster than $\ln s$.

The Regge result, equation (1.50), violates the Froissart bound only at ultra–high energies. With $\sigma_{\mathrm{tot}} = 21.70\, s^\Delta$ mb for pp–reactions and $\sigma_{\mathrm{tot}} = 0.0677\, s^\Delta$ mb for γp–reactions [13], the Froissart bound is violated at $\sqrt{s} = 10^{29}$ GeV and $\sqrt{s} = 10^{47}$ GeV for pp and γp respectively. A tighter restriction can be found using the Pumplin bound [37], which is derived from the eikonal approximation of the scattering amplitude and the optical theorem. It limits the diffractive contribution to the total cross section:

$$\sigma_{\mathrm{elastic}} + \sigma_{\mathrm{diffractive}} \leq \frac{1}{2}\sigma_{\mathrm{tot}} \tag{1.57}$$

from which follows:

$$\frac{\sigma_{\mathrm{elastic}}}{\sigma_{\mathrm{tot}}} \leq \frac{1}{2} \tag{1.58}$$

Using equations (1.50) and (1.51) integrated over t, limits the total cross section:

$$\sigma_{\mathrm{tot}} = \mathrm{const}\, s^\Delta \leq \frac{1}{2} 16\pi b \tag{1.59}$$

This inequality is violated already at about $\sqrt{s} = 6 \cdot 10^6$ GeV and $\sqrt{s} = 10^{24}$ GeV for pp– and γp–reactions respectively. For the slope parameter b the result from equation (1.51) has been used including shrinkage and a fixed value b_0 of 12.5 GeV^{-2}.

The value Δ, therefore, has not to be seen as a fixed value, but a slight decrease with energy has to be considered in order not to violate above's bounds for the total cross section.

Within that picture, Regge–theory is able to describe cross sections up to any achievable energy and so far, neither from theory nor from experiments, a breakdown of the s^Δ–law is in sight.

It is up to now not clear, why total cross sections rise. Regge–theory does not necessarily explain this fact, as the value Δ, the intercept above unity of the pomeron trajectory, has been derived from data only and is not restricted by Regge–theory at all. A more crucial explanation is expected from QCD.

1.10   What is the Pomeron?

Quantum chromodynamics (QCD) is very successful in its perturbative approach, where, at large momentum transfer, the strong coupling constant α_s is small and therefore can be used as an expansion parameter. Regge–theory, on the other hand describes particle reactions at small values of t, here a perturbative approach naturally fails. The theorists debate on nature and properties of the pomeron is still going on.

Regge theory does not say what the pomeron is, however, some of its characteristics can be stated. In elastic and diffractive pp–scattering, the protons retain their identity, which means that no quantum numbers are exchanged. The pomeron is therefore a neutral, color–singlet state with C–parity $+1$. The easiest approach to describe these features is a 2–gluon exchange as depictured in fig 1.8a. This picture, which is not able to describe the rise of the cross sections, has first been introduced by Low and Nussinov [38, 39] in the mid 1970's.
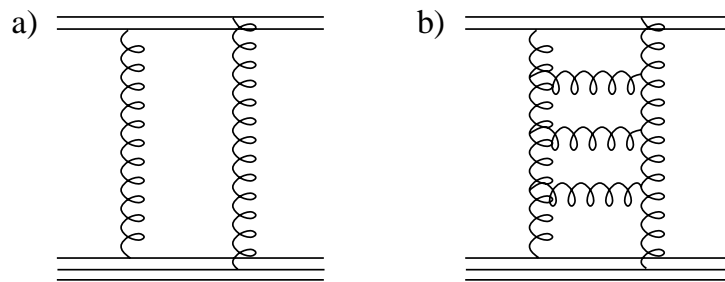
Figure 1.8:   The pomeron in QCD is thought as a gluon exchange process. All permutations of the quark–gluon vertices have to be summed up.
a) The Low–Nussinov picture of the pomeron as a simple, simultaneous two–gluon exchange process.
b) The Lipatov picture introduces gluon–gluon interactions in form of a ladder of gluon insertions, which defines the reggeized gluon. An infinite number of gluon insertions have to be summed up.

In the leading $\log(\frac{1}{x})$ approximation at high energy, without running coupling–constant (the Balitsky–Fadin–Kuraev–Lipatov (BFKL) equation [40, 41], 1978), a rising cross section with energy is obtained, $\sigma \sim s^\Delta$.

Lipatov introduced in 1986 the so called *reggeized gluon*, which, starting from the 2–gluon exchange, introduces gluon–gluon interactions between the 2 gluons (see fig 1.8b) and takes the running of the coupling constant α_s into account. A sum over an infinite number of such gluon insertions, containing each a convolution integrate of x and transverse momentum $k_\perp$ of the gluon lines, the Lipatov kernel, yields a rising cross section. This

defines the BFKL–pomeron:

$$\alpha_{\mathbb{P}}^{\text{BFKL}}(0) = 1 + \frac{12\alpha_s}{\pi}\ln 2 \qquad (1.60)$$

thus, a value for Δ of $\frac{12\alpha_s}{\pi}\ln 2$ is obtained. For typical values for α_s of ~ 0.2, a value for Δ of ~ 0.5 is obtained. This value is far above 0.0808 the value used to describe the data. Therefore, the pQCD descriptions of the pomeron are called *hard pomeron*, whereas the non–perturbative description within the Regge–theory defines the *soft pomeron*. It is not yet clear, whether this distinction is only academical, or if there really exist two different pomerons in nature.

The *critical pomeron* is the one with an intercept $\alpha_{\mathbb{P}}(0)$ equal to one, thus leading to a constant cross section at large energies, whereas the *supercritical pomeron* has an intercept $\alpha_{\mathbb{P}}(0)$ greater than one, thus yielding to a rising cross section, which eventually breaks the Pumplin and Froissart bounds.

Gluon–ladders, as introduced to build the reggeized gluon, constructed out of three gluons instead of two, have a C–parity of -1. Such constructs build the *odderon*. Or more generally, an even number of gluons defines the (hard) pomeron, an odd number of gluons defines the odderon. (Different models describe the pomeron as an infinite sum over more and more complex gluon–ladders.)

Different constructs and models exist, which try to explain the nature of the (soft/hard) pomeron. So a non–gluonic content is introduced, by $q\bar{q}$–loops and pomeron structure functions are defined.

Donnachie and Landshoff argue that the pomeron might be a glueball. The pomeron trajectory, equation (1.47), using the fitted intercept and slope [13], can be extrapolated assuming a straight line for the trajectory to positive $m^2 = t$, then $\alpha(t)$ is equal to 2 at $m \approx 1900$ MeV, this is the region where glueballs are postulated from lattice calculations. A possible candidate might be an exotic 2^{++}–state at the expected mass–scale of 1926 ± 12 MeV found by the WA91 collaboration [42].

Chapter 2

HERA

HERA is the first ever constructed electron-proton storage ring, located at the DESY laboratory in Hamburg, Germany [43]. Two independent accelerators store 820 GeV protons and 30 GeV electrons respectively to collide the two counterrotating beams head on in four interaction points spaced uniformly around its 6.3 km circumference. Four different experiments (H1, ZEUS, HERMES and HERA–B) make use of this facility. Whereas ZEUS [44] and H1 [45] measure genuine *ep*-collisions since spring 1992, HERMES [46] and HERA–B [47] are being built to record data using one beam only.
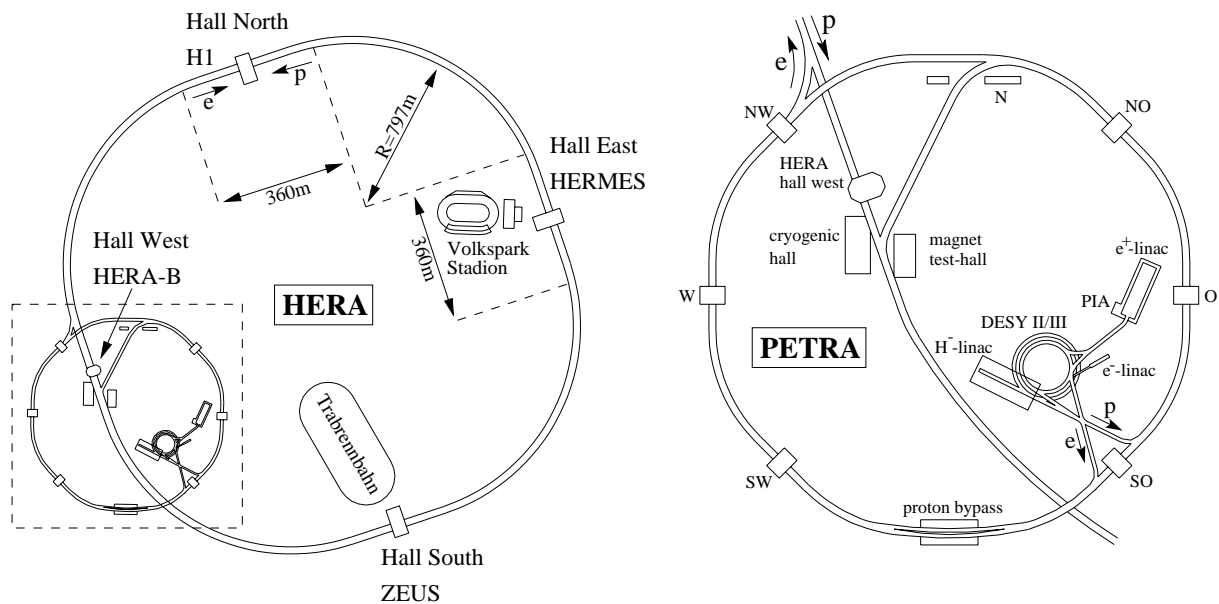
Figure 2.1: Layout of HERA with PETRA and pre–accelerators.

The layout of the HERA accelerator complex is depicted in fig 2.1 and its main parameters are given in Table 2.1.

	Design parameter		Autumn 1993		Autumn 1994	
	p ring	e ring	p ring	e ring	p ring	e ring
energy [GeV]	820	30	820	26.7	820	27.55
cm energy [GeV]	314		296		300	
peak luminosity [cm^{-2}s^{-1}]	1.5×10^{31}		1.8×10^{30}		3.7×10^{30}	
integrated luminosity [nb^{-1}y^{-1}]	10^5		10^3		6×10^3	
specific luminosity [cm^{-2}s^{-1}mA^{-2}]	3.3×10^{29}		4.5×10^{29}		5.2×10^{29}	
current per bunch [μA]	770	280	190	260	320	190
number of bunches	210	210	90	94	170	168
bunch separation [ns]	96	96	96	96	96	96
bunch–crossing rate [MHz]	10.41		10.41		10.41	
injection energy [GeV]	40	14	40	12	40	12
σ_x/σ_y at interaction point [mm]	0.28/0.09	0.30/0.06	0.36/0.10	0.30/0.07	0.18/0.06	0.28/0.06
σ_z at interaction point [mm]	110	8	180	8	110	8

Table 2.1: Summary of HERA parameters.

The electron machine uses conventional technology, accelerating the electrons to 27.5 GeV, whereas the proton ring makes use of superconducting magnets to produce the high magnetic field needed to keep the 820 GeV protons in their orbit.

Electrons (positrons) from a 500 MeV linear accelerator are injected into a small storage ring, accumulated into a 60 mA single bunch, injected on axis into DESY II, accelerated to 7 GeV and transferred to the PETRA II ring. This is repeated at a rate of 12.5 Hz until PETRA II has been filled up with maximum 70 bunches each with 0.4×10^{11} electrons (positrons), which are spaced at 28.8 m apart as in HERA, which are then injected into the HERA main ring. This is repeated 3 times until HERA has been filled up with maximum 210 bunches.

Negatively charged hydrogen ions from a 50 MeV linear accelerator are sent through a stripper foil, such that they loose their electrons and the bare proton remains. These protons are injected into DESY III and captured into 11 buckets each with 0.7×10^{12} protons,

spaced 28.8 m apart as in HERA, accelerated to 7.5 GeV and transferred to PETRA II. After PETRA II has been filled up with maximum 70 bunches, the protons are accelerated to a energy of 40 GeV before injected into HERA. Again, this has to be repeated 3 times until HERA has been filled up with maximum 210 bunches.

Normally protons are filled into the ring first and then ramped to the final energy of 820 GeV. The lifetime of the proton beam exceeds 100 h. During ramping of protons, PETRA II is switched to electrons (positrons) and two to three hours after a proton fill an electron (positron) fill can be obtained. Electrons (positrons) are then ramped too and finally the two beams are finetuned for collisions. The lifetime of the electron beam is typically 10 h, for positrons it can be up to 20 h, which is why since 1994 mainly e^+p–collisions have been recorded. Depending on the beam quality more than one positron fill can be made with the same proton fill.

Chapter 3

H1

The H1 detector, located at the north interaction point of HERA, is shown in fig 3.1 (cut along beam axis) and fig 3.2 (cut perpendicular to the beam axis). A detailed description of the H1 detector can be found in [45].

Since the center of mass for HERA collisions is boosted along the proton direction (which defines the z–axis of the H1 frame) with $\gamma_{cm} = 2.86$ the H1 detector is considerably more massive and higher instrumented in $+z$ (forward) direction. This is apparent from fig 3.1.

Starting the brief description from the center of the interaction region, the detector consists of a central and a forward tracking system, each containing different layers of drift and trigger proportional chambers. A liquid argon cryostat surrounds the tracker. It houses lead absorber plates and readout gaps for the electromagnetic section, which are followed by steel plates for the hadronic section with their readout gaps. A cylindrical, superconducting coil with a diameter of 6 m and a length of 5.75 m provides an analyzing field of 1.15 T. The iron return yoke of the magnet is laminated and filled with streamer tubes. The small fraction of hadronic energy leaking out of the back of the calorimeter is registered here and muon tracks are found. Muon identification further benefits from additional chambers inside and outside the iron. Very stiff muon tracks in forward direction are analyzed in a supplementary toroidal magnet sandwiched between drift chambers. The remaining holes in the liquid argon calorimeter are closed with warm calorimeters, a Si–Cu plug at very forward angles, a Pb–scintillator calorimeter backed by a tail catcher (part of the muon system) in backward direction and lastly an electron tagger at $z = -33$ m upstream from the interaction point (not shown in fig 3.1). The tagger marks the energy of an electron with very small scattering angle inducing a photoproduction event and, taken in coincidence with a corresponding photondetector at $z = -103$ m from the interaction point, monitors the luminosity by the bremsstrahlung process. Two scintillator walls in backward direction are installed to recognize background produced by the proton beam upstream of the H1–detector. A survey of detector parameters is given in table 3.1.

1	Central tracking chambers
2	Forward tracking + TRD
3	Elektromagnetic calorimeter (lead)
4	Hadronic calorimeter (stainless steel)
5	Liquid argon cryostat
6	Superconducting coil (1.2 T)
7	Instrumented iron (iron stabs + streamer tube detectors)
8	Muon chambers
9	Concrete shielding
10	Warm electromagnetic calorimeter
11	Beam pipe and beam magnets
12	Compensation coil
13	Liquid argon expansion vessel
14	Muon toroid magnet
15	Plug calorimeter
16	Time of flight system

Vertical cut along the beam

0   1   2   3   4m

Figure 3.1: Longitudinal cut through the H1–detector along the beam line.
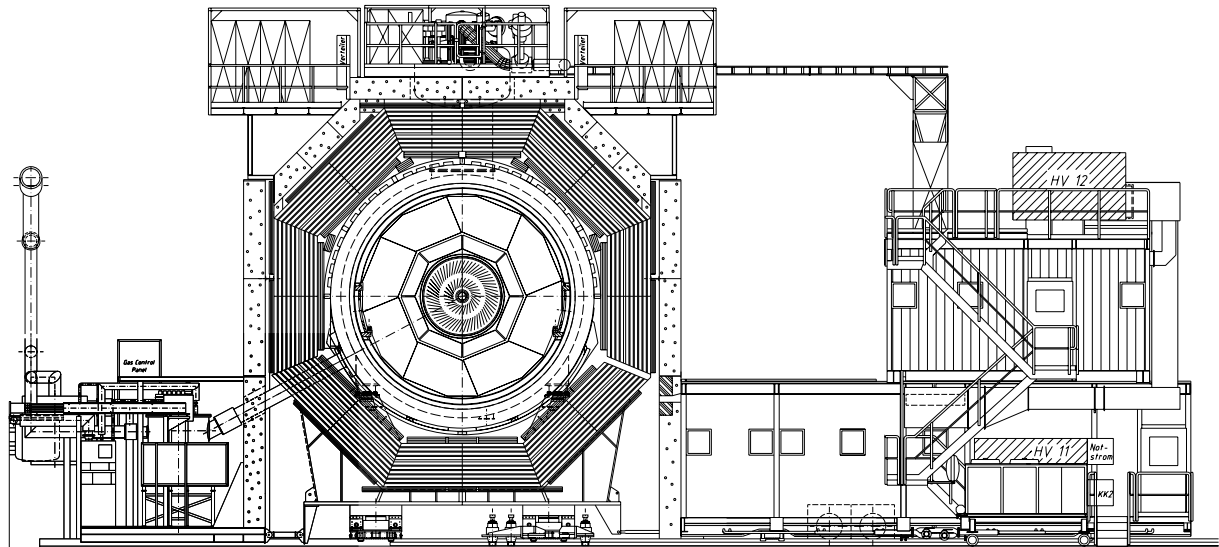
Figure 3.2: Transverse cut through the H1–detector at the center of the inter-action region.

Calorimetry		
Main calorimeter: liquid Ar	Electromagnetic part	Hadronic part
Granularity	10 to 100 cm^2	50 to 2000 cm^2
Depth (number of channels)	20 to 30 X_0 (30784)	4.7 to 7 λ_{abs} (13568)
Resolution $\sigma(E_{e,h})/E_{e,h}$	$12\%/\sqrt{E_e} \oplus 1\%$	$\approx 50\%/\sqrt{E_h} \oplus 2\%$
LAr purity (stability of el. calibration)	$\leq 0.2\%$ over one year (one month)	
Noise per channel	10 to 30 MeV	
Angular coverage – dead channels	$4^\circ < \vartheta < 153^\circ$	$< 0.3\%$
Backward calorimeter: Pb–scintillator		
Angular coverage – granularity	$151^\circ < \vartheta < 177^\circ$	16×16 cm^2
Depth – resolution $\sigma(E_e)/E_e$	22.5 X_0 (1 λ_{abs})	$10\%/\sqrt{E_e} \oplus 2\,[1]\%$
Tail catcher: iron–streamer tubes		
Angular coverage	$4^\circ < \vartheta < 177^\circ$	
Depth – resolution $\sigma(E_h)/E_h$	4.5 λ_{abs}	$100\%/\sqrt{E_h}$
Plug calorimeter: Cu–Si		
Angular coverage – granularity	$0.7^\circ < \vartheta < 3.3^\circ$	5×5 cm^2
Depth – resolution $\sigma(E_h)/E_h$	4.25 λ (44.6 X_0)	$\approx 150\%/\sqrt{E_h}$
Electron tagger: Tl(Cl/Br)		
Angular coverage – granularity	$\vartheta > 179.7^\circ$	2.2×2.2 cm^2
Depth – resolution $\sigma(E_e)/E_e$	21 X_0	$\approx 10\%/\sqrt{E_e} \oplus 1\%$

Tracking		
Coil: radius – field	3 m – $B = 1.15$ T, $\Delta B/B \leq 2\%$	
Central tracking		
Angular – radial coverage	$25^\circ < \vartheta < 155^\circ$	$150 < r < 850$ mm
Jet chamber: spatial resolution	$\sigma_{r\varphi} = 170\,\mu$m	$\sigma_z = 22.0$ mm
z-chambers: spatial resolution	$\sigma_{r\varphi} = 25$ and 58 mm	$\sigma_z \approx 350\,\mu$m
Momentum – dE/dx resolution	$\sigma_p/p^2 < 0.01\,[0.003]$ GeV^{-1}	$\sigma(dE)/dE = 10\,[6]\%$
Forward/backward tracking		
Angular – radial coverage (forward)	$7^\circ < \vartheta < 25^\circ$	$120 < r < 800$ mm
Spatial resolution (forward)	$\sigma_{r\varphi} = 170\,\mu$m ($\sigma_r = 29$ mm)	$\sigma_{x,y} = 210\,\mu$m
Angular coverage – resolution (barrel)	$155^\circ < \vartheta < 175^\circ$	$\sigma_{x,y} = 1$ mm
Trigger proportional chambers		
Angular coverage – channels	$7^\circ < \vartheta < 175^\circ$	3936

Muon detection		
Instrumented iron		
Angular coverage – total area	$4^{\circ} < \vartheta < 171^{\circ}$	4000 m^2
Number of channels	wires: 103700, strips: 28700, pads: 4000	
Spatial resolution	$\sigma_{wire} = 3 - 4$ mm	$\sigma_{strip} = 10 - 15$ mm
Angular–momentum resolution barrel	$\sigma_{\vartheta}(\sigma_{\varphi}) = 15(10)$ mr	$[\sigma_p/p \approx 0.35]$
Forward muon toroid		
Angular coverage – resolution	$3^{\circ} < \vartheta < 17^{\circ}$	$[0.25 < \sigma_p/p < 0.32]$
Overall size (x, y, z) – weight	$12 \times 15 \times 10$ m^3	2800 t

Table 3.1: Summary of H1–detector parameters. The actual status of HERA has been given. Alternatively design and test beam figures have been given in brackets []. Energies are given in GeV.

In the following, those detector parts which are of some importance for the analysis of this work are described in more details.

3.1 Tracking

The tracking system of H1 provides simultaneous track triggering, reconstruction and particle identification for the event topology particular to HERA electron proton collisions. It has been designed to reconstruct jets with high particle densities and to measure the momentum and angles of scattered isolated charged particles to a precision of $\sigma_p/p^2 \approx 3 \times 10^{-3}$ GeV^{-1} and $\sigma_{\vartheta} \approx 1$ mr.

Because of the asymmetry between the electron and proton beam energies many charged particles are produced at small angles ϑ to the incident proton (forward) direction. To maintain good efficiency for triggering and reconstruction over the whole solid angle, we divide the tracking system between the central and forward regions (see fig 3.3). Two mechanically distinct tracking detectors have been constructed, the central (CTD) and forward (FTD) trackers, respectively. Each is optimized for tracking and triggering in its angular region.

Track reconstruction in the central region (see fig 3.4) is based on two large concentric drift chambers, CJC1 and CJC2. The chambers have wires strung parallel to the beam axes (z-direction) with the drift cells inclined with respect to the radial direction. We have measured a space point resolution of 170 μm in the drift coordinate ($r\varphi$ plane) and can, by comparing signals read out at both wire ends, achieve a resolution of one percent of the wire length in z. From the signals recorded in these chambers the transverse track
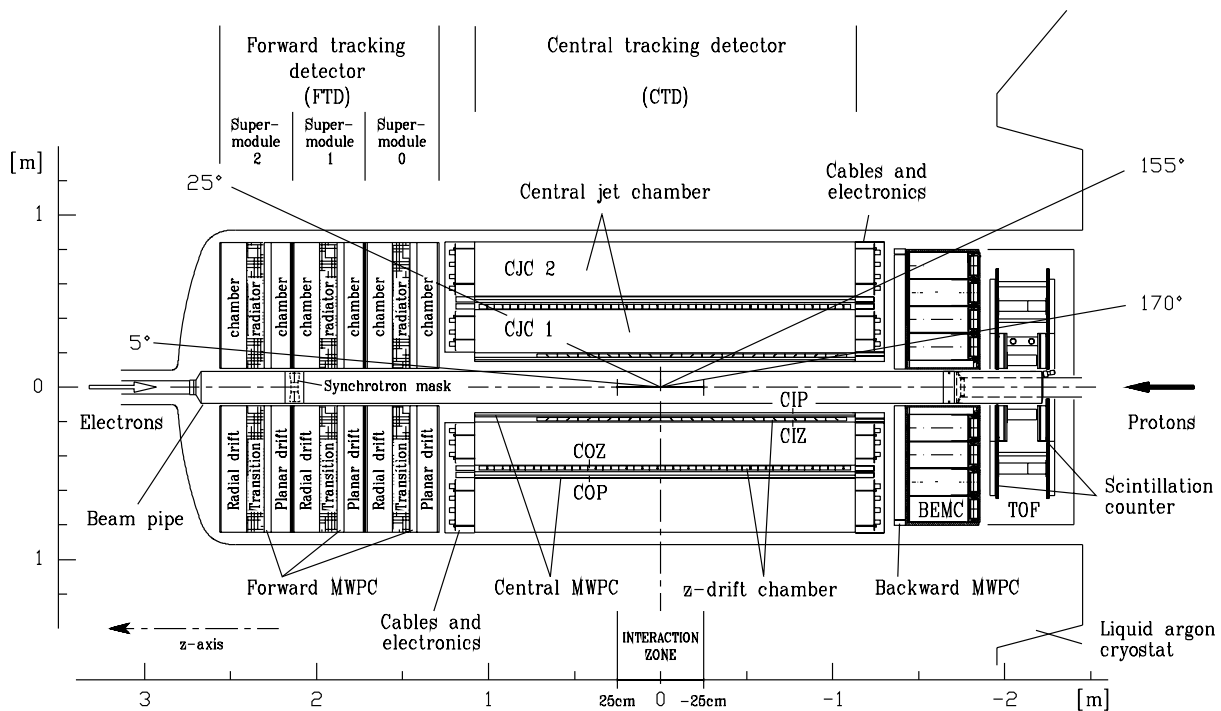
Figure 3.3: The H1–tracking system (rz view).

momentum is determined and in addition the specific energy loss dE/dx is used to improve particle identification.

Two thin drift chambers, the central inner (CIZ) [48] and central outer (COZ) z–chambers complement the measurement of charged track momenta in the central chambers. The CIZ chamber fits inside CJC1, and the COZ chamber fits in between CJC1 and CJC2. These two chambers deliver track elements with typically 300 μm resolution in z and 1 to 2% of 2π in φ. This requires a drift direction parallel and sense wires perpendicular to the beam axis.

3.2   Trigger chambers

For trigger purpose, several multiwire proportional chambers (MWPC) are used for a fast first level (L1) distinction of genuine ep events from background events [49, 50]. Their signals provide space points of traversing particles, which allow a fast, coarse estimation of the position of the event vertex along the beam axis. These are the central inner proportional chamber (CIP), the central outer proportional chamber (COP) and the forward proportional chambers (FPC). While CIP and COP are cylindrical chambers situated around the beam axis, FPC is a planar chamber, located in proton direction,
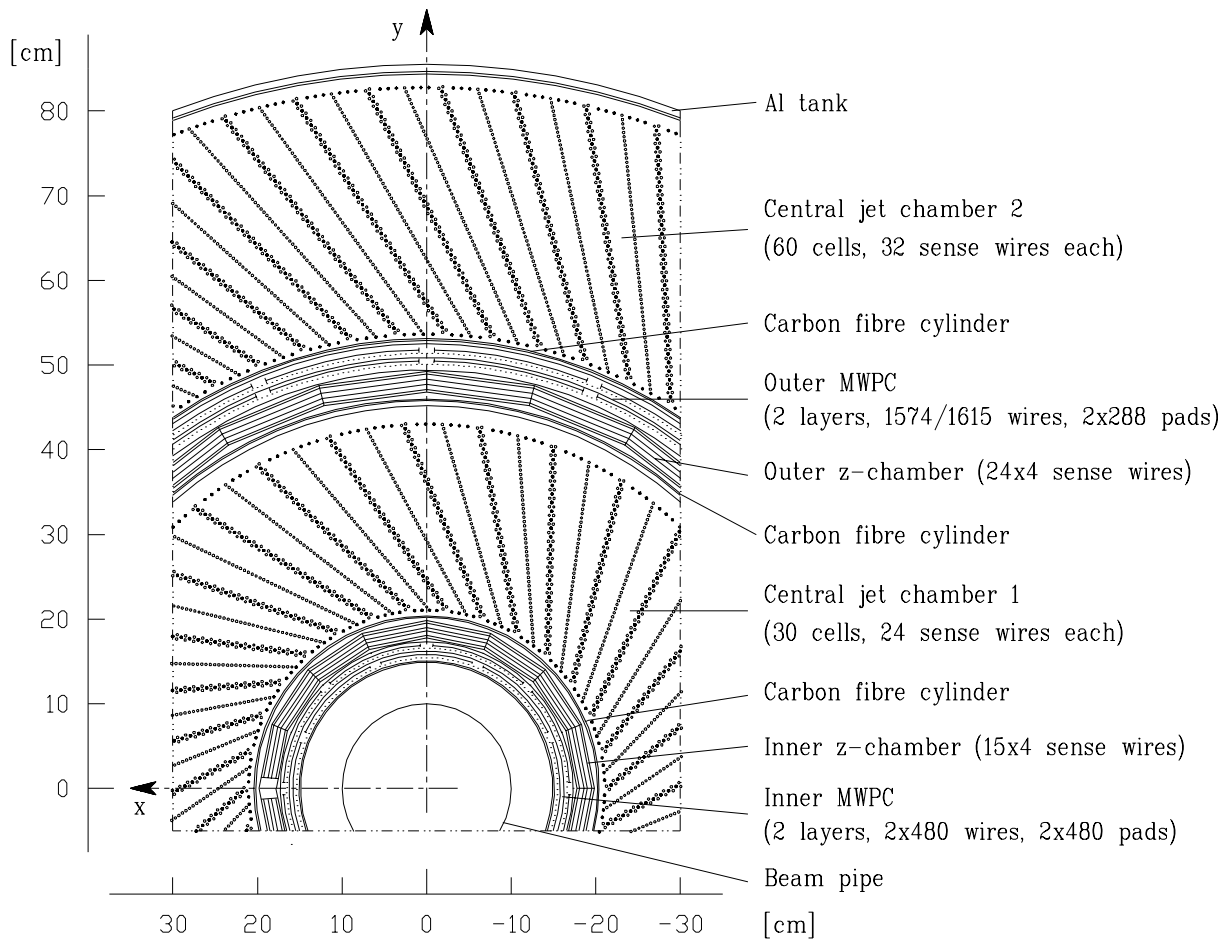
Figure 3.4: Central tracking system, section perpendicular to the beam line.

perpendicular to the beam axis. Each chamber consists of two independent layers.

CIP This chamber is described in detail in [51], therefore only important points are discussed here. CIP consists of two cylindrical chambers and has an active length of 2190 mm and radius to the inner (outer) anode wires of 157 mm (166 mm). With the ep interaction point in the middle, it covers a ϑ region from 8° to 172°. Induced signals, from particles depositing charge at the anode wire, couple to the cathode foil, which is segmented into pads. Both, inner and outer CIP contain each 480 pads with a 60-fold segmentation along z and a 8-fold segmentation in φ. The inner chamber is rotated in φ by 22.5° with respect to the outer one which results in an effective 16-fold segmentation in φ. The signals from the pads are preamplified directly on the chambers and transported to the electronic trailer outside the H1 detector. 480 anode wires are connected to positive high voltage. Each high voltage supply feeds 30 adjacent anode wires resulting in a 16-fold high voltage segmentation in φ. Therefore, defective sectors can be degraded in voltage in steps of half a pad.

COP This chamber follows closely the construction of CIP. Differences occur in size and number of pads. With its three times larger radius, COP surrounds the whole CIP.

FPC The 6 forward proportional chambers are planar, ring shaped chambers. Its cathode pads are correspondingly ring shaped and cover an azimuthal angle of $\pi/8$ each, except for the four outermost of the 20 rings where they cover $\pi/16$. The radial pad width increases with radius in geometrical progression between 18 and 37 mm. Two consecutive cathode planes are offset by one half of a ring, such that the effective polar angle resolution is halved.

Additional first level track triggers are derived from driftchamber signals.

Table 3.2 summarizes some important properties of the trigger chambers.

	unit	CIP inner/outer	COP inner/outer	FPC #1/#2/#3
active length $\Delta z/\Delta r$[1]	mm	2190	2172	583
active zone starts at z/r[1]	mm	-1125	-1107	167
position of first anode r/z[1]	mm	157/166	501/514	1451/1875/2297
number of wires		480	1574/1615	724
wire separation	mm	2.1/2.2	2.0	2.5
gap width[2]	mm	3.0	4.0	4.0
number of cathode pads		480	288	384
length of pad $\Delta z/\Delta r$[1]	mm	36.6	120	13 to 54
width of pad $\Delta\varphi$	o	45	22.5	45 (22.5)[3]

Table 3.2: Trigger chamber parameters. The separate columns for CIP and COP refer to the two planes, for the FPC to a whole module containing two planes.
[1] First coordinate for CIP and COP, second for FPC.
[2] Distance between anode and cathode plane.
[3] Only for the four outermost of the 20 radial pads.

3.3   Calorimetry

To provide a clear identification and precise measurement of electrons, muons and penetrating neutral particles together with very good performance in the measurement of jets with high particle densities a calorimeter inside a large coil is used. This minimizes both, the amount of dead material in front of the electromagnetic calorimeter and the overall size and weight of the calorimeter.

Using a liquid argon technique eases calibration and provides a good stability as well as homogeneity of response. A fine granularity is needed for e/π separation and energy flow measurements.

A longitudinal view of the H1–calorimeters is shown in fig 3.5.

The liquid argon calorimeter covers the polar angular range between $\vartheta = 4^{\rm o}$ and $\vartheta \approx 153^{\rm o}$. The calorimetric coverage is completed with a small calorimeter in the proton direction (PLUG) with copper absorber and silicon pad readout, covering the region between the beam-pipe and the liquid argon cryostat ($\vartheta \leq 4^{\rm o}$) and a lead scintillator backward electromagnetic calorimeter (BEMC) located in the electron direction after the tracker and covering $151^{\rm o} \leq \vartheta \leq 177^{\rm o}$.

The segmentation along the beam axis is done in eight self supporting *wheels* as shown in fig 3.5, each of them segmented in φ into eight identical stacks or octants.
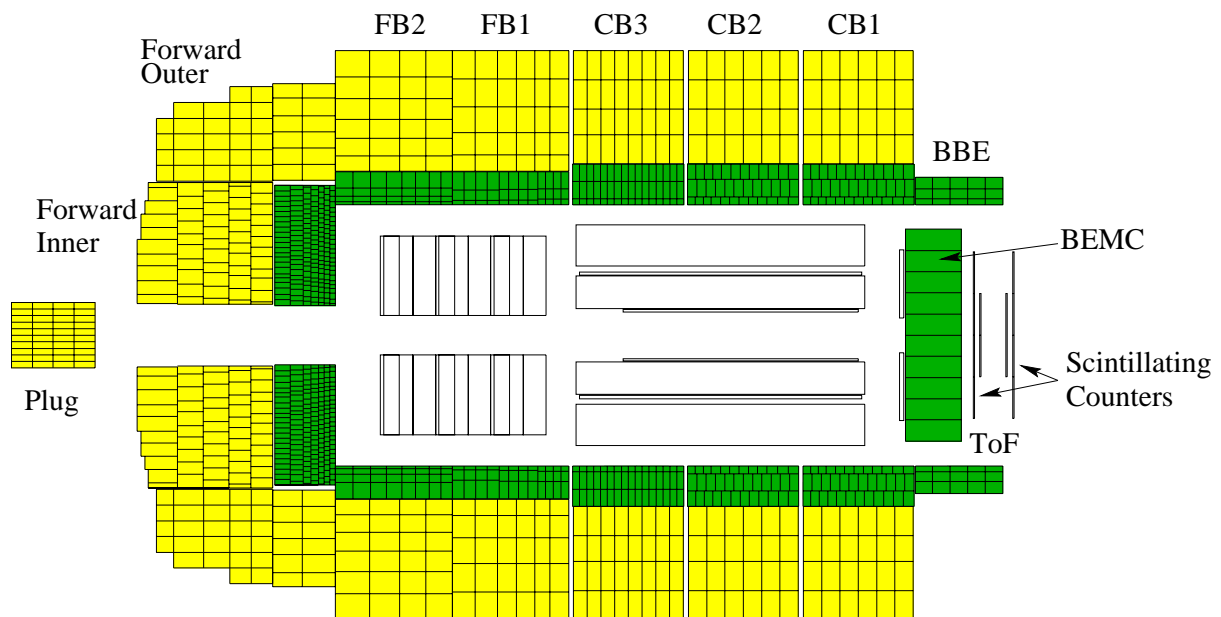
Figure 3.5: Longitudinal view of calorimeters showing the readout cells of the eight wheels (*Forward Inner* ... *BBE*) in the central part, the PLUG in forward direction and the BEMC in backward direction.
light-gray: hadronic part
dark-gray: electromagnetic part

3.4   Luminosity system and electron tagger

The luminosity is determined from the rate of Bethe-Heitler events $e + p \rightarrow e + p + \gamma$ [52]. The main source of background is bremsstrahlung from the residual gas in the beam pipe, $eA \rightarrow eA\gamma$. At design luminosity these events are expected at 10% of the $ep \rightarrow ep\gamma$ rate, but can be subtracted using data from electron pilot bunches. The luminosity is calculated as

$$\mathcal{L} \ = \ \frac{R_{tot} - (I_{tot}/I_0)R_0}{\sigma_{vis}}$$

where R_{tot} is the total rate of the bremsstrahlung events, R_0 is the rate in the electron pilot bunches, I_{tot}, I_0 are the corresponding electron beam currents and σ_{vis} is the visible part of the $ep \rightarrow ep\gamma$ cross section with acceptance and trigger efficiency included.

The luminosity system detects scattered electrons and outgoing photons in coincidence. It contains therefore two arms: the electron tagger (ET) and the photon detector (PD). Since the angular distributions for both the electrons and photons are strongly peaked in the direction of the primary e-beam – at 30 GeV polar angles are of the order of $\vartheta \simeq \mathcal{O}(m/E) \simeq 17 \, \mu\mathrm{rad}$ – the detectors are placed close to the beamline and very far from the interaction region in order to cover these small angles.

The general view of the luminosity system is shown in Fig. 3.6. Scattered electrons are deflected by a set of low-beta quadrupoles and a bending magnet located in the region $5.8 \, \mathrm{m} < -z < 23.8 \, \mathrm{m}$, pass an exit window at $-z = 27.3 \, \mathrm{m}$ and hit the ET at $-z = 33.4 \, \mathrm{m}$. The photons leave the proton beam pipe through a window at $-z = 92.3 \, \mathrm{m}$, where the beam pipe bends upward, and hit the PD at $-z = 102.9 \, \mathrm{m}$. A Pb filter ($2 \, X_0$) followed by a water Čerenkov ($1 \, X_0$) veto counter (VC) protects the detector from the high synchrotron radiation flux. From the p-beam side the PD is shielded by an iron wall of 2 m thickness. The VC eliminates events with photons interacting in the filter.
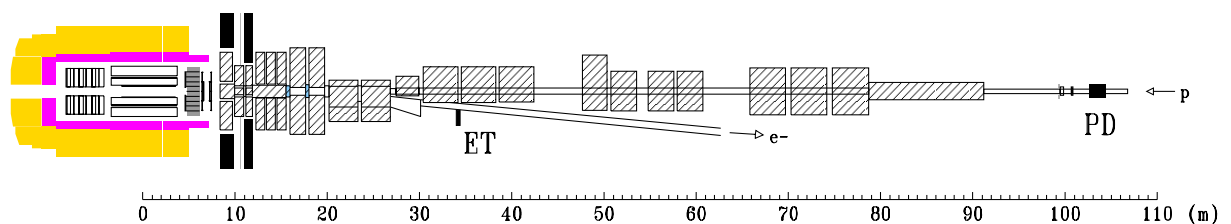
Figure 3.6: The luminosity system (The H1–detector is not in scale).

The acceptance of the luminosity system for nominal electron beam conditions ($E_e = 30$ GeV, zero tilt) and the expected rates at the design luminosity of $1.5 \times 10^{31} \, \mathrm{cm^{-2}s^{-1}}$ are given in the Table 3.3. One of the main contributions to the systematic error in the absolute luminosity stems from the dependence of the system acceptance on possible

variations of the electron beam angle in the interaction region. This tilt, typically of the order of 100 μrad, is controlled by the position of the beam profile at the PD with high precision, of the order of 10 μrad. The corresponding corrections to σ_{vis} are taken into account already online and can be further improved during the offline analysis.

	unit	ET	PD
Energy interval, $E_\gamma/E_e = 1 - E'_e/E_e$		$0.2 - 0.8$	$0.004 - 1.0$
Polar angle acceptance interval	mr	$0 - 5$	$0 - 0.45$
Average acceptance for $ep \rightarrow ep\gamma$ events	%	48	98
Average acceptance for photoproduction events	%	36	$-$
Visible $ep \rightarrow ep\gamma$ cross section	mb	28	174
$ep \rightarrow ep\gamma$ event rate[1]	MHz	0.4	1.3
Photoproduction event rate [1]	Hz	$20 - 30$	$-$
Aperture $x \times y$ (granularity)	mm^2	154×154 (7×7)	100×100 (5×5)
Chemical composition		TlCl(78%) + TlBr(22%)	
Radiation length (Moliere radius)	cm	0.93 (2.10)	
Crystal length (radiation hardness)	cm (Rad)	$20 (> 6 \cdot 10^7)$	
Energy resolution, σ_E/E		$1 \oplus 10/\sqrt{E}$, (E in GeV)	
Position (time) resolution, $\sigma_{x,y}$ (σ_t)	mm (ns)	$0.3 - 1.2$ (< 3)	

Table 3.3: Parameters of the luminosity system. [1] for $E > E_{thr} = 4$ GeV at design luminosity.

Quasi-real photoproduction events with $Q^2 < 0.01$ GeV^2 can be tagged by ET in the energy interval $0.2 < E'_e/E_e < 0.8$ using both PD and VC as a veto.

3.5   Time of flight

The time of flight hodoscope (ToF) consists of two planes of 3 cm NE102A scintillator mounted perpendicular to the beam pipe upstream of the interaction region (see fig 3.3 and fig 3.5). Particles from proton induced background and from ep collisions are separated in time at this point by ~ 13 ns. The electron bunches have negligible size whereas the proton bunches are spread over 2 to 3 ns FWHM. The plane nearest the interaction point (ToF1) lies at $z = -1.95$ m and has 16 butted counters, measuring 317×317 mm^2 thus matching the size of four BEMC stacks. The outer plane at $z = -2.25$ m consists of eight larger counters $(317 \times 634$ mm$^2)$.

Each wall of ToF is made up of a sandwich of scintillator and lead, mounted on a backing plate of non-magnetic steel to minimize stresses from the large magnetic field. The lead is 6.5 mm thick to absorb synchrotron radiation, both to protect the counters from damage and to limit the number of triggers from this source. Eddy currents, produced during a magnet quench must be minimized, so steel is used rather than aluminum.

Signals produced by the PM's are amplified ($\times 40$), up to ~ 1 V before traveling down 29 m of cable to NIM logic located in the electronics trailer. Here the signals are discriminated and strobed in three time windows: background, interaction and global, which are used in the first level trigger decision.

3.6   Trigger

The purpose of the trigger system is to select interesting ep collision events and to reject background events. Background events are mainly beam induced and orders of magnitude higher than the rate of ep collisions. Background events can be subdivided into following classes:

Proton beam–pipe interactions Off momentum protons may hit the beam pipe preferably at the collimators. Showers of secondary particles are produced, which enter the H1 detector.

Proton gas interactions Protons may hit residual gas molecules within the vacuum of the beam pipe. The cross section for such reactions is in the order of $A^{2/3} \cdot 40$ mb, with A being the atomic mass of the hit nucleon within the residual gas molecule. The total rate of proton–gas interactions is determined by the intensity of the incoming protons, the cross section and the number of gas targets. At design luminosity and at a vacuum of 10^{-7} Pa a rate of 1 kHz per meter along the beam pipe can be estimated. The quality of the vacuum suffers from synchrotron radiation, originating from the electron beam, hitting the beam pipe.

Electron beam–pipe interactions These are of little importance due to the smaller beam current and the better focusing properties of the electron beam optics.

Electron gas interactions The cross section for electron–nucleon interactions is in the order of α_{em} suppressed with respect to proton–nucleon interactions, in addition the intensity of the electron beam is much lower than the intensity of the proton beam. These events are therefore not a problem for triggering but for offline analysis, as they look similar to deep inelastic scattering events with a high energy electron within the H1 detector.

Synchrotron radiation In order to achieve collisions between electrons and protons under a crossing angle of π, the electron ring is bent just a few meters in front of the interaction region. This results in synchrotron radiation becoming visible within the H1 detector.

Cosmic rays A cosmic muon crossing the interaction zone of the H1 detector can be mistaken as two muon tracks originating from the H1 interaction region faking a leptonic decay of mesons such as J/ψ.

To deal with the low ep cross section, large proton and electron beam currents are needed, which is realized by running in a multi bunch mode. Every 96 ns a proton bunch collides head on with its corresponding electron bunch. This time interval is referred as bunch–crossing time, 1 BC $\widehat{=}$ 96 ns. This short time interval, together with the huge background rate is a challenge for triggering, therefore a fast complex trigger using several levels with increasing complexity has been achieved. Each subsequent level is only started if a given event has been accepted by the preceding decision logic. The first level trigger (L1) runs completely deadtime free, which is only possible due to the pipelined architecture of the H1 readout electronics. Every bunch–crossing (BC), the full information gained in H1 is stored in memory within the front end electronics and simultaneously fed to the first level trigger. The information of previous events is shifted by one step and the oldest information is dropped. Depending on the subdetector, the full information of 27 to 5 events can be subsequently stored (pipelined). The final L1 decision, built by a central trigger logic out of 9 different trigger systems, based on the information of the subdetectors, is available 24 BC after the real ep event time. Only in case of an *L1keep* decision, all pipelines in the front–end electronics are stopped and the event topology is further analyzed by the subsequent trigger levels. As the probability for a real ep–reaction is in the order of 10^{-4} per bunch–crossing no further ep–data is expected in the pipelines and no deadtime is accumulated during the first level trigger step.

During the 1994 data taking period, level two and three were not fully operational and the final trigger decision was taken at level four.

Level four (L4) is an asynchronous software trigger based on 30 fast mips R3000 processor boards [53], which build together the L4 filter farm. It is integrated into the central data acquisition system and has the raw data of the full event available. Each board processes one event completely, where fast reconstruction code analyses the event topology and sophisticated algorithms provide an accurate decision.

An event which passes L4 is finally kept and written to tape. A final reconstruction and classification according the topology of the event is performed offline in a later step (L5).

Table 3.4 gives an overview of the H1 trigger levels and fig 3.7 shows a schematic overview of the trigger system.
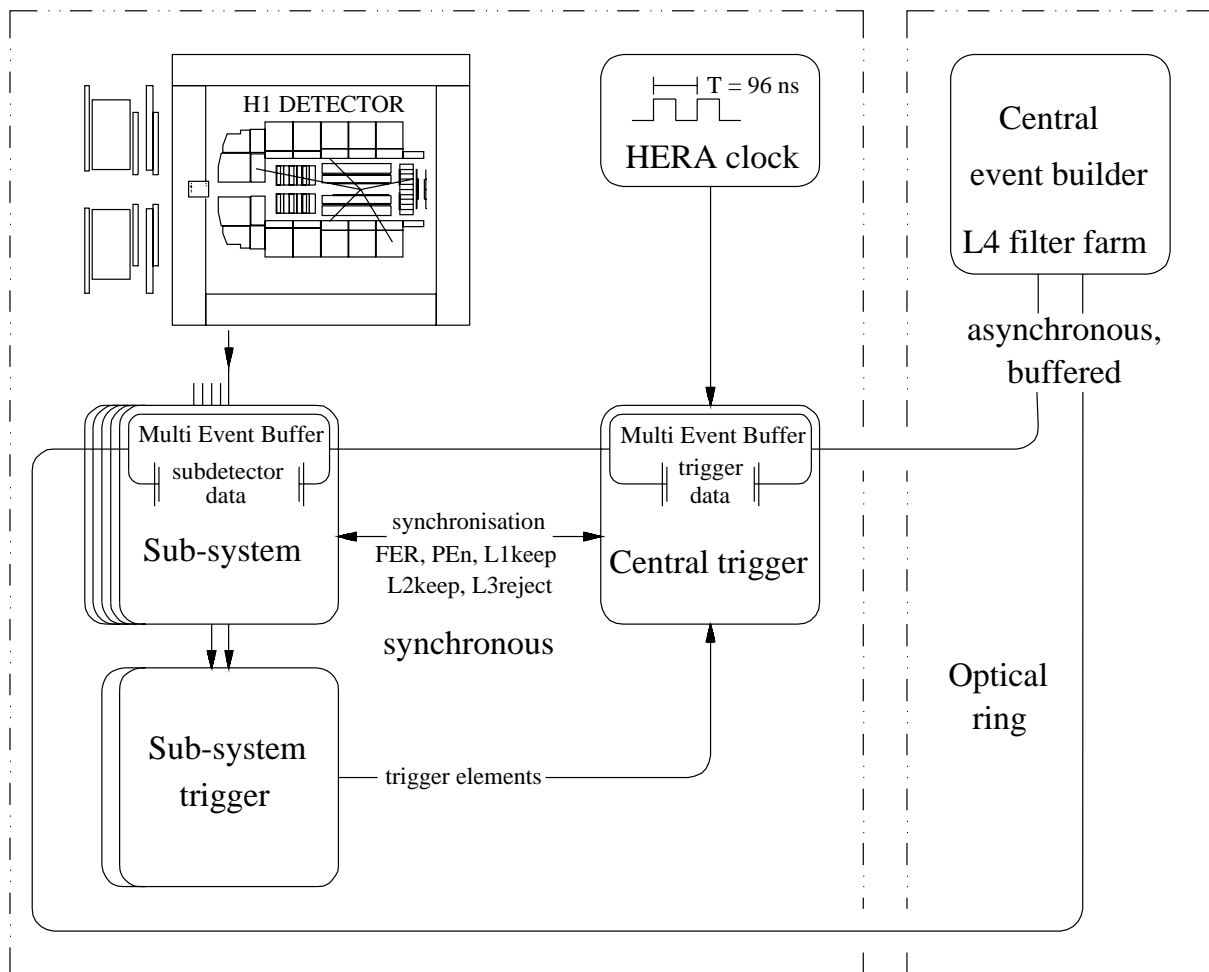
Figure 3.7: Overview of the H1 trigger system.

3.7   Data acquisition

For a triggered event, a total of over a quarter of a million analogue channels are read-out and digitized, resulting in some 3 Mbyte of raw digitized information. As the time between successive electron-proton bunch–crossings is just 96 ns, various levels of hardware triggering, software filtering and digital compression are employed before the final data size is reduced to acceptable storage–media recording rates. The information is digitized and read-out in parallel from many subdetector parts before being finally merged. Data compression and formatting reduce the 3 Mbyte of raw data to event sizes of between 50 Kbyte and 100 Kbyte so that final data recording rates are not restricted at the presently maximum bandwidth of 1.2 Mbyte/s.

For the data acquisition several hundred processing elements are embedded largely within the IEEE VMEbus standard [54]. The readout system of each branch is autonomous up

trigger level	level 1	level 2	level 3	level 4	level 5
Maximum decision time	2.5 μs	20 μs	800 μs		
Input event rate	$\approx$ 50 kHz			50 Hz	5 - 10 Hz
Output event rate	50 Hz			5 - 10 Hz	5 - 10 Hz
Designed output rate	1 kHz	200 Hz	50 Hz	5 - 10 Hz	5 - 10 Hz
Introduced dead time	0 μs	20 μs	< 800 μs		
Data	from own subtrigger system	from all subtrigger systems	from all subtrigger systems	from all detectors	from all detectors
Implementation	hardware, front end subsystem, synchronous	hardware, front end subsystem, synchronous	software, front end processor, synchronous	software, 30 R3000 processors, asynchronous	SGI challenge, asynchronous
Action	stop data pipelines	start data readout	start event building or abort data readout	verification of trigger decision, event filtering	event reconstruction and classification

Table 3.4: Overview of H1 trigger levels. On five subsequent trigger levels the event topology is analyzed with increasing complexity of the analyzing algorithm. Level 1 to level 4 are online filters, whereas level 5 is an offline filter and is therefore sometimes a few days behind the actual data taking.

to and including a central subdetector VMEbus crate. Each central subdetector crate contains a dedicated supervisory readout controller, a multi-event buffer (MEB), a VMEtaxi and any input drivers necessary to access the data as illustrated in fig 3.8. This design allows a particular subdetector to be decoupled from the rest of the system, during installation and test phases, or due to malfunctioning of specific parts within a subdetector when data taking is going on. An event coordinator management task runs on the master VMEtaxi of the ring and interacts with each readout controller via shared memory blocks. During acquisition, when it is free for event building, it searches the subdetector multi-event buffers for the next event. When all branches are ready with the same event number, the raw data is transferred via an optical ring into a full-event buffering system
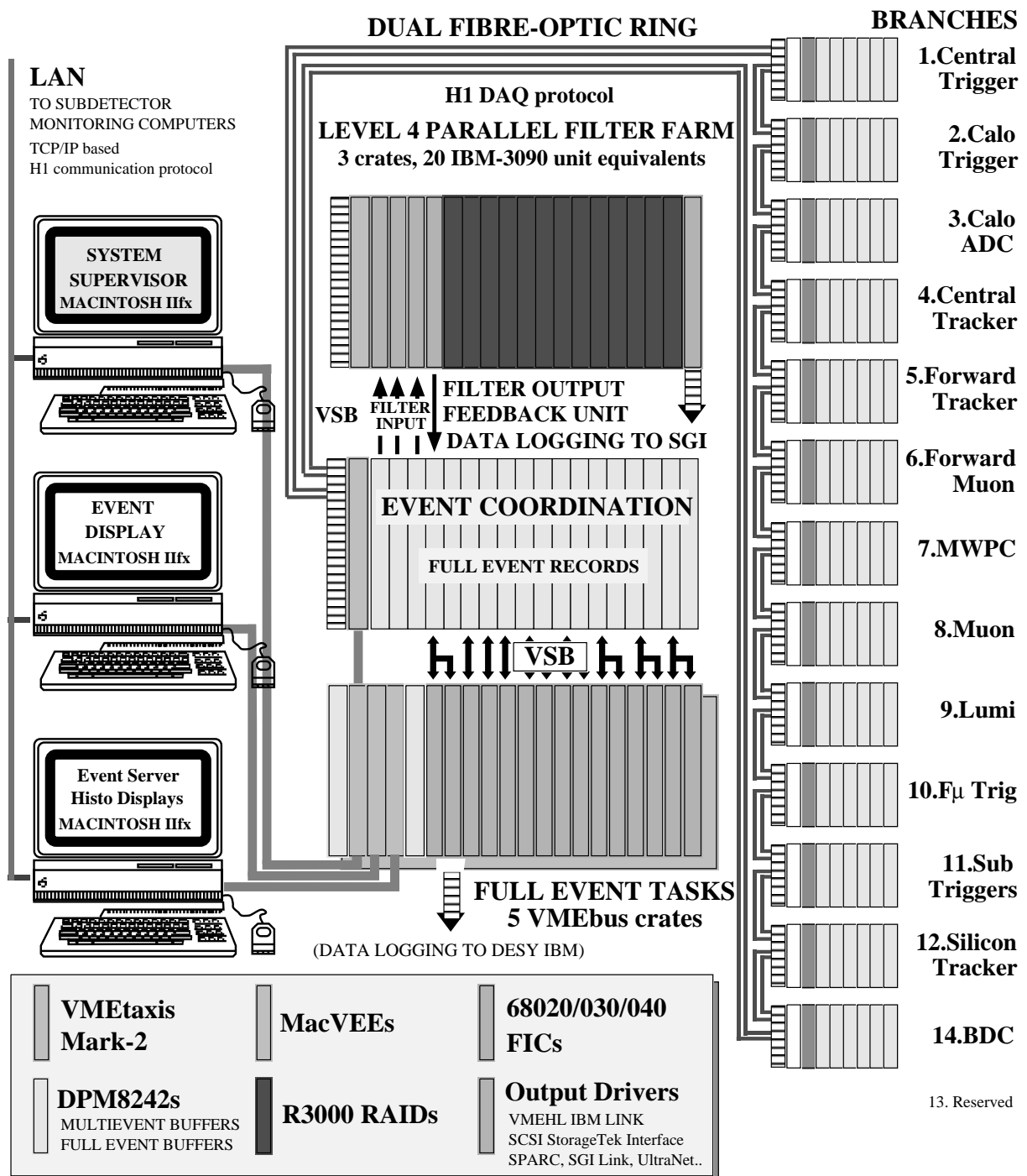
Figure 3.8: Layout of the H1 data acquisition. Each subdetector is decoupled from the others via an own readout branch. A dual fiber optic ring transfers all raw data to the event coordinator, where the data is assembled into full events and then handed to the L4 filter farm. In case L4 accepted the event, it is transfered to the data logging task running on a SGI computer at DESY side, some 3 km away from the location of the H1 experiment.

(FEB). Since the memory has read and write access from both the event task processors and the event coordinator, data can also be fed back into the system, for example, from the filter farm. The final event records are sent to a Silicon Graphics (SGI) computer at DESY, at rates of up to 7 Mbyte/s.

3.8   Computing environment

Cross sections for various physics processes at HERA and the resulting data rates are presented in table 3.5, assuming an instantaneous luminosity of 10^{31} cm^{-2}s^{-1}.
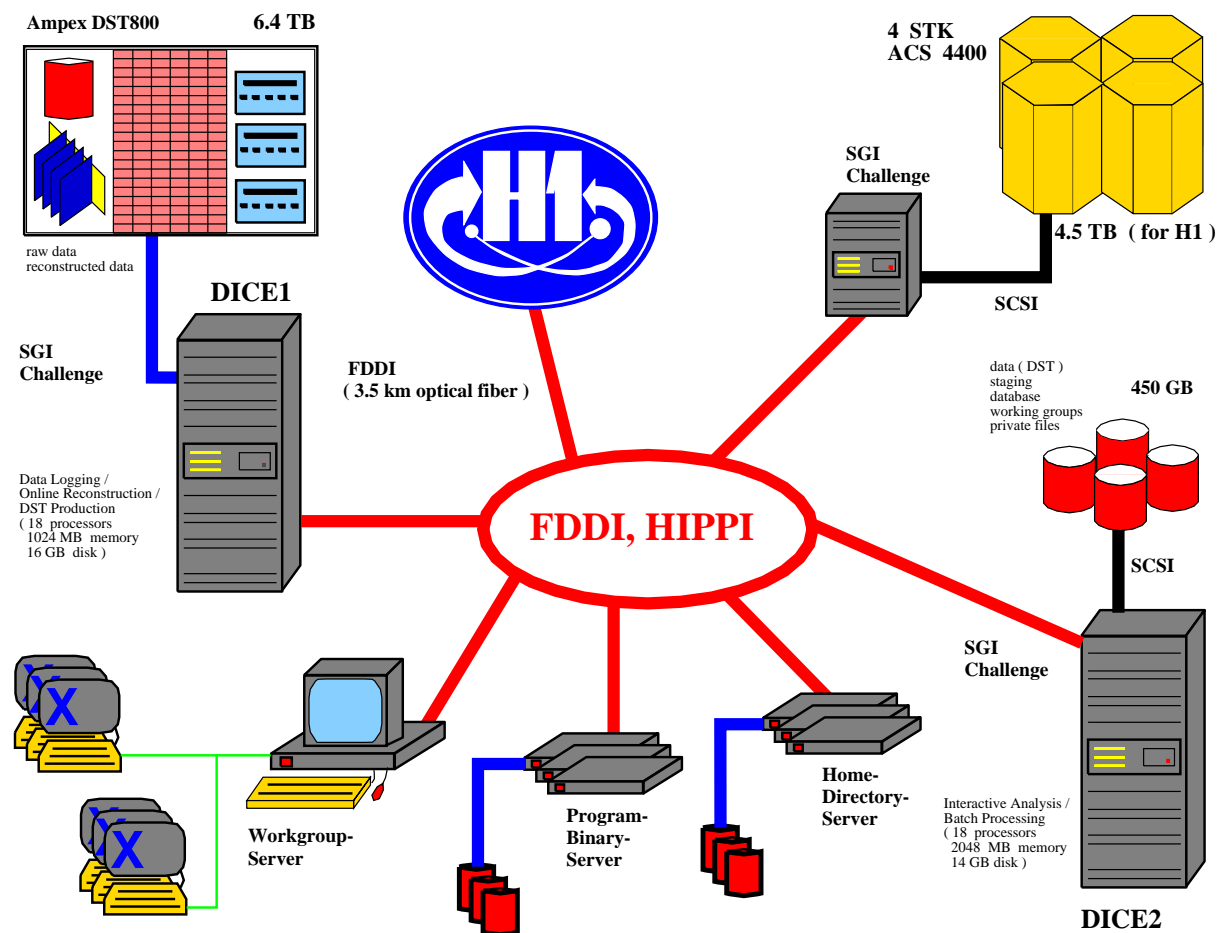
Figure 3.9: Computing environment of the H1 experiment.

Assuming effectively 10^7 s of H1 operation, this results in a yearly data volume of 10^8 events corresponding a raw data volume of ~ 5 TB, which have to be stored, analyzed and have to be accessible to the H1 community [55]. The reconstructed and classified events occupy another ~ 3 TB from which the for *ep* physics interesting candidates

process	cross section	event rate
γp	20 μb	$\mathcal{O}(100$ Hz$)$
$c\bar{c}$	1 μb	$\mathcal{O}(10$ Hz$)$
NC	100 nb	$\mathcal{O}(1$ Hz$)$
$b\bar{b}$	5 nb	$\mathcal{O}(0.1$ Hz$)$
CC	0.1 nb	$\mathcal{O}(0.001$ Hz$)$
p induced background		$\mathcal{O}(100$ kHz$)$

Table 3.5: Visible cross sections and data rates for various physics processes

are extracted, which leads to another $\sim$ 150 GB of data. To handle such amounts of data is only possible using a large and powerful computing environment as shown in figure 3.9. The main computing facilities are provided by two SGI Challenge XL computers with 18 MIPS R4400 processors each, used for *online* purpose (data logging, online reconstruction, reprocessing) and *analysis* purpose (batch and interactive).

Chapter 4

The z–Vertex trigger

In this chapter, all aspects of the z–Vertex trigger are described which occur offline, when data has to be analyzed which has been triggered by this device. The z–Vertex trigger in its content and assembly is described elsewhere [50, 49]. To prove the reliability of the z–Vertex trigger, a fully automatically scheme has been realized, which provides a quasi online monitoring of the hardware reliability of the z–Vertex trigger.

4.1 Principle of operation of the z–Vertex trigger

The z–Vertex trigger is entirely based on multiwire proportional chambers (MWPC) signals, namely the central inner proportional chamber (CIP) [51], the central outer proportional chamber (COP) and the first double layer of the forward proportional chambers (FPC). While CIP and COP are cylindrical chambers situated around the beam axis, FPC is a planar chamber, located in the proton direction, perpendicular to the beam axis. Each chamber consists of two independent layers. A total of 1920 signals, preamplified directly on their detector, transported some 35 m to the electronic trailer outside the H1 apparatus, shaped, discriminated, digitized to a unique width of 96 ns and synchronized with the global HERA clock are fed into the z–Vertex trigger hardware, from which every 96 ns the full trigger decision is built, this corresponds to a data volume of 1.9 GByte/s. The digitized and synchronized signals are stored in a pipeline, such that in case the central trigger sends an *L1keep* signal, the pipeline stops and can be read out. A schematic overview of the data flow is shown in fig 4.1.

The aim of the z–Vertex trigger is to reconstruct online the primary interaction vertex along the beam axis, the z–coordinate. This is realized by building *rays* out of the coincidence of four (optionally three) pad signals which can be connected by a straight line which points to the z–axis. To each ray unambiguously a region along the z–axis is as-
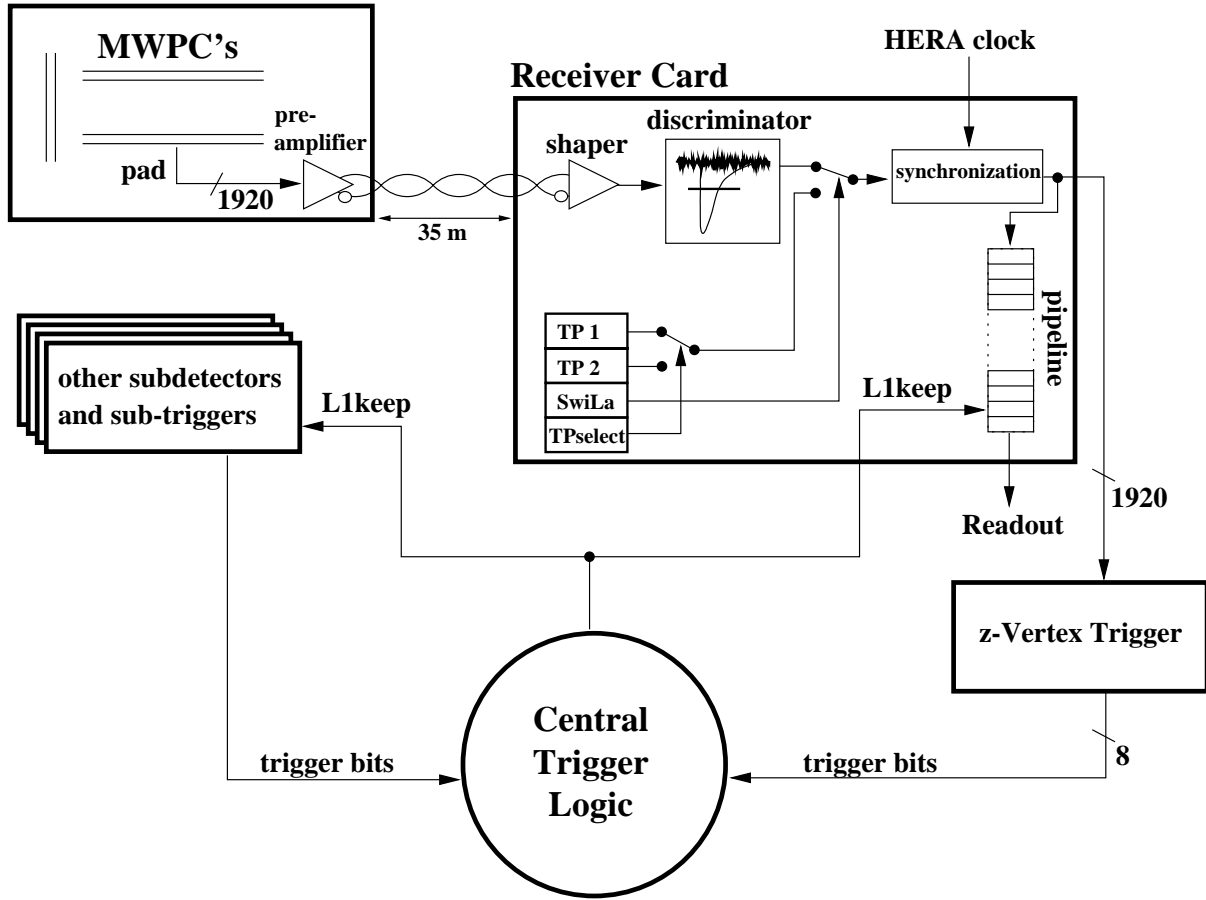
Figure 4.1: The z–Vertex trigger is one out of nine level one subtriggers of the H1 trigger system. Proportional chamber signals are first preamplified, shaped, discriminated, digitized and globally synchronized with HERA clock before they enter the z–Vertex trigger hardware. The central trigger logic compiles the L1 KEEP signal out of all trigger bits from all subtriggers.

signed which defines a bin of the z–Vertex histogram. The z–Vertex histogram consists of 16 bins with a size of 54.9 mm each, thus the the z–Vertex histogram covers a total length of 87.84 cm around the nominal interaction point. Each active ray contributes one entry to the z–Vertex histogram. The histogram bin with the most entries is expected to contain the interaction vertex of the ep collision. Figs 4.2 and 4.3 illustrate the construction of the z–Vertex histogram from the pad signals.

A block diagram, showing the implementation of the z–Vertex trigger is sketched in fig 4.4. The digitized and synchronized MWPC pad signals are distributed into 256 printed circuit boards, the *ray finder cards*. Each ray finder card is able to check about 120 rays belonging all to the same φ–segment and to the same z–Vertex histogram bin. An adder
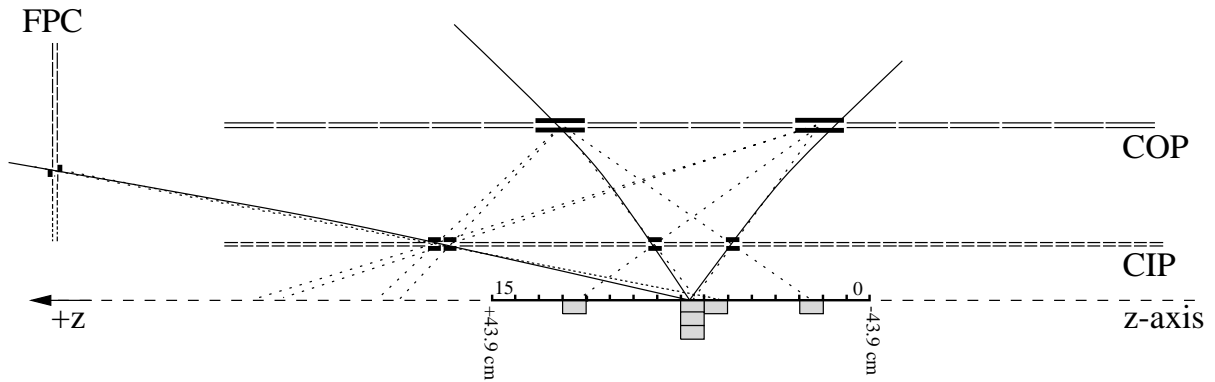
Figure 4.2: $r - z$ view of the principle of operation of the z–Vertex trigger. Four pads pointing along a straight line to the z–axis contribute one count to the z–Vertex histogram.
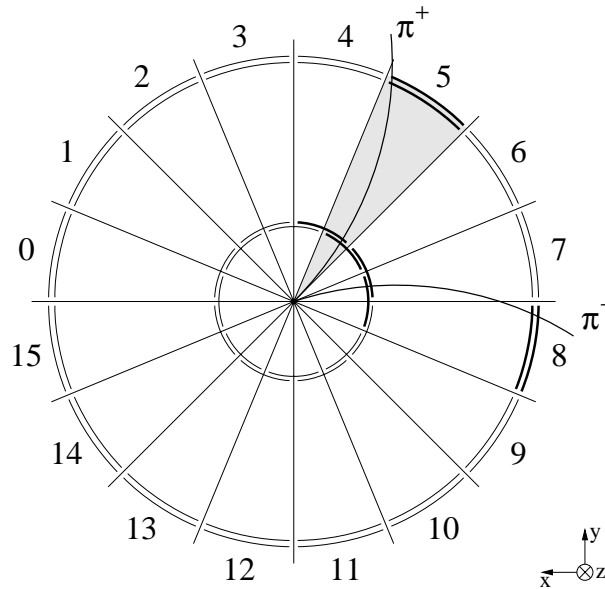
Figure 4.3: r–φ view of the principle of operation of the z–Vertex trigger. In the plane perpendicular to the z–axis a 16–fold segmentation is used, such that the rays of each segment are treated separately. Assuming a three out of four logic, the π^- track would fire a ray in φ–segment 8.

cascade calculates the sum of the active rays, which represents the number of entries in one bin of the z–Vertex histogram for segment φ. All active rays are grouped into *big ray* candidates. Big rays (and big ray candidates) have the same φ–segmentation and point to the same bin of the z–Vertex histogram as nominal rays, whereas the azimuthal angle ϑ is divided into 14 regions, such that the geometrical covering matches with the calorimeter stacks. A total of 224 big rays can be formed this way. Big rays, therefore,

represent in a somewhat coarser granulation the active rays. All big ray candidates are stored in a special pipeline that they can be used further in case of validation. Validation of big ray candidates is based on the topology of the z–Vertex histogram and the setup parameters used during loading of the hardware and is performed later in the *vertex finder card* which enables either all big ray candidates or only those pointing into a region close to the estimated vertex.

The 256 ray finder modules send their output into 16 *adder cards*, with each being responsible for one specific bin of the final z–Vertex histogram. Thus, from 16 ray finder modules, all containing the number of active rays for their specific φ–segment, the output has to be summed. A pipeline, located on each of the adder cards, stores one bin of the z–Vertex histogram.

The final histogram is analyzed on the *vertex finder card*, where the integral of the z–Vertex histogram is calculated, the location of the peak of the histogram and 2 quality bits are determined. Depending on the programmable setup of the trigger logic and the topology of the z–Vertex histogram, some of the big ray candidates get validated and are via a *big ray distribution box* available to further trigger hardware on all trigger levels.

The final decision of the z–Vertex trigger is performed on the RAM card, a special lookup table, which checks, based on the integral of the z–Vertex histogram, the number of entries at the peak location and the two quality bits, whether some predefined topological criteria of the z–Vertex histogram are fulfilled. The most important one is the z–*Vertex*–T_0 bit, which is set when at least one histogram entry was found.

Two different programs running on MacIntosh IIxi computer write hardware settings onto the receiver cards. The program RAYFIND, controlling the z–Vertex trigger hardware and the program MWPC_CONTROL, controlling the fast readout program running on the FIC front end processor [56] and all hardware settings needed to control the MWPC system. As the two programs do not share any information between each other, the hardware setting is defined by the program which last had access. This is usually the MWPC_CONTROL program, which always stores a copy of all settings into the FIC memory. Whenever a new run starts at the H1 supervisor console, the FIC reinitializes all MWPC hardware settings. This scheme makes impossible for the program RAYFIND to know about the status of the hardware when a run is going on[†]. Therefore, whenever information has been loaded into the z–Vertex trigger hardware, a copy of the relevant hardware settings is stored in the FIC memory. At runstart, the FIC sends a special runstart record which contains all setup data from both the MWPC system and the z–Vertex trigger. Whenever a run stops, a special job, the TCL job, running on the DICE1 batch computer, analyzes all non–runevent data (such as runstart records) and updates the

---

[†]except by virtue of human interference, which already proofed to be error prone.
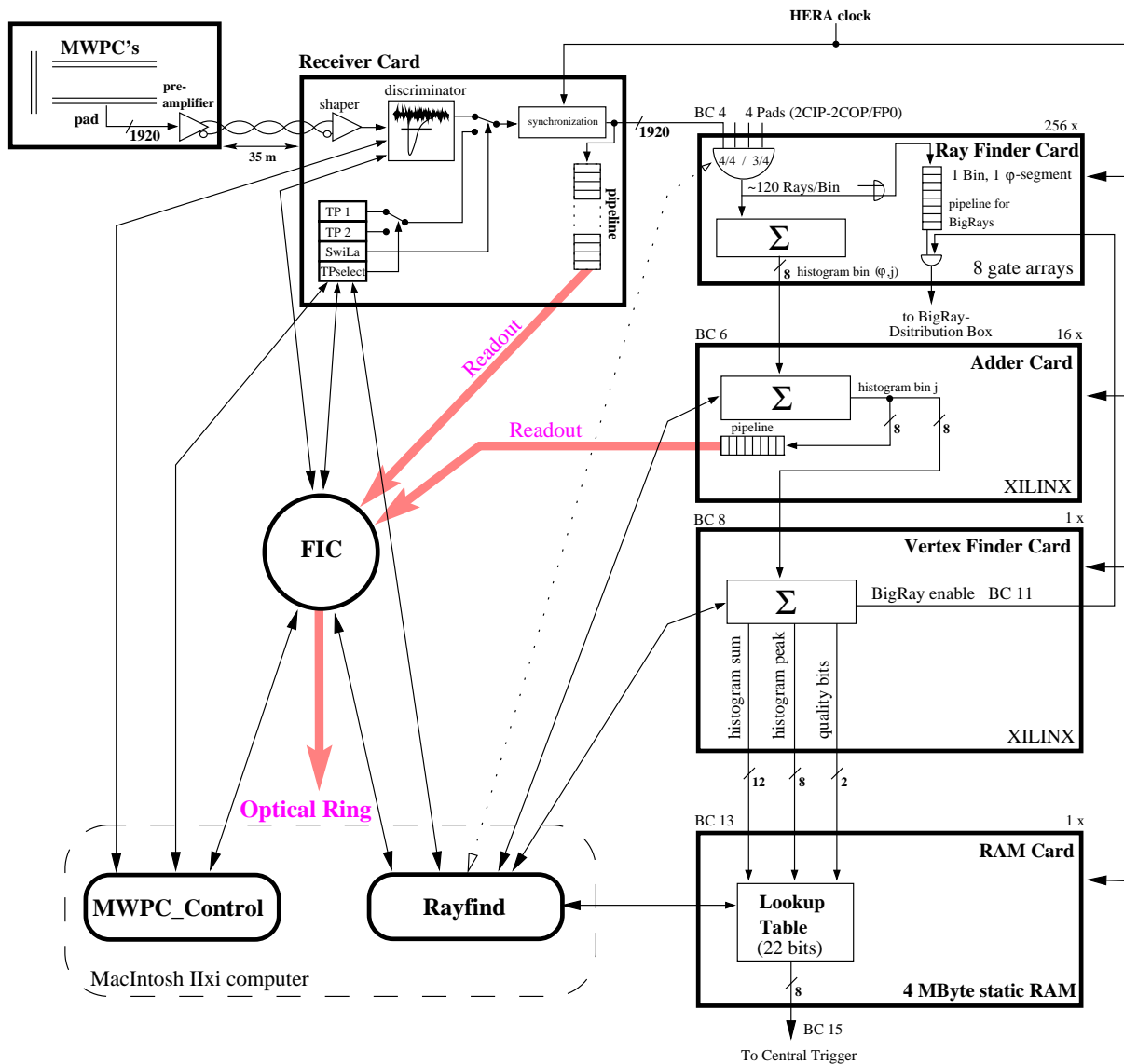
Figure 4.4: Implementation of the *z*–Vertex–trigger. The signals from 1920 MWPC pads are checked, whether they contain rays. All rays belonging to the same φ–segment and histogram bin are summed on the ray finder cards. After a summation over φ on the adder cards, the resulting histogram is analyzed on the vertex finder card. The final trigger bits are available after prominent values of the histogram were sent to a lookup table on the RAM card. There is no direct connection from the program RAYFIND to the ray finder cards, these have to be initialized through the data lines via the receiver cards.

main H1 data base. This way, with every runstop, the most up to date hardware settings are available offline.

4.2   Offline implementation of the z–Vertex trigger

In order to calculate the z–Vertex trigger response out of pad signals offline, several modules are needed, which follow closely the hardware realization described above.

At H1, all software is written in FORTRAN77 [57] and in order to gain more flexibility, BOS [58] a dynamic memory management system for FORTRAN is used. All data volumes are stored in BOS banks, which allows for a modular structure of the whole H1 software environment. The signals of CIP and COP are stored in one common BOS bank (further only *bank*) CRME and the signals of FPC in a own bank FRME. The structure of these banks is seen in table 4.1.

TABLE **CRME**		B16			Central Response MWPC Event Bank
COL	ATT–name	FMT	Min	Max	Comments
1	NCHAN	I	0	1535	*channel number of active pad*

TABLE **FRME**		B16			Forward Response MWPC Event Bank
COL	ATT–name	FMT	Min	Max	Comments
1	NCHAN	I	0	1151	*channel number of active pad*

Table 4.1: Contents of *CRME* and *FRME* banks.

Two large tables CTRC and CTRF define for each central and for each forward ray respectively the pad combinations, the bin of the z–Vertex histogram and the range of big rays being enabled. There are 1198 central and 948 forward rays defined. These two tables are defined for one φ–segment only, as all rays are identical for each φ–segment. Any deviation from that symmetry, as arises if one wants to defeat malfunctioning of chamber segments, has to be corrected using special update tables which are stored in the CTR1 bank. Table 4.2 shows the contents of CTRC and CTRF. Table 4.3 shows the contents of the CTR1 bank, which is usually empty, as only updates to the ray tables enter this bank. This bank allows to set a *preset* bit for each chamber pad individually, which enables the *three out of four* option. More precisely, a ray, defined through four signals $s_1, \ldots, s_4$ is active when following boolean expression evaluates to .TRUE.:

$$s_1 \cdot s_2 \cdot s_3 \cdot s_4 + p_1 \cdot s_2 \cdot s_3 \cdot s_4 + s_1 \cdot p_2 \cdot s_3 \cdot s_4 + s_1 \cdot s_2 \cdot p_3 \cdot s_4 + s_1 \cdot s_2 \cdot s_3 \cdot p_4 \qquad (4.1)$$

The preset bits p_i can be set for each pad in each φ–segment individually. These banks (CRME,FRME,CTRC,CTRF and CTR1) are sufficient to calculate the z–Vertex histogram and the big rays, this is done in CMRAYS a routine from within the H1 simulation package. It uses a clever algorithm, which needs only one loop over all active pads instead the pedestrian approach which would need a four times interlaced loop to

TABLE **CTRC**		I			ray list for CIP–COP pad combinations
COL	ATT–name	FMT	Min	Max	Comments
1	IZ0	I	0	59	*pad z position of inner layer of* CIP
2	IZ1	I	0	59	*pad z position of outer layer of* CIP
3	IZ2	I	0	17	*pad z position of inner layer of* COP
4	IZ3	I	0	17	*pad z position of outer layer of* COP
5	IZBIN	I	0	15	*associated bin of z–Vertex histogram*
6	IBTMIN	I	1	14	*lower limit of associated big ray range*
7	IBTMAX	I	1	14	*upper limit of associated big ray range*

TABLE **CTRF**		I			ray list for CIP–FPC pad combinations
COL	ATT–name	FMT	Min	Max	Comments
1	IZ0	I	0	59	*pad z position of inner layer of* CIP
2	IZ1	I	0	59	*pad z position outer layer of* CIP
3	IR2	I	0	19	*pad r position of first layer of* FPC
4	IR3	I	0	19	*pad r position of second layer of* FPC
5	IZBIN	I	0	15	*associated bin of z–Vertex histogram*
6	IBTMIN	I	1	7	*lower limit of associated big ray range*
7	IBTMAX	I	1	7	*upper limit of associated big ray range*

Table 4.2: Contents of CTRC and CTRF banks.

check all coincidences. Once the rays are calculated, they get stored in the CTRY bank (see table 4.4). The calculation of the z–Vertex histogram and the big rays is done in CMVHIS and CMBRAY respectively, two simple lookup routines. The histogram is stored in the CTVE bank and the big rays in a BRDB bank, their structure is seen in table 4.5 and 4.6. The CTVE bank allows to keep more than one histogram in order to cope with the pipelined readout procedure, which allows to read not only the actual event from within the pipeline but also z–Vertex histograms in the previous and succeeding slices of the pipeline can be read out and have to be stored subsequently. As big rays are not only built by the z–Vertex trigger but also by the forward ray trigger [59] the BRDB bank has a structure which allows to store big rays from either source. A flow chart illustrating the data flow during the calculation of the z–Vertex trigger is seen in fig 4.5.

BANK **CTR1**	I	modified pads for ray list
bits	**0 ... 10**	*identify the Pad number, (0 to 2047)*
bits	**11,12**	*identifies the region in which the pad is found*
		bit 11 = 0 and bit 12 = 0: central
		bit 11 = 1 and bit 12 = 0: forward
		bit 11 = 0 and bit 12 = 1: backward (not implemented)
bit	**13**	*set to 0 if the pad is connected to the chamber*
		set to 1 if the pad is set to a test pattern value
bit	**14**	*set to 0 if the test pattern value is always off*
		set to 1 if the test pattern value is always on
bit	**15**	*set to 0 if preset is disabled*
		set to 1 if preset is enabled
bits	**16,17**	*only used for CIP and innermost FPC pads (these have a 8–fold segmentation in φ only):*
		indicate to which half of the pad the test pattern value is active
		bit 16 = 1: first half seen clockwise
		bit 17 = 1: second half seen clockwise
bits	**18,19**	*only used for CIP and innermost FPC pads:*
		indicate to which half of the pad the preset bit set
		bit 18 = 1: first half seen clockwise
		bit 19 = 1: second half seen clockwise

Table 4.3: Contents of the CTR1 bank.

BANK **CTRY**	I				list of active rays
COL	ATT–name	FMT	Min	Max	Comments
1	IRAY	I	0	159999	*the first two digits represent the φ segment $(0 \leq \varphi \leq 15)$ in which the ray was found and the last four digits represent the continuous ray index as found by concatenating CTRC and CTRF list of rays.*

Table 4.4: Contents of the CTRY bank.

4.3 Definition of the z–Vertex trigger elements

Once the z–Vertex histogram is filled, only the trigger bits need to be calculated, which are determined from the 16 bins of the histogram through a set of logical functions. These

TABLE **CTVE**		B16			central trigger vertex histograms
COL	ATT–name	FMT	Min	Max	Comments
1	BCnumber	I	0	32	*bunch crossing number, indicating the time slice on the pipeline to which this histogram belongs.*
2	ZVBIN0	I			*content of bin_0 and bin_1 ($256 \cdot bin_1 + bin_0$)*
3	ZVBIN1	I			*dito for bin_2 and bin_3*
4	ZVBIN2	I			*dito for bin_4 and bin_5*
5	ZVBIN3	I			*dito for bin_6 and bin_7*
6	ZVBIN4	I			*dito for bin_8 and bin_9*
7	ZVBIN5	I			*dito for bin_{10} and bin_{11}*
8	ZVBIN6	I			*dito for bin_{12} and bin_{13}*
9	ZVBIN7	I			*dito for bin_{14} and bin_{15}*

Table 4.5: Contents of the CTVE bank.

TABLE **BRDB**		B16			contents of big ray distribution box
COL	ATT–name	FMT	Min	Max	Comments
1	BCnumber	I	0	32	*bunch crossing number, indicating the time slice on the pipeline to which these big rays belong.*
2	Data1	I			*central big rays (bit packed) of φ–segment 0*
3	Data1	I			*forward big rays (bit packed) of φ–segment 0*
⋮	⋮	⋮			
32	Data31	I			*central big rays (bit packed) of φ–segment 15*
33	Data32	I			*forward big rays (bit packed) of φ–segment 15*

Table 4.6: Contents of the BRDB bank.

simulate the *ram card* described in section 4.1. Input to these functions are the number of entries in the z–Vertex histogram, the highest number of entries found in an individual bin (the peak) and two quality bits derived from the topology of the histogram. Quality bit 1 is set if all entries of the z–Vertex histogram are found within four neighboring bins and none outside and quality bit 2 is set if no highest entry is found in the two outermost bins on either side of the histogram. The eight trigger elements are then defined as follows[†]:

[†]The programming of the ram card is flexible enough, that at any time a complete new set of trigger bits might be invented. The definition of the trigger bits shown here is the one which was used in the first three years running of H1
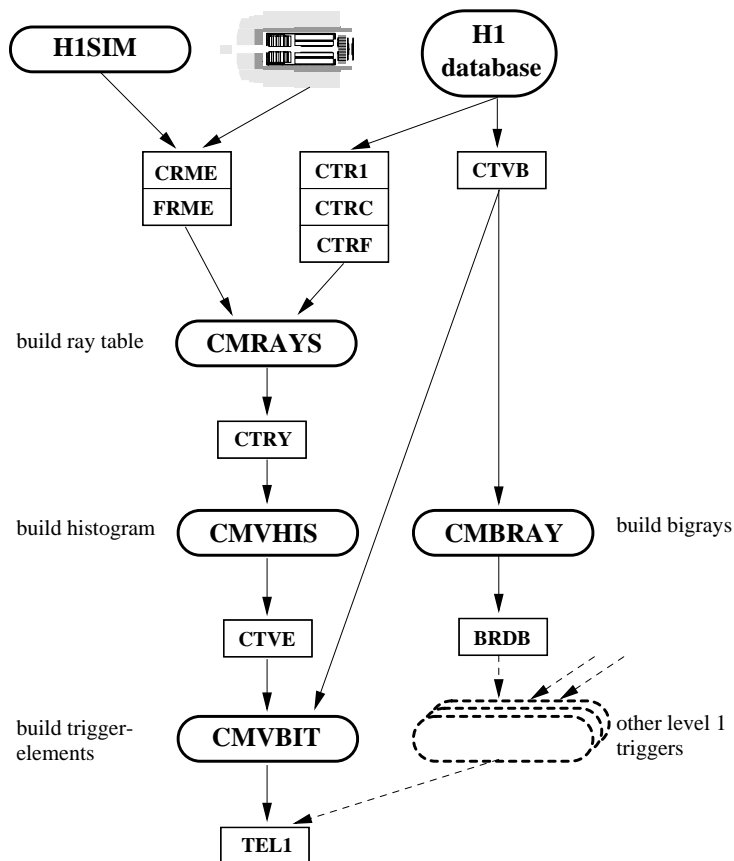
Figure 4.5: Flow chart of z–Vertex trigger simulation. The chamber response is stored in the CRME and CRMF banks, taken either from H1SIM or directly from the experiment and enter the relevant routines for a calculation of the expected response of the z–Vertex trigger. All setup data are derived from the global H1 database.

$\mathbf{T_0}$ this bit is set whenever a non–empty histogram is found.

$\mathbf{S_0, S_1, S_2}$ are used to code numbers from 0 to 7 which indicate the sum of the z–Vertex histogram: $0,1,2$–$3,4$–$5,6$–$7,8$–$10,11$–max,$>max$.

Small   is set whenever the histogram peak is smaller than *peak* and the sum over all other bins is smaller than *rest*. As this condition is fulfilled naturally for empty histograms, a special veto can be set which prevents triggering on empty histograms. A second veto bit prevents triggering when a peak is found near the edge of the histogram.

Cluster   is set whenever the histogram content is within four neighboring bins. Again, two veto bits can be set to prevent triggers on empty histograms and peaks

found near the edge.

$\boldsymbol{\sigma_1}$ is set if one of four predefined boolean functions (see equation (4.7)) evaluates
to .TRUE.

$\boldsymbol{\sigma_2}$ dito.

The values of *max*, *peak*, *rest* and the veto options are free parameters which have to be
defined before the loading of the trigger. The quality bits can be expressed more precisely
using following expressions:

$$Q_1 = \begin{cases} 1 & \text{if} \quad \exists\, j \in (0 \ldots 12) \quad | \quad \sum_{i=j}^{j+3} \text{bin}(i) = \sum_{i=0}^{15} \text{bin}(i) \\ 0 & \text{otherwise} \end{cases} \tag{4.2}$$

for the cluster–bit Q_1 and

$$Q_2 = \begin{cases} 1 & \text{if} \quad \exists\, j \in (0,1,14,15) \quad | \quad \text{bin}(j) = \max_{i \in (0 \ldots 15)} \text{bin}(i) \\ 0 & \text{otherwise} \end{cases} \tag{4.3}$$

for the edge–bit Q_2.

It is useful to define *peak*, *sum* and *background* as general properties of the z–Vertex
histogram:

$$p = \text{peak} \qquad\quad = \max_{i \in (0 \ldots 15)} \text{bin}(i) \tag{4.4}$$

$$s = \text{sum} \qquad\quad = \sum_{i=0}^{15} \text{bin}(i) \tag{4.5}$$

$$b = \text{background} \; = \frac{\text{sum} - \text{peak}}{15} \tag{4.6}$$

With help of these parameters, it is possible to describe the ram card in its full function-
ality: Any imaginable boolean function out of p, s, Q_1 and Q_2 plus additional parameters
which are independent of the actual topology of the histogram can be implemented. Fol-
lowing functions σ_1 and σ_2 have been implemented:

$$\sigma_{1;2}(p, s, Q_1, Q_2, \mathbf{par}, \mathbf{veto}) = \begin{cases} \mathbf{1:} \; \left(\quad \dfrac{p - b}{\sqrt{p}} \quad > \mathbf{par} \right) \cdot \overline{(Q_2 \cdot \mathbf{veto})} \\[2mm] \mathbf{2:} \; \left(\quad\quad p \quad\quad > \mathbf{par} \right) \cdot \overline{(Q_2 \cdot \mathbf{veto})} \\[2mm] \mathbf{3:} \; \left(\quad\quad s \quad\quad > \mathbf{par} \right) \cdot \overline{(Q_2 \cdot \mathbf{veto})} \\[2mm] \mathbf{4:} \; \left(\dfrac{\sqrt{p} - 2.5}{b + \frac{1}{15}} > \mathbf{par} \right) \cdot \overline{(Q_2 \cdot \mathbf{veto})} \end{cases} \tag{4.7}$$

For both σ_1 and σ_2, a set of four different functions is predefined from which one has to be selected as well as the parameter *par* and the *veto*–bit have to be selected at the time when the trigger hardware is going to be initialized. The factor $\overline{(Q_2 \cdot \text{veto})}$ gives the possibility to prevent triggering when a peak is found near the edge of the histogram, which means far away of the nominal interaction point. Function 1 asks the peak to be significantly above the averaged background of the z–Vertex histogram, assuming a statistical error of the value of the peak–bin of $\sqrt{p}$. Functions 2 and 3 ask the peak, the integral sum respectively, to be above a given threshold. Function 4 is derived ad hoc from a Monte–Carlo analysis of $c\bar{c}$–events. A fifth function is going to be implemented based on a neural network study of J/ψ and D^* candidates. The final trained network is a function of p,s,Q_1 and Q_2 and can be realized on the ram card. These setup values are stored in the CTVB bank which has the data structure shown in table 4.7.

BANK **CTVB**		I			settings of the z–Vertex trigger
COL	ATT–name	FMT	Min	Max	Comments
1	SUM_MAX	I	0	4080	max *used for* S_0, S_1, S_2 *bits*
2	PEAK_SML	I	0	255	peak *used for* small *bit*
3	REST_SML	I	0	3825	rest *used for* small *bit*
4	ACC_ZERO	I	0	1	*accept 0 entries for* small *bit*
5	EXCL_BIN	I	0	1	veto *if peak at edge for* small *bit*
6	CLU_ZERO	I	0	1	*accept 0 entries for* cluster *bit*
7	EXCL_CLS	I	0	1	veto *if peak at edge for* cluster *bit*
8	SIGFUN_1	I	1	4	*function used for* σ_1 *bit*
9	THRES_1	I	0	$+\infty$	*par·100 for* σ_1 *bit*
10	EXCLSIG1	I	0	1	veto *if peak at edge for* σ_1 *bit*
11	SIGFUN_2	I	1	4	*function used for* σ_2 *bit*
12	THRES_2	I	0	$+\infty$	*par·100 for* σ_2 *bit*
13	EXCLSIG2	I	0	1	veto *if peak at edge for* σ_2 *bit*
14	BIGRAYVAL	I	0	3	*criteria to select big ray enabling rays:*
					0: each ray enables big rays
					1: rays pointing to a peak of the
					* z–Vertex histogram enable big rays*
					2: rays pointing to a peak or to its
					* neighbor enable big rays*
					3: rays pointing to a peak or to its first
					* or second neighbor enable big rays*

Table 4.7: Contents of the CTVB bank.

Once the trigger bits of the z–Vertex trigger are known, they are stored together with all trigger bits from all other triggers at H1 in the TEL1 trigger element level 1 bank (check ref. [60] how to access this bank).

4.4   Reliability of the z–Vertex trigger

Before any data can be analyzed based on z–Vertex triggered events, the reliability of the z–Vertex hardware has to be known. With help of the offline tools described in the previous sections, it is possible to check whether the input into the trigger, the MWPC response event banks, corresponds with its output, the z–Vertex histogram and the trigger bits, for each event individually. The result of such a cross check is rather sensitive to the knowledge of all setup parameters and care has to be taken to keep these values up to date for any given run period. Taking track of these parameters by human interference is hardly possible as the setup is not determined by one component alone and there are furthermore different people working on different components at once. All setup parameters for the whole H1 experiment for any given time period are stored in one common place, the *H1 database*. Each H1 run has its own set of setup parameters. Meanwhile more than 100'000 runs have been taken at the H1 supervisor console. Even if the setup parameters of the z–Vertex trigger are not changing with each run and a rather stable operation with no changes in parameters are derived, a complete and automatic scheme has been implemented to keep track of all relevant parameters and to compute a few numbers per run indicating the proper or improper functioning of the z–Vertex trigger. This scheme is sketched in fig 4.6.

As the CTR1 setup bank does not depend on the settings of the z–Vertex trigger alone but also on the settings of the receiver cards (see table 4.3) the setup parameters known to the program MWPC_control have to be merged with the setup parameters known to the program RAYFIND. Both programs run on a MacIntosh computer and do not share any data volumes, except that both write into the same VME memory connected to different pieces of hardware all sharing the same VMEbus. The memory of the FIC front–end processor is therefore an ideal place to store setup values from both, MWPC_control and RAYFIND. Whenever a hardware component is reinitialized, the initializing program writes also its relevant setup data directly in BOS data structures into the FIC memory.

ZRMR is the BOS bank written by MWPC_control containing for each channel on each receiver card the threshold values, the switch–latch settings indicating if the channel is connected to the chamber or to some test pattern value, the values of the test patterns and some technical data not relevant for offline calculations such as settings of delay lines.

RAYFIND writes a rather technical ZVTX bank (see table 4.8) containing information
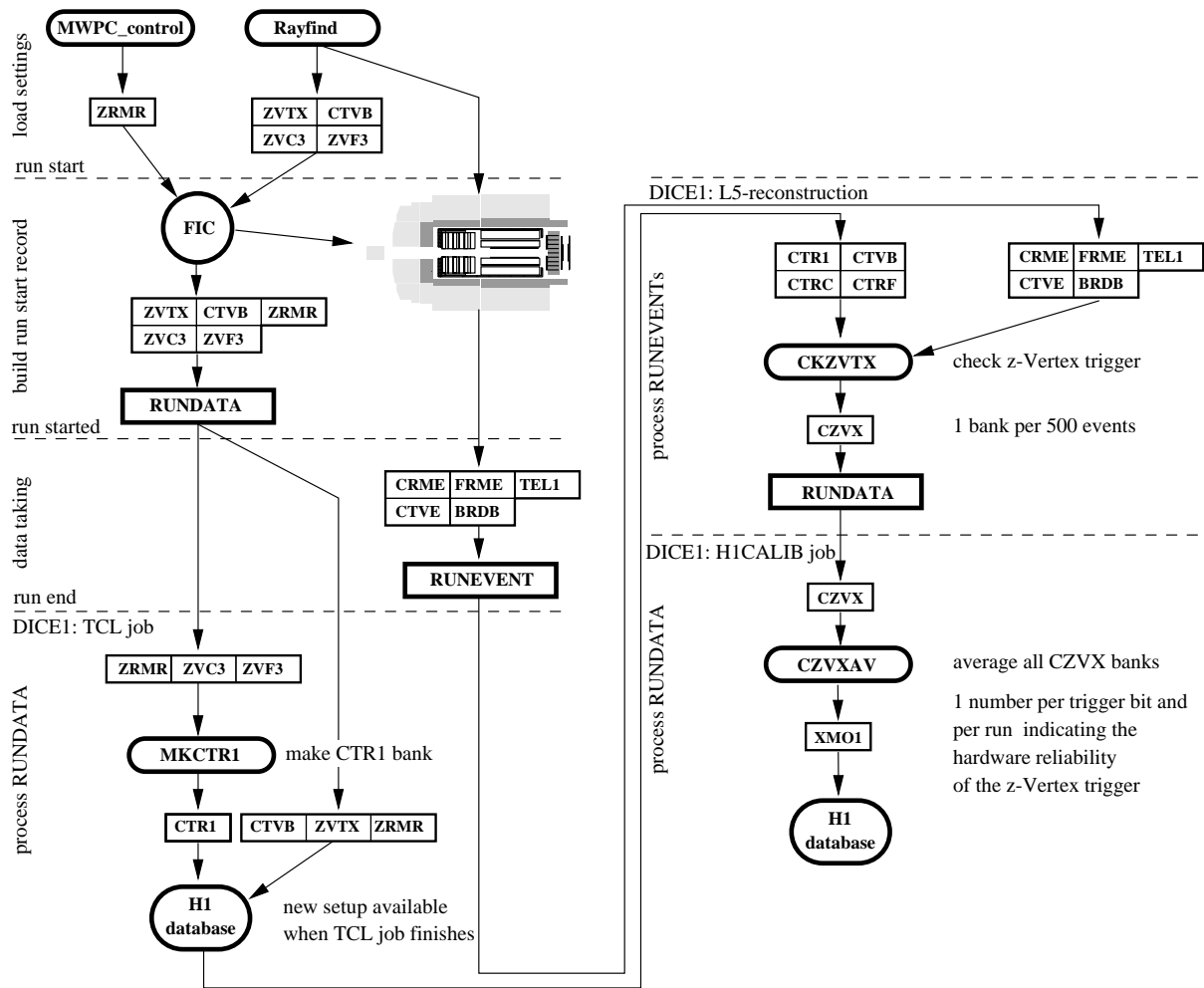
Figure 4.6: Data flow of setup parameters of the z–Vertex trigger. At time when the hardware gets initialized, a copy of the relevant parameters are written into the FIC's memory. At runstart, these settings follow the H1 data stream and enter the runstart record. Further analyzing of the event data results in one number (0–100%) per run and trigger bit, indicating the hardware reliability of the z–Vertex trigger.

about date and time of the last loading of the trigger and some internal settings. The offline relevant data are sent in three banks, namely CTVB, described above (see table 4.7) and ZVC3 and ZVF3 both containing the preset bits for the three out of four option for central and forward rays respectively (see table 4.9).

TABLE **ZVTX**		B16			z–vertex initialization bank
COL	ATT–name	FMT	Min	Max	Comments
1	YEAR	I	1904	2040	*date and time of initializing*

Table 4.8: (continued)

TABLE **ZVTX**		B16			z–vertex initialization bank
COL	ATT–name	FMT	Min	Max	Comments
2	MONTH	I	1	12	*the z–Vertex trigger hardware*
3	DAY	I	1	31	
4	HOUR	I	0	23	
5	MIN	I	0	59	
6	SEC	I	0	59	
7	DOWEEK	I	1	7	*day of week; 1=Sunday*
8	CONFIG	I	0	65535	*version identifier*
9	cYEAR	I	1904	2040	*date and time of last modifying*
10	cMONTH	I	1	12	*the configuration of the trigger*
11	cDAY	I	1	31	
12	cHOUR	I	0	23	
13	cMIN	I	0	59	
14	cSEC	I	0	59	
15	cDOWEEK	I	1	7	
16	CIP034	I	0	65535	CIP *0: one bit per φ–sector if the* preset *bit is set for at least one* *half–pad*
17	CIP134	I	0	65535	CIP *1: dito*
18	COP034	I	0	65535	COP *0: dito*
19	COP134	I	0	65535	COP *1: dito*
20	FP0034	I	0	65535	FP0 *0: dito*
21	FP1034	I	0	65535	FP1 *0: dito*
22	INCLK	I	0	255	*InClock delay*
23	PCLK	I	0	255	*PClock delay*
24	ACLK	I	0	255	*AClock delay*
25	SLOW2FW	I	0	255	*Slow 2 FW delay*
26	SLOW2CB	I	0	255	*Slow 2 C/B delay*
27	PENAF	I	0	255	*Pipe enable FW delay*
28	PEANCB	I	0	255	*Pipe enable C/B delay*
29	HCLKFW	I	0	255	*Fanout Clock FW delay*
30	HCLKCB	I	0	255	*Fanout Clock C/B delay*
31	ACC	I	0	255	*Adder CC delay*
32	DELC00	I	0	255	*Delay Clock 0*
33	DELC01	I	0	255	*Delay Clock 1*
34	DELC02	I	0	255	*Delay Clock 2*

Table 4.8: (continued)

TABLE **ZVTX**		B16			z–vertex initialization bank
COL	ATT–name	FMT	Min	Max	Comments
35	DELC03	I	0	255	*Delay Clock 3*
36	DELC04	I	0	255	*Delay Clock 4*
37	DELC05	I	0	255	*Delay Clock 5*
38	DELC06	I	0	255	*Delay Clock 6*
39	DELC07	I	0	255	*Delay Clock 7*
40	DELC08	I	0	255	*Delay Clock 8*
41	DELC09	I	0	255	*Delay Clock 9*
42	DELC10	I	0	255	*Delay Clock 10*
43	DELC11	I	0	255	*Delay Clock 11*
44	DELC12	I	0	255	*Delay Clock 12*
45	DELC13	I	0	255	*Delay Clock 13*
46	DELC14	I	0	255	*Delay Clock 14*
47	DELC15	I	0	255	*Delay Clock 15*
48	ADDPIP	I	0	255	*Adder pipe length*
49	VTXPIP	I	0	255	*Vertex pipe length*
50	RAMPIP	I	0	255	*RAM pipe length*
51	TRGPIP	I	0	255	*Trigger out pipe length*
52	DRV1P	I	0	255	*Driver 1 pipe length*
53	DRV2P	I	0	255	*Driver 2 pipe length*
54	GA18	I	0	255	*Out pipe GA 1 . . . 8*
55	GA910	I	0	255	*Out pipe GA 9 . . . 10*

Table 4.8: Contents of the ZVTX bank.

As soon as a run gets started at the H1 supervisor console, a *runstart record* is created as first action. The FIC front end processor dumps the initialization part of its memory into the main data stream. All relevant setup data from all other subdetectors are then collected and merged into one event record. In addition, all few hundred events during normal H1 data taking, *RUNDATA* records can be written containing new setup parameters. The MWPC system does not take use of this possibility, only the very first *RUNDATA* record, the *runstart* record contains its setup parameters. As soon as a run stops, a special offline job, the *TCL job*, starts at the main offline reconstruction computer DICE1, an SGI challenge machine. This job analyzes *RUNDATA* records only and updates the main H1–database with new setup values. At this stage, MKCTR1 a special routine compiles the CTR1 bank out of ZRMR, ZVC3 and ZVF3. The CTR1, ZVTX and ZRMR

BANK **ZVC3**	I	preset bits for CIP and COP pads
bits **0 ... 10**		*identify the Pad number, (0 to 1535)*
bits **11,12**		*only used for CIP pads (these have a 8–fold segmentation*
		in φ only):
		indicate to which half of the pad the preset bit is active
		bit 11 = 1: first half seen clockwise
		bit 12 = 1: second half seen clockwise

BANK **ZVF3**	I	preset bits for FPC pads
bits **0 ... 8**		*identify the Pad number, (0 to 383)*
bits **9,10**		*only used for innermost pads (these have a 8–fold*
		segmentation in φ only):
		indicate to which half of the pad the preset bit is active
		bit 9 = 1: first half seen clockwise
		bit 10 = 1: second half seen clockwise

Table 4.9: Contents of the ZVC3 and ZVF3 banks.

banks get now updated on the database, either by prolonging the run range in case of identical setup to the previous runs, by writing a delta bank containing only changes of the setup parameters with respect to the previous run or by completely writing the full bank contents.

On level 5, the offline reconstruction on the DICE1 computer, each event gets analyzed individually. As the setup of the z–Vertex trigger is now known completely to the current job, a verification of the real output of the z–Vertex trigger with its expected output calculated out of the trigger chamber response is possible. For each event it is checked, whether the z–Vertex histogram is bin by bin identical to the expected one, whether the z–Vertex–T_0 is as expected and whether all big rays are identical to the expected ones. At the same time, a first rough measurement of the trigger chamber efficiencies is done. Following the online monitoring scheme of V. Blobel [61], the results of 500 events are collected in one bank and written into the *RUNDATA* stream. The CZVX bank contains the results from this hardware check (see table 4.10). In analogy to the *TCL job*, the *H1CALIB job* runs over all *RUNDATA* records after level 5 has finished a run. Here, the routine CZVXAV averages all CZVX banks and derives for the z–Vertex histogram, the z–Vertex-T_0 and for the big rays one number each, indicating the results of the hardware quality check. These numbers get stored in the database in XMO1 a special monitoring bank (see ref. [61] for a description of this bank).

With all setup parameters accessible in the master database on a run by run basis, it is

TABLE **CZVX**		I			z–Vertex check results
COL	ATT–name	FMT	Min	Max	Comments
1	ZBIN	F	0.	1.	*1.0: if* MWPC *pads and z–Vertex histogram are consistent*
					0.0: otherwise
2	ZT0	F	0.	1.	*1.0: if* MWPC *pads and z–Vertex–T_0 are consistent*
					0.0: otherwise
3	ZVBR	F	0.	1.	*1.0: if* MWPC *pads and big rays from z–Vertex trigger are consistent*
					0.0: otherwise
4	EVENT	F	0.	$+\infty$	*event number of current event*

Table 4.10: Contents of CZVX bank.

```
*************************************************
*                                               *
* zVtx downloaded:       Son 30-10-1994  16:31  *
* zVtxConfig.10 created: Thu 04-08-1994  19:54  *
*                                               *
* 3 out of 4 in following phi-sectors           *
* -----------------------------------           *
*                                               *
* COP_0: 14, 15                                 *
* COP_1: 11, 12, 13                             *
*                                               *
* Setup of RAM                                  *
* ------------                                  *
*                                               *
* SUM_MAX                100                    *
*                                               *
* SMALL Peak .LE.          5                    *
* SMALL Rest .LE.          3                    *
* SMALL reject 0 entries                        *
* SMALL accept peak in edge bins                *
*                                               *
* CLUSTER reject 0 entries                      *
* CLUSTER exclude peak in edge bins             *
*                                               *
* Sig_1 function          1                     *
* Sig_1 threshold         1.50                  *
* Sig_1 exclude edge bins                       *
*                                               *
* Sig_2 function          1                     *
* Sig_2 threshold         1.50                  *
* Sig_2 exclude edge bins                       *
*                                               *
* BigRay Validation:      peak+-2               *
*                                               *
*************************************************
```

Figure 4.7: Setup of the z–Vertex trigger for a given run as provided by the ZVSTUP routine.

now easy to retrieve any information. The routine ZVSTUP as available in H1 UTIL, the H1 utility library pool, dumps a selection of setup parameters. Fig 4.7 shows an example. To check the z–Vertex trigger performance is now feasible by just looking at the database without the need of stageing of hundreds of individual data tapes first. Figure 4.8 shows the reliability of the z–Vertex trigger for the whole autumn 1994 data taking period.
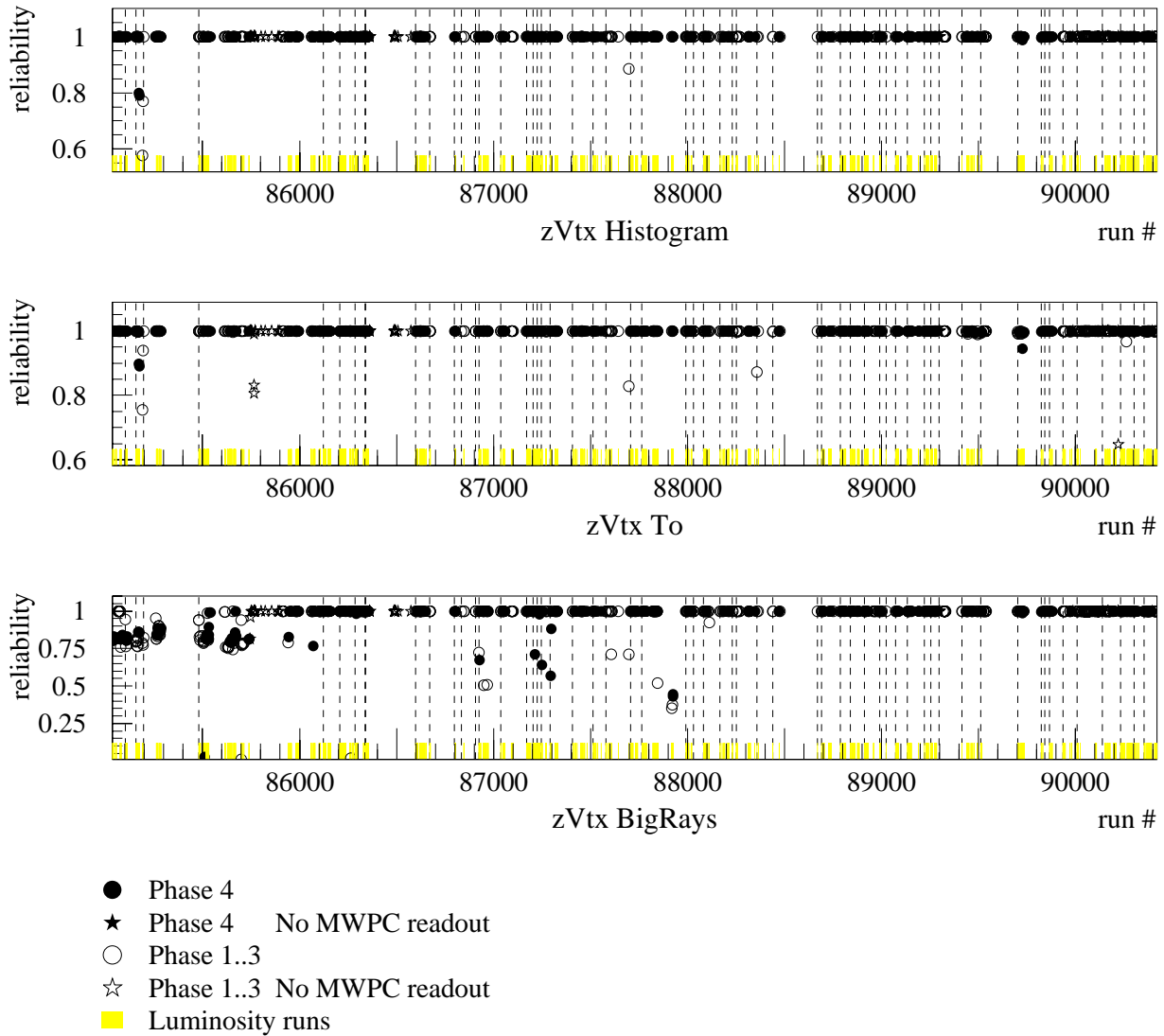

Figure 4.8: Reliability of the z–Vertex trigger. The run period from August 21st to November 1st 1994 is shown. Dotted lines represent the reinitialization of the trigger hardware. Except for a few runs the z–Vertex trigger worked very well. Runs with bad hardware reliability have to be excluded from the analysis. The big ray distribution box was just being installed, therefore, the measured reliability of big rays for the very first runs was not optimal.

4.5   The geometrical acceptance of the z–Vertex trigger

The trajectory of a charged particle moving in an homogeneous magnetic field is a helix which can be described using a set of five parameters. Taking the projection of a helix along the z–axis results in a circle. This circle is described by its signed curvature $\kappa = \pm r^{-1}$, the sign is determined by the charge of the particle, $\kappa < 0$ for positive charged particles (see fig 4.3), by the signed distance of closest approach to the z–axis d_{ca} and by the angle φ of the trajectory at the point of closest approach to the z–axis. Figure 4.9 explains the forthcoming sign conventions.
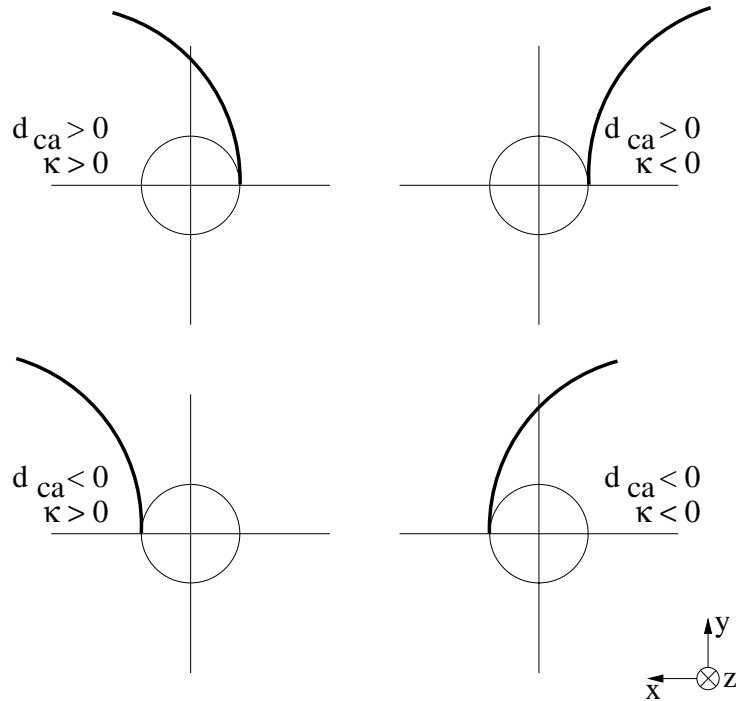

Figure 4.9: Sign conventions of track parameters ($\varphi = \pi/2$ for these tracks).

The probability for a particle track to enable a central ray of the z–Vertex trigger is a function ε' of $\varepsilon'(\kappa, d_{\mathrm{ca}}, \varphi)$. For the determination of the geometrical acceptance the inefficiencies of the proportional chambers are neglected and the probability function ε' takes only the two possible values 0 and 1. Either a given track of $(\kappa, d_{\mathrm{ca}}, \varphi)$ passes the proportional chamber within one φ–segment and enables a ray or it doesn't. Assuming an uniform distribution of tracks in φ, which is certainly fulfilled, allows for an integration

over φ:

$$\varepsilon(\kappa, d_{\mathrm{ca}}) = \frac{1}{2\pi} \int_0^{2\pi} \varepsilon'(\kappa, d_{\mathrm{ca}}, \varphi)\, d\varphi = 16 \cdot \frac{1}{2\pi} \int_{\varphi_1}^{\varphi_2} \varepsilon'(\kappa, d_{\mathrm{ca}}, \varphi)\, d\varphi$$

$$= 16 \cdot \frac{1}{2\pi} \cdot (\varphi_2 - \varphi_1) = \frac{16}{2\pi} \Delta\varphi \tag{4.8}$$

Where φ_1 and φ_2 are the minimal (maximal) possible angles φ within one φ–segment, such that $\varepsilon'(\kappa, d_{\mathrm{ca}}, \varphi) = 1$. The factor 16 normalizes to the 16 φ–segments.

$$\left(|\kappa^{-1}| + |d_{\mathrm{ca}}|\right)^2 + r_i^2$$
$$-2\left(|\kappa^{-1}| + |d_{\mathrm{ca}}|\right) r_i \cos(\xi_i) = \kappa^{-2}$$

$$\xi_i = \arccos\left\{\frac{r_i^2 + d_{\mathrm{ca}}^2 + 2|\kappa^{-1} d_{\mathrm{ca}}|}{2 r_i\left(|\kappa^{-1}| + |d_{\mathrm{ca}}|\right)}\right\}$$

$$\Delta\varphi = \alpha - (\xi_2 - \xi_1)$$

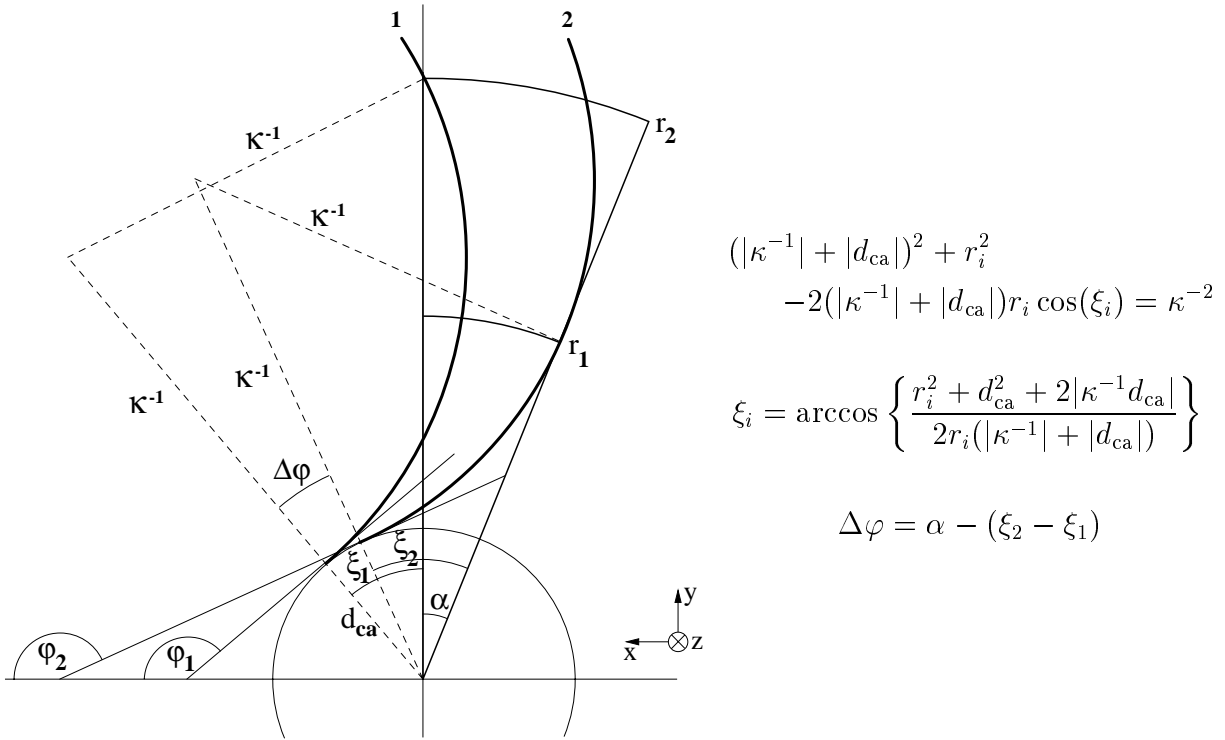**Figure 4.10:** Acceptance determination for single tracks.

Figure 4.10 shows the determination of $\Delta\varphi$ in the case of negative d_{ca} and positive κ. The angle α is the opening angle of one of the φ–segments and takes the value of $\alpha = \frac{2\pi}{16}$, r_1 and r_2 are the radii of the inner layer of CIP and the outer layer of COP. Similar geometrical exercises for the remaining cases for the signs of d_{ca} and κ lead to following universal expression:

$$\xi_i = \begin{cases} \text{undefined} & \text{if} \quad |d_{\mathrm{ca}}| > r_1 \text{ or } \mathrm{sign}(\kappa)(2\kappa^{-1} - d_{\mathrm{ca}}) < r_2 \\ \arccos\left[-\mathrm{sign}(d_{\mathrm{ca}})\dfrac{r_i^2 + d_{\mathrm{ca}}^2 - 2\kappa^{-1} d_{\mathrm{ca}}}{2 r_i(\kappa^{-1} - d_{\mathrm{ca}})}\right] & \text{otherwise} \end{cases}$$

$$\Delta\varphi = \begin{cases} 0 & \text{if} \quad \xi_1, \xi_2 \text{ undefined or } \alpha - |\xi_1 - \xi_2| < 0 \\ \alpha - |\xi_1 - \xi_2| & \text{otherwise} \end{cases}$$

$$\varepsilon(\kappa, d_{\text{ca}}) = \frac{1}{\alpha}\Delta\varphi \tag{4.9}$$

This formulation prevents unexpected results from tracks not reaching the CIP and COP layers and prevents double–counting of curling tracks, only the first intercept of a track with a chamber is used.
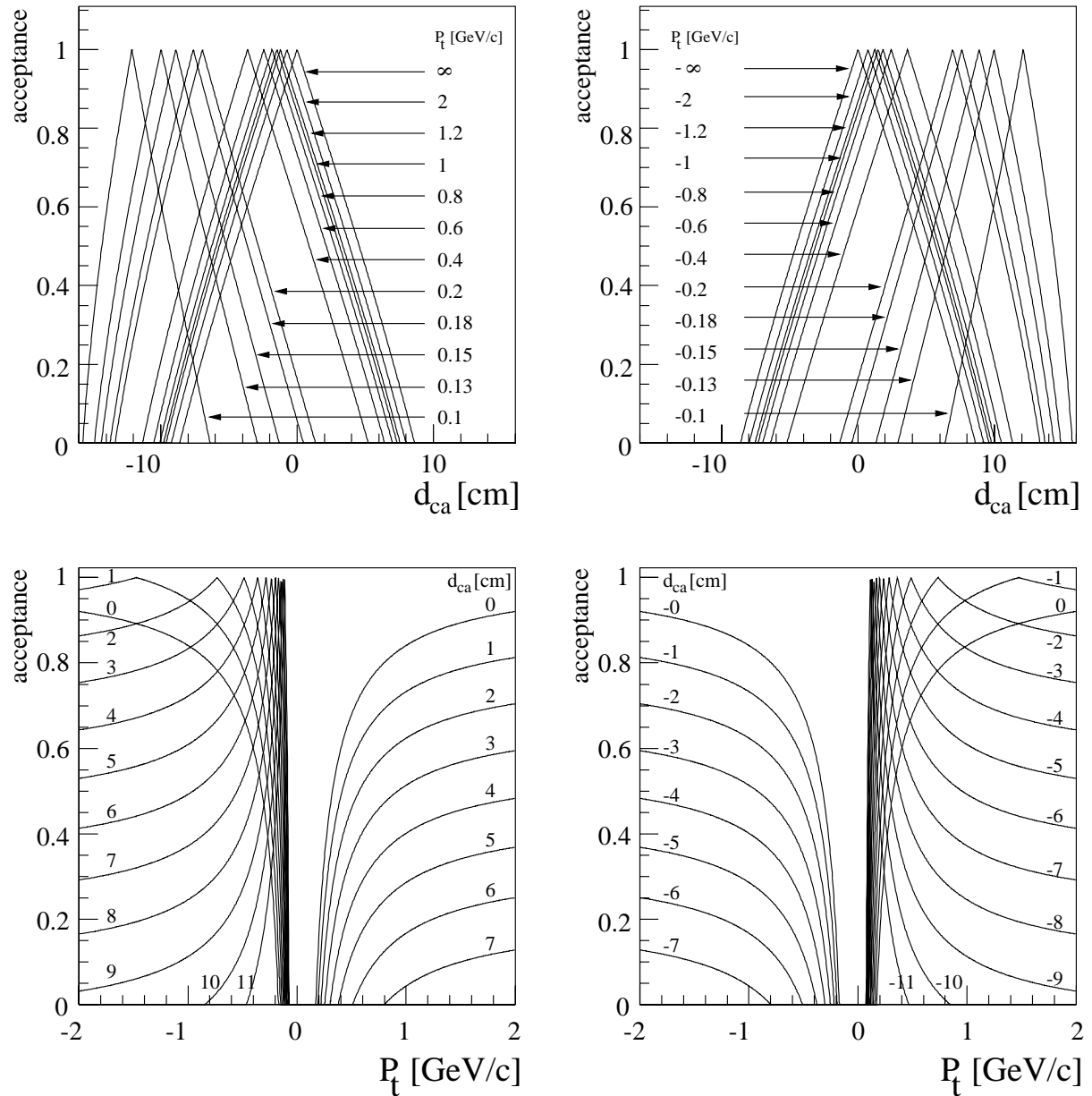

Figure 4.11: Acceptance of the z–Vertex trigger as function of transverse momenta and distance of closest approach of particle tracks Acceptances are only sensitive to the relative sign of d_{ca} and $p_{\perp}$.

The transverse momentum $p_\perp$ of a particle track is determined through the magnetic field B, the charge q and the inverse radius κ of the track as $p_\perp = \frac{qB}{\kappa}$. Using convenient units, where $p_\perp$ is measured in [GeV/c], B in [Tesla] and κ in [cm^{-1}] this relation reads as:

$$p_\perp = \pm \frac{0.29979 \cdot B}{\kappa \cdot 10^2} \tag{4.10}$$

with the sign being determined by the charge of the particle. (According the H1 sign conventions $p_\perp$ is negative for positive charged particles.)

Series of acceptance curves at fixed values of d_{ca} versus the transverse momentum $p_\perp$ and curves at fixed values of $p_\perp$ versus the distance of closest approach d_{ca} are shown in fig 4.11. Values for $r_{1,2}$ and B are 15.7 cm, 51.4 cm and 1.15 T, respectively (see tables 3.2 and 3.1).

The most important curve is the one for $d_{\text{ca}} = 0$ cm, as it represents particle tracks coming from genuine ep–collisions. The φ–segmentation of the proportional chamber is therefore equivalent to an effective $p_\perp$–cut of $\approx$ 170 Mev/c. An acceptance of 50% is reached at $\approx$ 330 Mev/c and 90% at $\approx$ 1.6 GeV/c. An acceptance 100% is only reached in the asymptotic limit of very large transverse momenta.

Large values of d_{ca} are suppressed only in the case of large transverse momenta, especially stiff cosmic tracks are limited into the range of $d_{\text{ca}} \approx -9 \ldots 9$ cm.

Tracks with large values of d_{ca} originate most probably from beam–gas and beam–wall events, they do not provide any physics interest but enlarge the trigger rate. Secondary particles from gamma–conversion at the beam–pipe or showers from collimator tips have a very high acceptance in the low $p_\perp$–range. At the L4 filter farm, over 70% of all z–Vertex–T$_0$ events with a tagged electron in the electron–tagger are rejected because the fast track analysis does not find any acceptable tracks (tracks with only few hits, large values of d_{ca} or pointing far outside the interaction region).

For each value of d_{ca} a corresponding value $p_\perp$ exists where the acceptance reaches 100%. The signed inverse radius κ determining the transverse momentum is then:

$$\kappa = -\frac{2d_{\text{ca}}}{r_1 r_2 - d_{\text{ca}}^2} \qquad \text{with} \quad |d_{\text{ca}}| < r_1 \tag{4.11}$$

Thus, large values of d_{ca} enable rays of the z–Vertex trigger at small transverse momenta.

Studying the effects of the preset bits (the three out of four logic, see section 4.2) on the acceptance is hardly possible on a purely analytical basis. A simple Monte–Carlo program has been used, which extrapolates randomly generated tracks to the layers of CIP and COP. Still, only the acceptance of the z–Vertex trigger is studied and therefore the pad determined by the intercept with the track is taken to be active (see fig 4.15). A CRME bank with at most 4 active pads per track is fed into the z–Vertex simulation package

(see fig 4.5). Enabling and disabling of preset bits in the CTR1 bank allows then for an extensive study of the behavior of the z–Vertex trigger acceptance. To reach a reasonable description of the shape of the acceptance curve, especially in the region of sharp kinks, demands a large amount of Monte–Carlo tracks being analyzed. More than 10 hours of CPU time on a SGI challenge computer was necessary to produce the plots shown in fig 4.12. These show the acceptance of the z–Vertex trigger with all preset bits set as for the real three out of four case. As can be seen in these plots, the acceptance turns into step–like functions and the rôle of d_{ca} is no longer evident. This effect is already seen, if the preset bits for the CIP pads alone are set, as it's determined by the 8–fold φ–segmentation of the two layers of CIP. Enabling the preset bits on CIP pads results in a over–proportional rise of the trigger rate, as lots of low energetic particles with all values of d_{ca} become accepted by the trigger.

Asymmetric acceptances, which enlarge the trigger rate for positive charged particles with respect to negative charged particles are obtained by setting the preset bits on the first half (seen clockwise) of each CIP pad.
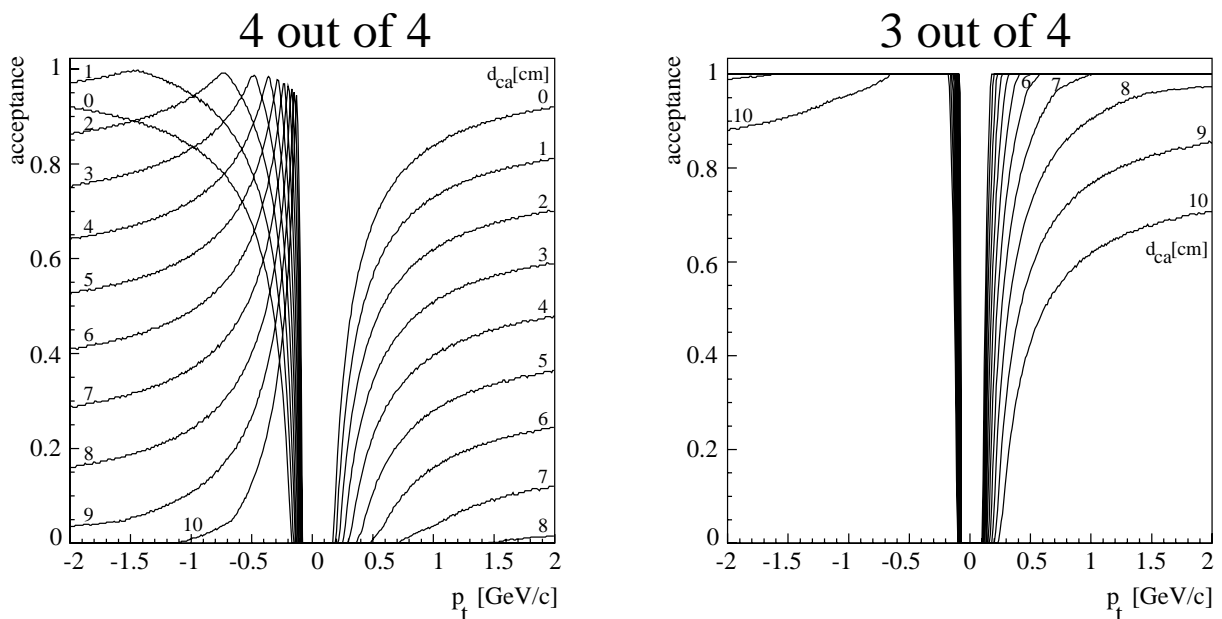

Figure 4.12: Effect of the three out of four option on the acceptance of the z–Vertex trigger. All acceptances are much more step–like. The suppression of large values of d_{ca} no longer holds. The Monte–Carlo result represents with less accuracy the analytic calculation in the four out of four case.

4.6 Efficiency determination of the z–Vertex trigger

The z–Vertex trigger is a topological trigger, even small changes in event properties let a previously triggered event go by unnoticed, e.g. an additional ray may turn a z–Vertex histogram fulfilling the *small* or *cluster* condition into a histogram no longer being accepted. The same is true for the $\sigma_{1,2}$ conditions. Table 4.11 shows possible combinations for values of peak and total sum of the z–Vertex histogram which enable the z–Vertex–σ_1 condition as it's used for H1 triggering.

$\dfrac{p - b}{\sqrt{p}} > 1.5$ with $b = \frac{\Sigma - p}{15}$							
p 3	4	5	6	7	8	9	10
Σ $3\ldots9$	$4\ldots18$	$5\ldots29$	$6\ldots40$	$7\ldots52$	$8\ldots64$	$9\ldots76$	$10\ldots88$

Table 4.11: z–Vertex trigger *quantum numbers* for σ_1. For a given value p of the peak, the histogram sum Σ has to be in a given range of values to fulfill the triggering criteria.

One exception is of course the z–Vertex–T_0 condition, here it is sufficient to calculate the efficiency for at least one ray of an event.

The probability for a given event to enable one of the z–Vertex trigger bits has to be calculated using the full event topology. This is possible for Monte–Carlo events if each trigger ray can be calculated sufficiently accurate. Such a procedure needs full knowledge of the behavior of the proportional chambers when a particle passes. For this reason the efficiency is determined for each run at the reconstruction step and stored in the H1–database. The same monitoring bank XMO1 as for the hardware reliability of the z–Vertex trigger has been used to store the data. Only one number per layer and run is stored as this efficiency is used to monitor changes of efficiencies only, such as different sets of thresholds, high voltage or ageing. The result of this monitoring task is seen in fig 4.13.

No run dependent changes are obvious from fig 4.13, it is therefore possible to describe the chamber efficiencies for the whole run period using one set of descriptive parameters only.

The physical behavior of proportional chambers is too complicated that it could be described using one parameter for its efficiency alone. A detailed study of each of its chamber pads together with a reasonable model, which describes the response of single pads while particle passes the chamber's layers, is necessary. Figure 4.14 shows a three dimensional hitmap of the MWPCs from a run period of several hundred runs taken in autumn 1994. The two layers of CIP show in coarse a rather smooth transition from little activity at
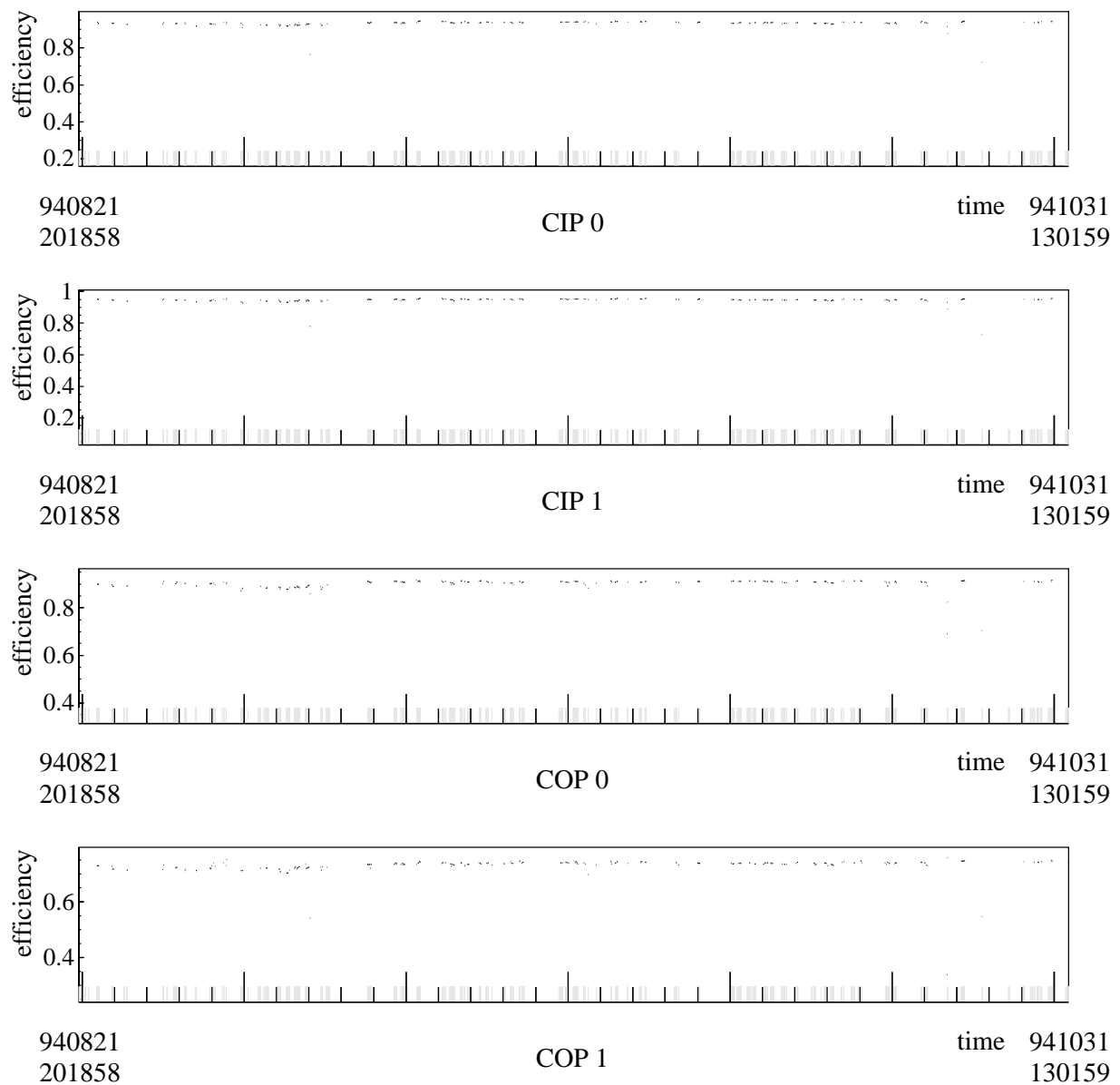
Figure 4.13: Efficiency of MWPC's. The period from August 21 20:18 to October 31 13:01 1994 is shown. All four chambers run stable except of very few exceptions where destructive beam conditions prevented a smooth operation. The typical efficiency is in the order of 90%, except for COP 1 where a broken wire kills 3/16 of the chamber.

the edges and much activity in the central region. Looking more carefully, lots of individual activities are recognized. Single dead channels exists, but are not visible in this perspective. COP 0, with only 18 channels along the z–axis, shows more morphology, as two of its sectors show extreme activity which is identified to be noise. One dead cable,

feeding the signals of 12 pads into the receiver cards was not operational and no single hit is visible in this region. COP 1 has one broken anode wire which prevents due to short circuits setting the high voltage of three out of sixteen sectors.
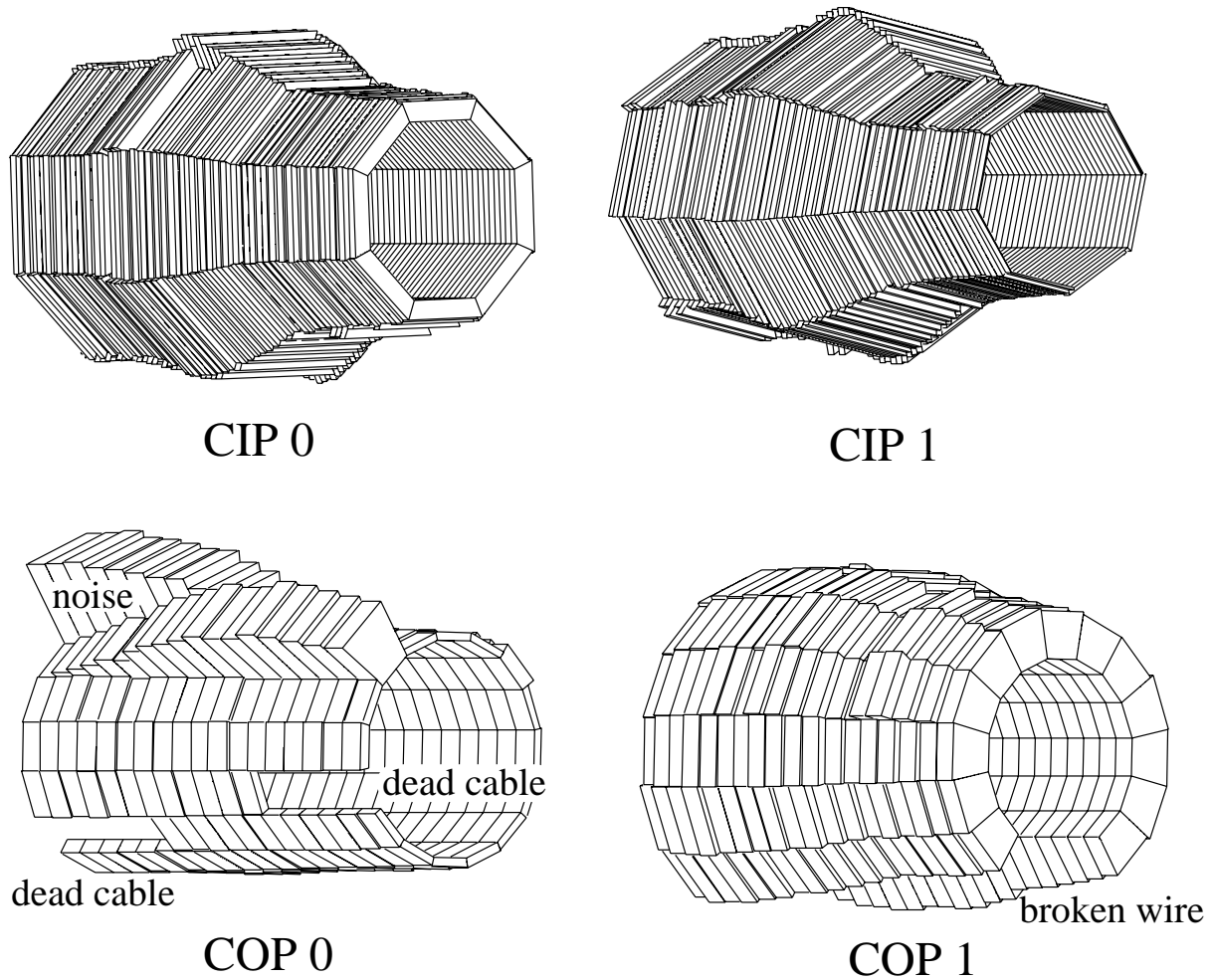

Figure 4.14: Hitmap of MWPC's. The integrated activity of each pad during a run period of several hundred runs of autumn 1994 is shown as lego–stacks mounted on a cylindrical surface.

4.6.1   Single pad efficiencies

A measurement of the efficiencies of each pad is necessary to describe the behavior of the MWPCs in detail. To measure these efficiencies we take fully reconstructed driftchamber tracks, extrapolate them to the layers of the MWPCs and check in a restricted region on the surface of each layer if an active pad is found (see fig 4.15).
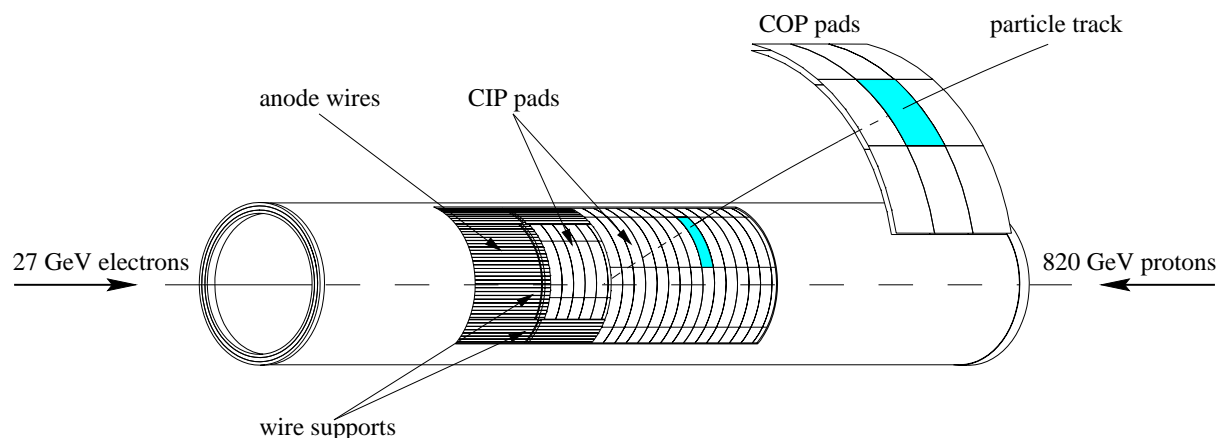
Figure 4.15: Efficiency measurement of single pads. A well isolated, fully reconstructed driftchamber track is extrapolated to the chamber surfaces. If near the intercept an active pad is found this pad is counted as efficient pad, otherwise the intercepted pad is counted as inefficient.

Those driftchamber tracks are selected as follows:

- Only tracks fitted to the primary event vertex with reasonable fitted track parameters (labeled *good* tracks) are used, to keep the calculated interception point as close as possible to the real intercept. In addition only tracks linked to both z–chambers (CIZ and COZ) were used to improve the track parameters.

- A track has to be reasonably separated from other tracks to avoid an overestimation of the measured efficiency due to near hits.

- Only *unbiased* tracks are to be used for an efficiency determination. Tracks from events triggered by an MWPC trigger, such as the z–Vertex trigger, have a higher probability to point to active pads than ordinary tracks.

- At H1, most of the particles reaching the central tracker are pions. A few percent of the particles are protons, kaons, electrons and muons. Especially protons and kaons deposit more energy in the sensitive detector parts than pions of same momentum. An overestimation of the measured efficiency arises, if other particles than pions are used for an efficiency determination.

A track fitted to the primary event vertex is labeled a good track if its transverse momentum is at least 100 MeV, its value for d_{ca} is less than 2 cm and the vertex has to be within 50 cm along the z–axis to the nominal H1 interaction point. The track length within the two driftchambers CJC1 and CJC2 has to be at least 15 cm to guarantee for an accurate determination of the track parameters.

Isolated tracks are selected as follows. For each intercept of a good track with a MWPC chamber surface in an event the distances to all other intercepts of the remaining tracks (good and bad, inclusive non–vertex fitted) are determined. The shortest distance is used to check whether the isolation criterion is fulfilled or not. This is done on each of the MWPC layers individually and only tracks fulfilling the isolation criterion on each layer are used for an efficiency determination. Figure 4.16 shows the efficiency of CIP and COP as function of this nearest distance. At very small distances, $d < 2 - 3$ cm, the efficiency is lower than at $d \approx 5$ cm. This is an artifact of particles which are, due to multiple scattering, wrongly fitted to two different tracks. Most of the tracks do not fulfill the isolation criterion as the error bars in fig 4.16 show and large event samples are therefore required.

Finding unbiased tracks is a problem too, since the z–Vertex trigger is used as logical *and* or *or* in almost any subtrigger combination. A more complicated scheme has therefore been adopted to find unbiased tracks. A track is considered unbiased, if the event would have been accepted without the presence of the track. The hardware reliability of the z–Vertex trigger is close to 100% and therefore a full simulation of the z–Vertex trigger requires only its input values. Rerunning the z–Vertex trigger simulation on a reduced input data set, from which all intercepted pads together with their closest neighbors are removed (at most $4 \times 9 = 36$ pads), yields the z–Vertex trigger decision for the event without the track in operation. If the z–Vertex trigger decision didn't change the track is considered as unbiased track and can be used for efficiency measurement of the proportional chambers. Typically 10% of good tracks are found to be biased.

Selecting pions is only possible if the particle's momentum is not too large, and the measured of the energy loss can be used for the identification. The H1 track reconstruction module includes among the track parameters also a value for the energy loss dE/dx. This quantity is normalized to the mean energy loss for minimum ionizing particles (*mips*). With an additional cut on $dE/dx \in (0.6 \ldots 1.6)$ (see fig 4.17) low momentum kaons and protons with large energy losses are eliminated.

With a significantly set of good, isolated and unbiased particle tracks the pad efficiencies can now be determined. Still some care has to be taken, as in addition to the geometrical position the efficiency also depends on the polar angle ϑ because the length of the chamber gap varies with $1/\sin\vartheta$.

An inspection of figure 4.14 points to a second problem. Noise contributes a non-negligible amount to the number of active pads. For the efficiency determination the contribution from noise is subtracted statistically. Whenever a pad is found active, it is not clear whether it was active due to noise or whether it was active due to a particle passing the layer plane. Pads found inactive even when a particle passed its layer are clearly free of
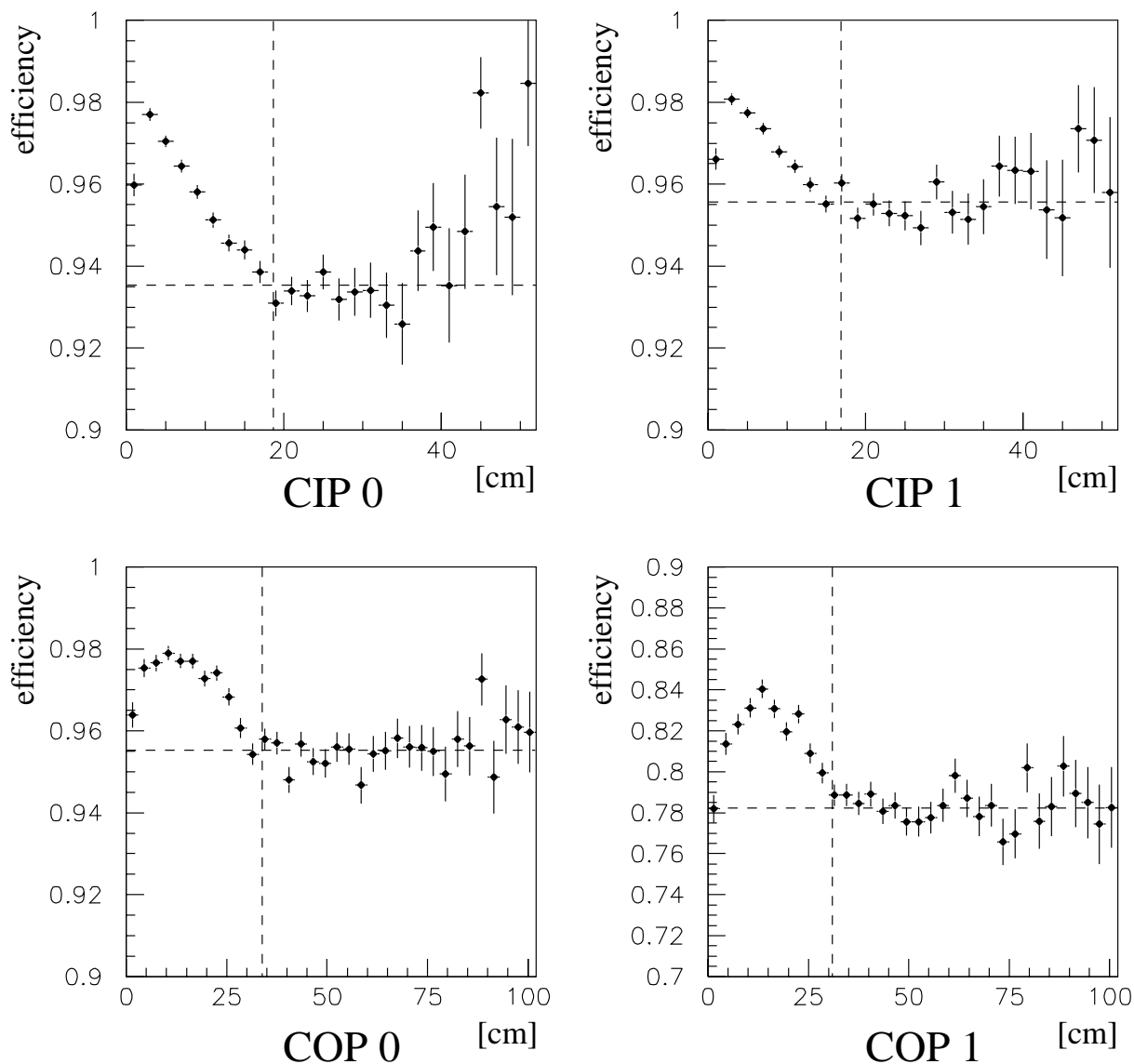
Figure 4.16: Isolation cut on driftchamber tracks. The MWPC efficiency is shown as a function of the distance of the intercept of the track used for the efficiency determination to the nearest intercept of all other tracks within the same event.

noise and inefficient. This leads to following formulation for noise corrected efficiency:

$$\varepsilon = 1 - \frac{\#\ \text{pad off}}{\#\ \text{pad tested} - \#\ \text{expected noise}} \qquad (4.12)$$

The expected noise can be determined from the history of the tested pad. In the readout pipeline (see section 3.6) not only the actual event is stored, but also the activity of the MWPCs some bunch crossings earlier and later. To exclude events triggered too early,
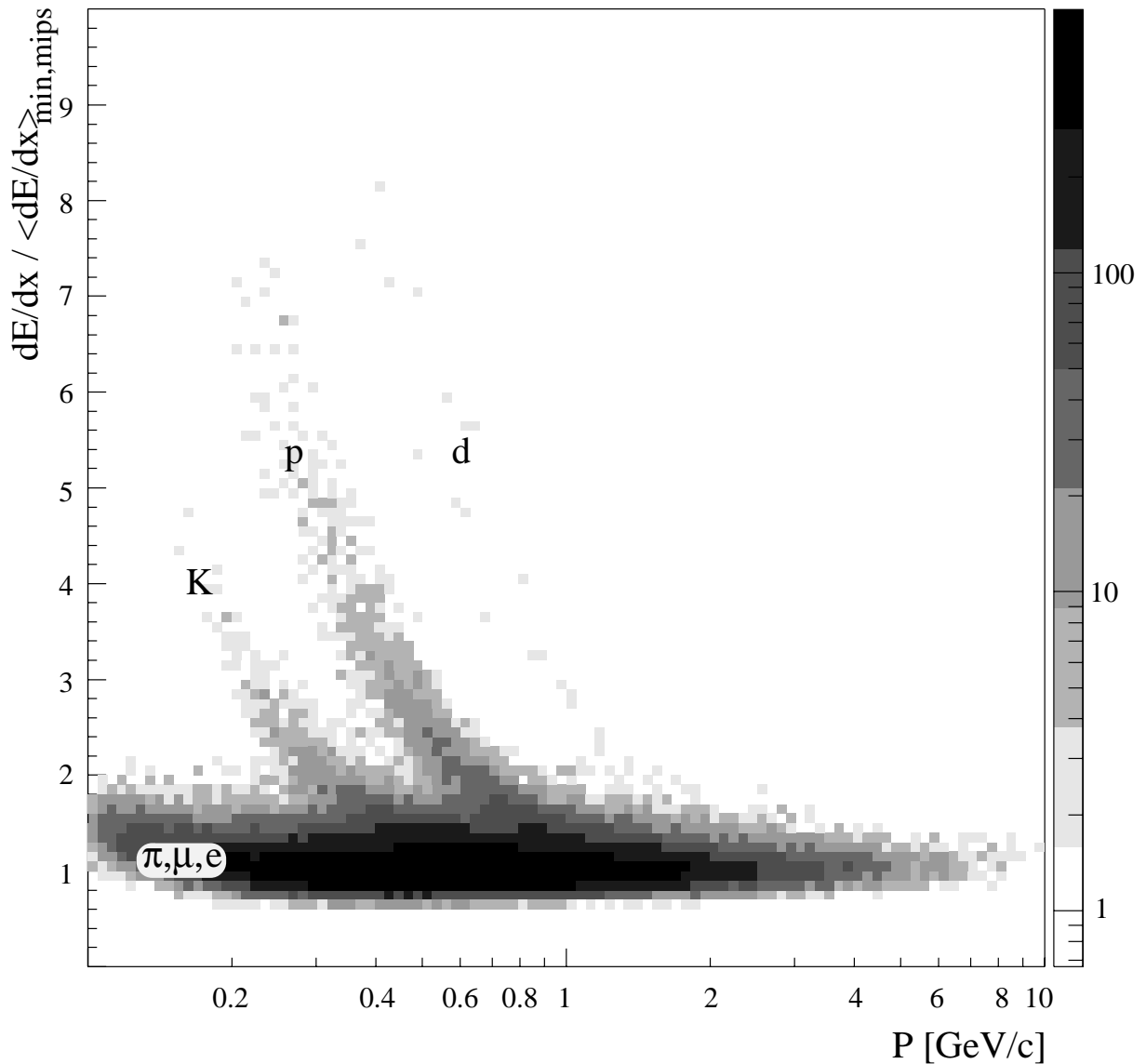
Figure 4.17: Energy loss of charged particles as measured in the H1 central tracker. At not too large momenta, kaons, protons and deuterons can be distinguished from pions, muons, and electrons.

the status of the pad is checked two bunch crossings before the actual bunch crossing of the event. If the pad is found active, it is counted as noisy.

Figure 4.18 shows a two dimensional map of measured efficiencies of CIP and COP pads. The granularity of the shaded map is coarse for low efficiency values and fine in the region above 90%. No cut was performed on the polar angle ϑ and therefore, as the ep–interaction point is centered along the z–axis, pads not being centered along z are hit mostly by flat tracks and show higher efficiencies. Central driftchamber tracks do not cover the whole
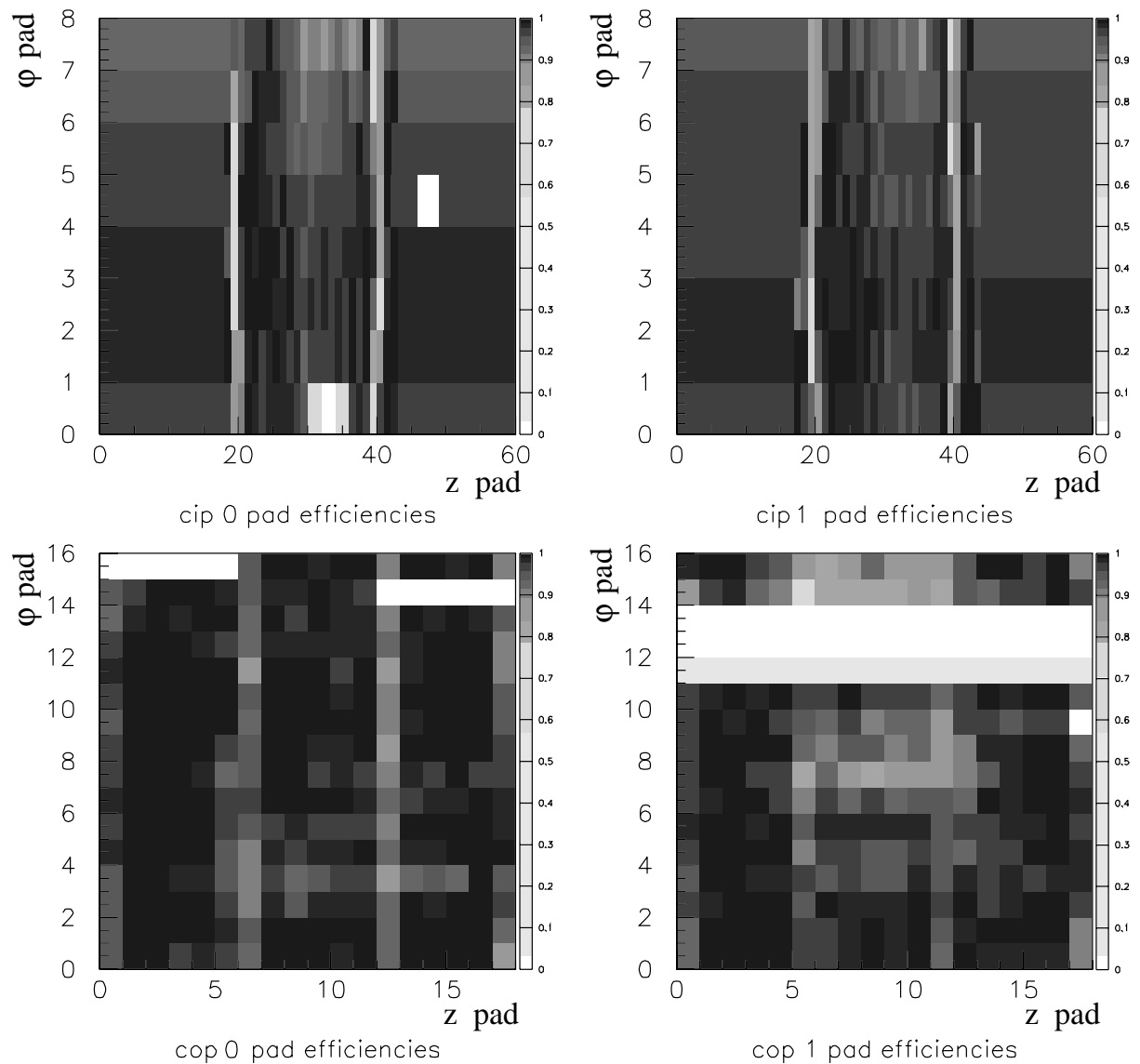
Figure 4.18: Efficiencies of CIP and COP pads. Dead channels and a decreased efficiency due to the wire–supports of the chambers is visible. For CIP only the central part can be measured with CJC driftchamber tracks.

area of CIP (see fig 3.3 for a sketch of the central tracker), therefore a guess, determined from the averaged values for each φ–segment, is plotted. Pad–efficiencies which fluctuate too much e.g. dead channels, are not used for the determination of that guess. Dead regions are visible as white areas (cf. fig 4.14). At pad numbers 19 and 39 for CIP and 6 and 12 for COP the efficiency decreases because the anode wires are supported there (see fig 4.15). The same argument holds for the very first and very last pad along z of COP.

4.6.2 Trigger pads

The question arises, if the noise seen predominantly in COP 0 and the large inactive regions of COP 1 prohibit sensitive triggering. The preset bit has been set on the dead channels of COP 0 and COP 1. Luckily none of the trigger rays required more than one preset bit which means, that rays are formed either from a four out of four or from a three out of three coincidence.
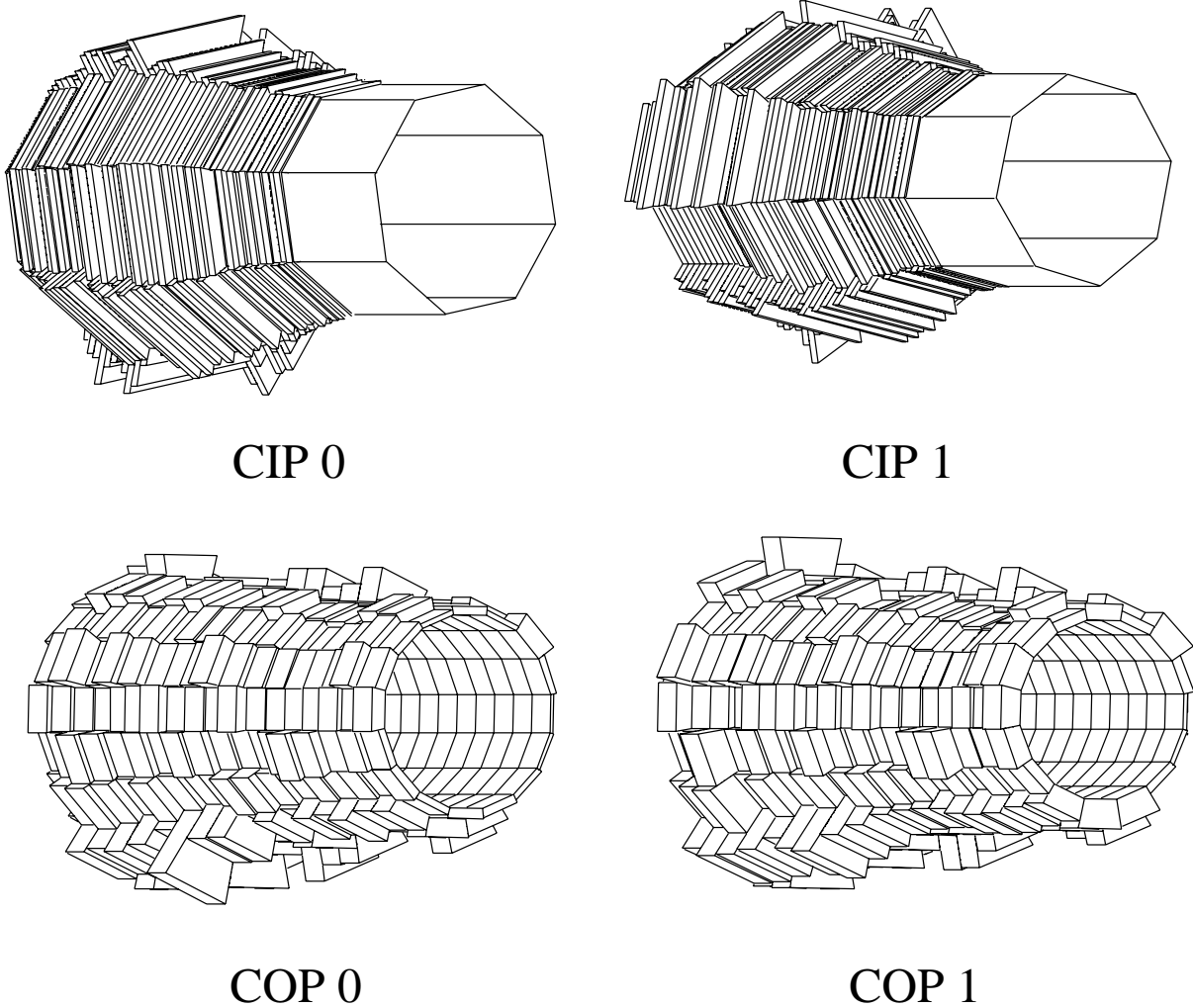

Figure 4.19: Hitmap of relevant trigger pads. Only those pads actually involved in the z–Vertex trigger enter this hitmap. Neither dead regions nor noise are visible in this map.

z–Vertex trigger rays are not read out separately but can be calculated from the proportional chamber pads. Taking the ray table and all active rays a hitmap for pads relevant to the z–Vertex trigger can be calculated. Figure 4.19 shows a three dimensional hitmap

of the for the z–Vertex trigger relevant pads. No dead channels are seen which is a direct proof of properly working preset bits. On the contrary, the dead channels show an increased activity, also visible along the cones of the rays in the other chambers (especially the bottom segment of all four chambers). Of vital importance is the fact, that the noisy region of COP 0 (see fig 4.14) is no longer seen and therefore does not influence the selectivity of the z–Vertex trigger.

The backward region of CIP is not used for z–Vertex triggering and the corresponding pads to not populate this special hitmap[†].

More information can be deduced from these maps. If the simulated response does not match the actual response, hardware problems like missing rays, e.g. caused by single pads can be traced. If enough statistics is accumulated, a hole or a peak indicates a problematic channel.

4.6.3   Single track efficiencies

The response of the z–Vertex trigger depends on the event topology. No easy measurement of single track acceptance is therefore feasible, except by selecting those rare events with exactly one good, unbiased track within the H1 central tracker.

An alternative scheme, based on the knowledge of the impact of good,unbiased and isolated tracks on the proportional chambers, has been developed. Not always exactly the intercepted pad activates when a particle passes, it is also possible that some of the neighboring pads activate. For a determination of single track acceptances all active pads of the within the cluster of nearest neighbors of the pad in question are extracted from the actual event and stored in a CRME bank (in maximum $4 \times 9 = 36$ pads). The z–Vertex simulation package (see fig 4.5) is then able to determine if this track alone would enable rays. As the whole setup of the z–Vertex trigger enters into this calculation, all deviations from the standard setup are taken into consideration automatically. Figures 4.20 and 4.21 show the results of such an investigation.

The typical transverse momentum $p_\perp$ of driftchamber tracks lies in the region of $\approx \pm(0.2 \ldots 2)$ GeV as can be seen from the unshaded histogram in the upper left plot of figure 4.20. A long tail going up to very large values of $p_\perp$ is not shown. The shaded histogram corresponds to tracks enabling at least one ray of the z–Vertex trigger. The ratio between these two histograms (shaded and unshaded) is seen in the lower left plot, it determines the efficiency of the z–Vertex trigger for single rays. The efficiency as function of transverse momentum $p_\perp$ shows the typical rise which has been discussed in

---

[†]From fig 4.2 it becomes evident that no trigger rays can be formed which involve the backward region of CIP.
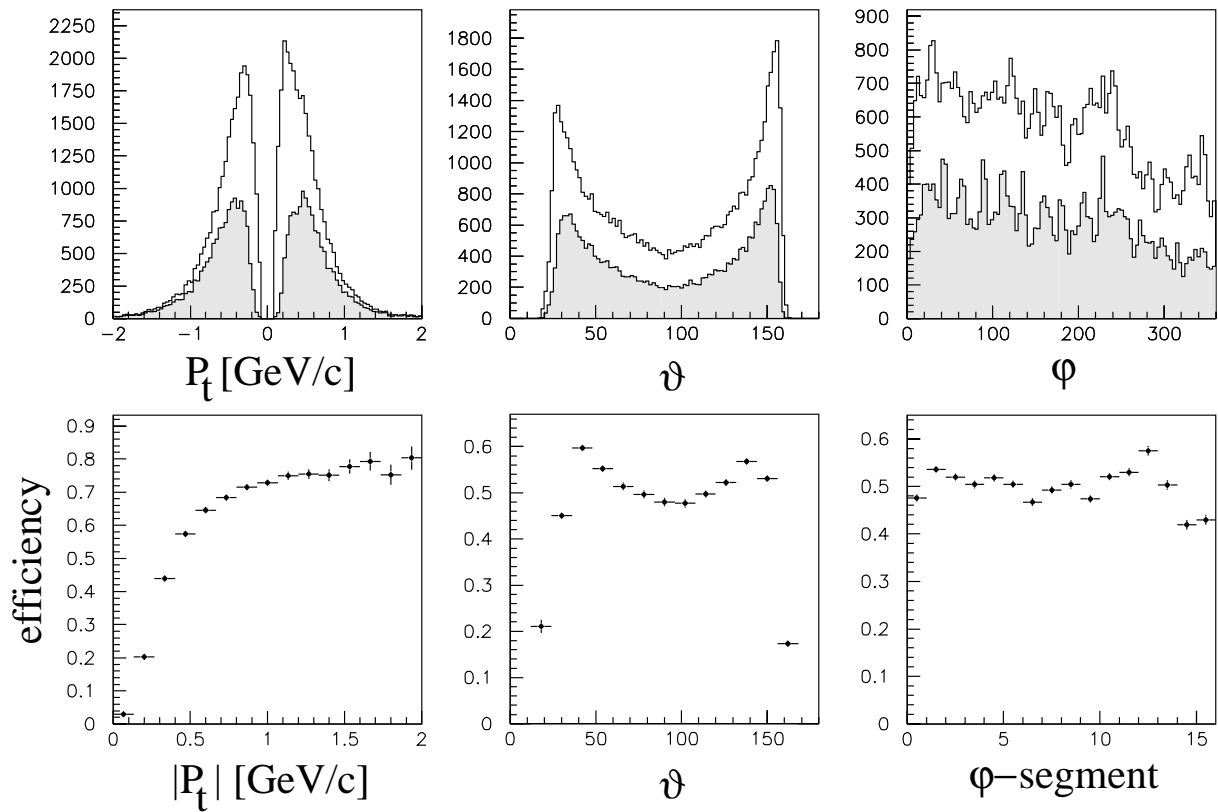
Figure 4.20: Efficiencies for single tracks. The distribution of different parameters of good, unbiased CJC–driftchamber tracks is shown. The shaded area corresponds to tracks enabling at least one ray of the z–Vertex trigger. The ratio between two histograms determines the efficiency of the z–Vertex trigger for single tracks.

section 4.5. For transverse momenta > 1.5 GeV/c dips are seen in the efficiency curve. These are understood as interferences which occur in the superposition of acceptances of tracks with a typical d_{ca} of ± 0.7 cm (see fig 4.11).

Tracks crossing the MWPC at right angles deposit less charge in the active gap and are therefore less efficient. Very forward and backward tracks have little chance to reach COP and escape therefore from the z–Vertex trigger acceptance.

A broken anode–wire in the COP makes φ–segments 11,12 and 13 unusable. Therefore the preset bit has been set on these channels which results in a higher efficiency in those segments. CIP 0 had problems in φ–segments 15,0 ($\widehat{=}\varphi$–segment 0 in the eight–fold numbering scheme of CIP) which decreased the efficiency in the corresponding segments.

The H1 interaction point was not aligned with the z–axis during 1994 data taking period but shifted ≈ 0.7 cm in the r–φ plane. The distribution of the values of distance of closest
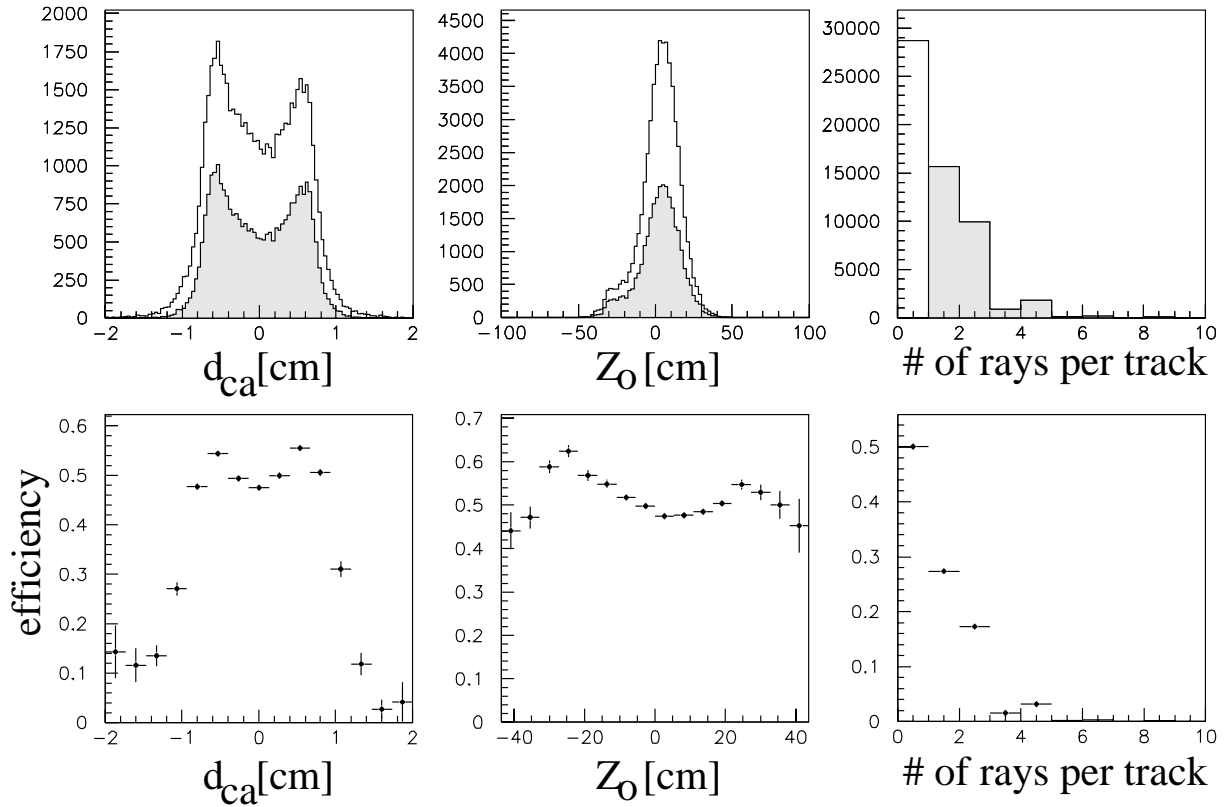
Figure 4.21: Efficiencies of single tracks. See text and figure caption 4.20 for an explanation of these plots.

approach d_{ca} peaks therefore ± 0.7 cm. Only particles crossing accidentally the z–axis have a vanishing d_{ca} which is only possible for tracks having a particular azimuthal angle φ.

The origin along the z–axis of the track (Z_0) is linked to the polar angle ϑ. Only flat tracks reach the layers of CIP and COP for extra large values of Z_0. This link tends to increase the efficiency for tracks with a large offset ($|Z_0| > 20$ cm).

If a track is efficient in the z–Vertex trigger, very often more than one is ray activated. Especially in those regions where preset bits are enabled up to 4 rays per track are regularly seen, in extreme cases even up to 8 rays are possible. This causes special problems for the understanding of those z–Vertex trigger elements derived from the whole topology of the z–Vertex histogram such as the z–Vertex– $\sigma_{1,2}$, *small* and *cluster* bits.

4.7   Monte–Carlo description of the z–Vertex trigger

A direct measurement of the event based efficiency of z–Vertex triggered events is only feasible in those rare cases where the full event–topology is covered by a complete in-

dependent trigger. This is not the case for all event classes and hence a sophisticated Monte–Carlo description of the response of the z–Vertex trigger based on our efficiency measurements is needed.

In the following we describe the procedure used.

4.7.1 Digitization of the response of multiwire proportional chambers with cathode pad readout

A fast, charged particle traversing the gaseous volume of a MWPC looses energy mainly through electromagnetic interactions with atomic electrons[†]. The mean energy loss per path length can be obtained from the well known Bethe–Bloch formula [63, 64]:

$$\frac{\mathrm{d}E}{\mathrm{d}x} = -K\frac{Z}{A}\frac{\rho}{\beta^2}\left\{\ln\frac{2m_ec^2\beta^2E_{\max}}{I^2(1-\beta^2)} - 2\beta^2\right\}, \qquad K = \frac{2\pi Nz^2e^4}{m_ec^2} \qquad (4.13)$$

where N is the Avogadro number, m_e and e are the electron mass and charge, Z, A and ρ are the atomic number and mass and the density of the gas medium respectively, and I is its effective ionization potential. z and β are charge and velocity of the traversing particle.

The quantity $E_{\max}$ represents the maximum energy transfer to an atomic electron in a single collision:

$$E_{\max} = \frac{2m_ec^2\beta^2}{1-\beta^2} \qquad (4.14)$$

In thin materials the total energy loss is given by a small number of collisions, each with a wide range of possible energy transfers. This determines the characteristic shape of the Landau distribution for the total energy loss [65]:

$$f(\lambda) = \frac{1}{\sqrt{2\pi}}e^{-\frac{1}{2}(\lambda+e^{-\lambda})} \qquad (4.15)$$

The reduced energy variable λ represents the normalized deviation from the most probable energy loss ΔE_{mp}:

$$\lambda = \frac{\Delta E - \Delta E_{\mathrm{mp}}}{\xi}, \qquad \xi = K\frac{Z}{A}\frac{\rho}{\beta^2}x \qquad (4.16)$$

Such a Landau distribution is shown in fig 4.23. A relatively sharp rise is followed by a long tail extending to large energy losses (up to $E_{\max}$) corresponding to events where one or more energetic δ–electrons have been produced.

[†]An overview of principles of operation of multiwire proportional and drift chambers can be found in [62]

During the passage of the particle a discrete number of collisions generate the primary electron–ion pairs in the medium. If the ejected electrons are sufficiently energetic, further ionizations take place producing secondary ion pairs. If on average an energy W_i is needed to produce one ion pair on gas component i, the total number of ion pairs can be computed:

$$n_T = \frac{\Delta E}{\overline{W_i}} \tag{4.17}$$

Charges produced by an ionizing event quickly lose their energy in multiple collisions with the gas molecules and assume the average thermal energy distribution of the gas. Electrons move much faster than ions (because of their small mass) and have an average thermal velocity of about 10 cm/μs whereas ions are about 100 times slower. When an electric field is applied across the gas volume, a net movement of the charges along the field lines is seen. At large electric fields ($>$ few kV/cm), electrons can gain enough energy between two collisions to produce inelastic phenomena such as excitations of various kind and ionization. The process of ionization is the basis of the avalanche multiplication in proportional chambers. Only very close (few 10 μm) to the anode wire the field grows high enough ($E \sim 1/r$ for small r) to allow avalanche multiplication which enlarges the tiny signal from the few primary ion–pairs by factors of up to 10^{5-7} and more. The total charge collected on the anode wire induces a signal on the cathode plane which can be calculated using a simple electro–static model and neglecting any effects from the anode wires itself.

With the method of mirror images Endo [66] obtains for a point like charge dQ placed on the anode wire plane at $(x,z) = (0,0)$ (see fig 4.22 left) a charge density $\sigma(x,z)$ on the cathode plane at distance l from the anode:

$$d\sigma(x,z) = -\frac{dQ}{2\pi} \sum_{n=0}^{\infty} (-1)^n \frac{(2n+1)l}{((2n+1)^2 l^2 + x^2 + z^2)^{3/2}} \tag{4.18}$$

The total charge collected per unit length on the anode wire is proportional to the total energy loss of the particle within an active region $d \leq l$, from which electrons from the primary ionization process of the particle reach the anode wire:

$$\frac{dQ}{dz'} = \frac{M}{|\cos\vartheta|}\frac{dQ}{ds} \sim \frac{1}{|\cos\vartheta|}\frac{dE}{ds} \tag{4.19}$$

with M being the gas amplification factor and s being the path length of the track within the active region. Assuming a homogeneous distribution of charge along the anode wire,
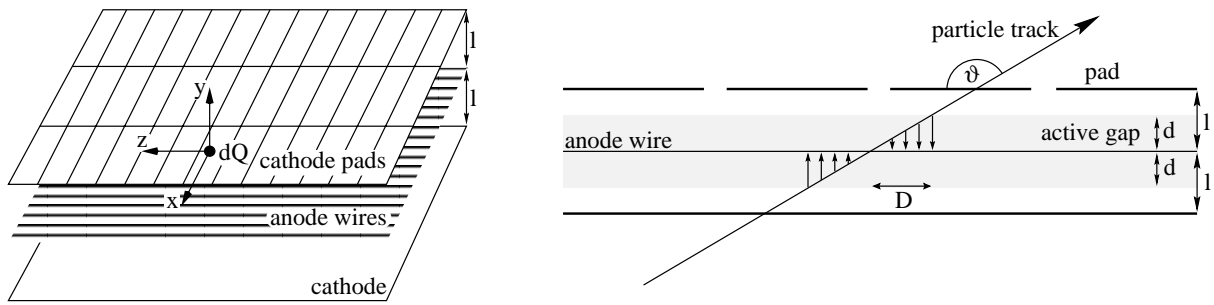
Figure 4.22: Charge distribution on cathode pads of a track passing the sensitive region of a MWPC.
left: The coordinate system used to describe the induced charge density on the cathode plane is taken such, that the charge dQ is located in the origin.
right: Charge distribution of a particle track. Electrons from the primary ionization process of the particle track from within an active region around the anode wire drift along the field lines towards the anode. Close to the anode, the avalanche multiplication takes place which leads to a considerable amount of charge distributed homogeneously along the anode.

the charge density on the cathode plane can by calculated:

$$\sigma(x, z) = \int_0^Q \sigma(x, z - z')\, dQ(z') \tag{4.20}$$

$$\sim \frac{1}{|\cos\vartheta|} \frac{dE}{ds} \int_{-D}^D \sigma(x, z - z')\, dz' \tag{4.21}$$

with D being half the length along the anode wire where charge is collected (see fig 4.22 right). Simple trigonometry yields:

$$D = \frac{d}{|\tan\vartheta|} \tag{4.22}$$

with d being the lateral size of the active region.

A further integration over the pad area leads to the total induced charge per pad:

$$Q_{\text{pad}} \sim \frac{1}{|\cos\vartheta|} \frac{dE}{ds} \iint_{\text{pad}} \int_{-D}^D \sigma(x, z - z')\, dz'\, dx\, dz \tag{4.23}$$

Figure 4.23 (middle and right) shows the calculated total induced charge in arbitrary units on the pads of CIP 0 from stiff tracks coming from the nominal H1 interaction point, as function of polar angle ϑ of the track. No Landau–fluctuation has been applied

in the plot in the middle and therefore the pad geometry is clearly visible. The induced charge of a track passing exactly between two pad boundaries is shared between those two pads which leads to characteristic dips seen in the figure. The envelope of this curve follows exactly a $1/\sin\vartheta$ behavior. Applying Landau–fluctuations yields the plot seen on the right side, where the dips between successive pad boundaries are still visible. Extra large values of induced charge per pad of more than 30 times the average value of induced charge from tracks passing perpendicular the chamber plane are possible for flat tracks.

A pad is active, if the total charge on a pad collected from all particle tracks crossing the active region of the MWPC exceed a for each pad individual setable threshold T_{pad}.
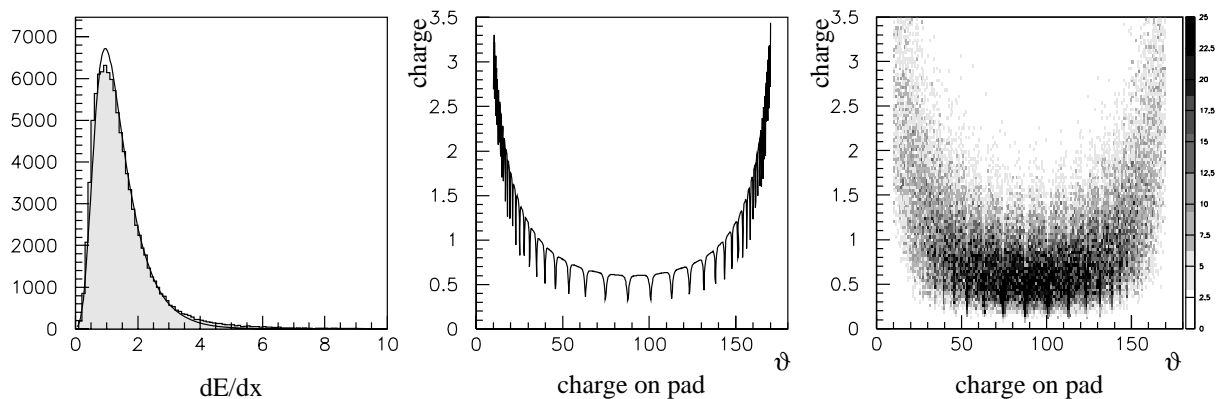

Figure 4.23:   Induced charge vs. polar angle ϑ.
left: Measured Landau–distribution for minimum ionizing particles for a constant step length of 1 cm. The fitted line corresponds to eq. (4.15).
middle: Induced charge in arbitrary units from stiff tracks traversing the chamber's layer on the hitten pad of CIP 0 stiff tracks traverse, as function of the polar angle ϑ of the track, before Landau–fluctuations are taken into account.
right: dito, but with Landau–fluctuations.

4.7.2   Monte–Carlo implementation of the digitization scheme

Any particle track generated by one of the various existing Monte–Carlo generator programs, such as PYTHIA [67], PHOJET [68], HERWIG [69], ARIADNE [70] and many others, is a result of a model calculation, taking only into account pure genuine ep–physics in vacuum.

Each generated particle track has then to be guided through the massive material of the H1 detector. This is done using the GEANT [71] package, a specialized program taking electromagnetic and hadronic interactions of the particle with the surrounding material

into account, such as multiple interactions and showering, as well as decays of particles in flight such as $\pi \to \mu\nu_\mu$ or $\mu \to e\nu_\mu\nu_e$; all of which produce lots of secondary particles.

Each of these secondary particles is then, in an iterative process, further treated by GEANT up to a minimum momentum scale of each of these secondaries.

The output of GEANT contains the simulated tracks stored in the STR bank (see table 4.12) and the points where particles intercept sensitive detector parts.

For the MWPCs, these hits are stored in the CRMT and FRMT bank respectively (see table 4.13).

TABLE **STR**		I			simulated tracks
COL	ATT–name	FMT	Min	Max	Comments
1	PX	F	$-\infty$	$+\infty$	*momentum p_x [GeV]*
2	PY	F	$-\infty$	$+\infty$	*momentum p_y [GeV]*
3	PZ	F	$-\infty$	$+\infty$	*momentum p_z [GeV]*
4	E	F	0	$+\infty$	*energy [GeV]*
5	IPDG	I	-99999	+99999	*PDG particle code [72]*
6	ITRHIS	I	0	767	*tracking history word*
	REL–bank	TYPE	INT–bank		Comments
7	STR	MOTHER			*pointer to parent particle in STR bank*
8	GTR	D1T1			*pointer to particle in GTR bank*
9	SVX	DMT1			*pointer to vertex number in SVX bank*

Table 4.12: Contents of the STR bank.

The digitization step then has to calculate the expected response of the sensitive detector parts from the passing simulated particles.

The routine CMDIGI takes as input the points where the simulated tracks intercept CIP and COP and from the particle mass and momentum and calculates the energy loss[†] and the total induced charge per pad as described above. The charge values are stored in the CRMP bank (see table 4.14). Analogue, the routine FMDIGI calculates the total charge on each of the forward proportional chamber pads and stores it in the FRMP bank.

Once the induced charge par pad is known, it has to be checked whether its value is above a threshold and the corresponding pad is active or not. This is done in the routine CMPME for CIP and COP pads and in FMPME for FPC pads respectively. Simultaneously, wrongly connected pads (due to cabling errors in 1992 and 1993) are remapped. The

---

[†]Non prominent secondary particles point to the original simulated track and the wrong momentum and mass is taken. In case of CIP and COP this error is negligible, as only a small fraction ($\approx 1\%$) of a radiation length has to be passed from the H1 interaction point to the layers CIP and COP.

TABLE **CRMT**		I			central response MWPC track
COL	ATT–name	FMT	Min	Max	Comments
1	ICH	I	0	3	*chamber number; 0: CIP 0, ... 3: COP 1*
2	XENTRY	F			*x–coordinate of entry point of track*
3	YENTRY	F			*y–coordinate of entry point of track*
4	ZENTRY	F			*z–coordinate of entry point of track*
5	XEXIT	F			*x–coordinate of exit point of track*
6	YEXIT	F			*y–coordinate of exit point of track*
7	ZEXIT	F			*z–coordinate of exit point of track*
8	ITRHIS	I	0	767	*tracking history word*
	REL–bank	TYPE	INT–bank		Comments
9	STR	DMT1			*pointer to track number in STR bank*

Table 4.13: Contents of the CRMT bank. Each pair of hits belongs to one simulated track found in the STR bank. The FRMT bank is built analogous, denoting entry and exit points of tracks in the FPC.

TABLE **CRMP**		I			central response MWPC accumulated charge per pad
COL	ATT–name	FMT	Min	Max	Comments
1	NPAD	I	0	1535	*pad number*
2	PADQ	F	0	$+\infty$	*accumulated charge*

TABLE **FRMP**		I			forward response MWPC accumulated charge per pad
COL	ATT–name	FMT	Min	Max	Comments
1	NPAD	I	0	1151	*pad number*
2	PADQ	F	0	$+\infty$	*accumulated charge*

Table 4.14: Contents of CRMP and FRMP banks.

output of these simulation routines contains then the simulated active pads and is stored in the CRME and FRME banks (see table 4.1), the same banks as for real data. These banks allow now for a determination of the simulated response of the z–Vertex trigger as can be seen from figure 4.5 (flow chart of z–Vertex trigger simulation).

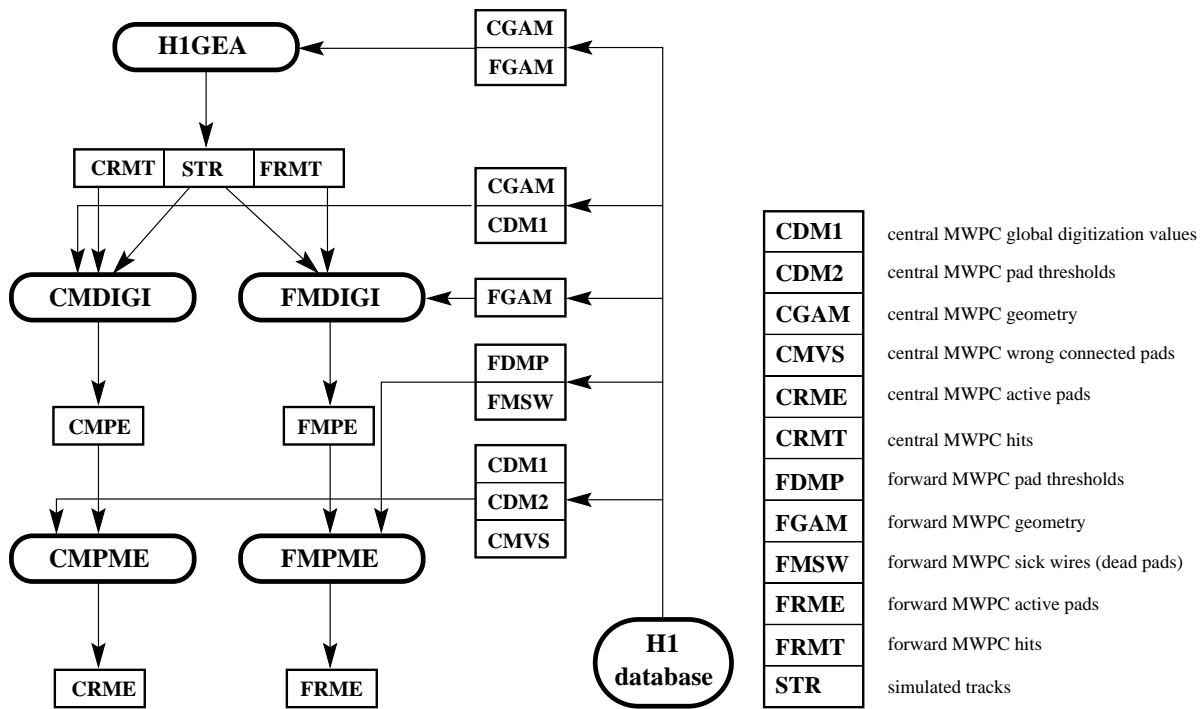Figure 4.24 shows the flow chart of the digitization step for the MWPCs.

CDM1	central MWPC global digitization values
CDM2	central MWPC pad thresholds
CGAM	central MWPC geometry
CMVS	central MWPC wrong connected pads
CRME	central MWPC active pads
CRMT	central MWPC hits
FDMP	forward MWPC pad thresholds
FGAM	forward MWPC geometry
FMSW	forward MWPC sick wires (dead pads)
FRME	forward MWPC active pads
FRMT	forward MWPC hits
STR	simulated tracks

Figure 4.24: Flow chart of the MWPC digitization step.

4.7.3 Tuning of the digitization parameters to real data

For an accurate Monte–Carlo description of the MWPCs, all free parameters of the digitization model have to be tuned to best knowledge to the effective conditions which were valid during the data taking period. As run conditions may have changed (broken wires, new high–voltage settings, new discriminator thresholds, new gas composition, ageing, ...) eventually more than one set of digitization parameters has to be prepared. The production of simulated ep-events has to take track on all actual run–conditions and a weighting of the event statistics, according to the actual integrated luminosity for each period of constant conditions during ep data–taking, is necessary.

The free (tune able) parameters in the current digitization model for CIP and COP are the following:

active gap the lateral size d of the active region (see fig 4.22 left). For CIP 0,1 and COP 0,1 one number each. The distance from anode to cathode is 3 mm (4 mm) for CIP (COP) which determines the maximum possible value for d.

threshold the minimum total induced charge per pad necessary to activate a pad. For each of the 1536 cathode pads an own threshold can be given. Dead channels are tagged with negative but otherwise arbitrary values.

crosstalk   the fraction of induced charge per pad which couples to neighboring pads. For each chamber one number for crosstalk to neighbor pads along z and one number each for crosstalk to neighbor pads along φ is given. (The induced charge is already distributed to several pads according equation (4.23), therefore only if the coupling should be stronger (weaker), the crosstalk parameters become important.

dead HV   For CIP, 16 high voltage segments feed 8 φ cathode pad segments which gives a pad the possibility being efficient on one half side and being totally inefficient on the other half side.
For COP, 16 high voltage segments feed 16 φ cathode pad segments. Whole φ segments can be disabled this way.

These values, once they are found, are stored in two different banks within the global H1 database. The values for *active gap*, *crosstalk* and *dead HV* have to be set by hand and are stored in the CDM1 bank (see table 4.15). The 1536 threshold values are determined from CDM1 and the measurement of the chamber efficiency using CJC driftchamber tracks. These are stored in the CDM2 bank (see table 4.16).

TABLE **CDM1**		I			digitization parameters for MWPCs
COL	ATT–name	FMT	Min	Max	Comments
1- 2	ACTGAP	F	0.0	0.3	*width [cm] of active gap for CIP*
3- 4	ACTGAP	F	0.0	0.4	*width [cm] of active gap for COP*
5- 8	ZCROSS	F			*crosstalk to z neighbor for CIP0 ... COP 1*
9-12	PCROSS	F			*crosstalk to φ neighbor for CIP0 ... COP 1*
13-28	HV_ON	I	0	1	*flags for the 16 high voltage segments of* CIP *0*
29-44	HV_ON	I	0	1	*flags for the 16 high voltage segments of* CIP *1*
45-60	HV_ON	I	0	1	*flags for the 16 high voltage segments of* COP *0*
61-76	HV_ON	I	0	1	*flags for the 16 high voltage segments of* COP *1*

Table 4.15: Contents of the CDM1 bank.

The values for the *dead HV* flags are easy to determine, as these values should be known to the chamber operator, all other values rise to more effort.

As the digitization scheme already allows for a distribution of induced charge over several pads, *crosstalk* has been switched off.

TABLE **CDM2**		I			digitization parameters for MWPCs
COL	ATT–name	FMT	Min	Max	Comments
1	GLOBFA	F			*global factor for each threshold*
2	GFCIP0	F			*global factor for CIP 0 thresholds*
3	GFCIP1	F			*global factor for CIP 1 thresholds*
4	GFCOP0	F			*global factor for COP 0 thresholds*
5	GFCOP1	F			*global factor for COP 1 thresholds*
6- 485	TCIP0	F			*thresholds for CIP 0, dead if negative*
486- 965	TCIP1	F			*thresholds for CIP 1, dead if negative*
966-1253	TCOP0	F			*thresholds for COP 0, dead if negative*
1254-1541	TCOP1	F			*thresholds for COP 1, dead if negative*

Table 4.16: Contents of the CDM1 bank. The global factors ease studying effects of globally varying efficiencies.

The values for *active gap* and for *threshold* are not decoupled. A small active gap corresponds to a small path length for the particle track and therefore to a small signal on the anode wire. As the efficiency values are determined through a direct measurement small signals lead to small thresholds. The routine CMDIGI, which only calculates the induced charge up to an arbitrary factor, rescales the total induced charge per pad with the value of the *active gap*. The remaining net–effect of the so redefined *active gap* can be seen from the charge distribution per pad of particles crossing at the chamber plane at a given polar angle ϑ. As can be seen from figure 4.25, the rôle of the *active gap* is relevant for flat tracks only and controls the number of active pads per track for flat tracks.

The lower limit of accepted polar angle ϑ of CJC tracks is $\approx$25° and the upper limit is $\approx$155° (see fig 4.20). The effect of the *active gap* between these two extremes is minor and therefore all effort is put into finding the correct of the threshold values.

The program ZVTXTUNE2 is the tool to find an appropriate set of thresholds from the *ep*–data. A flow chart of this program is shown in figure 4.26. Fully reconstructed DST[†] events are used. This program runs over large data taking periods, therefore the status of the MWPC has to be checked by the program itself. The high voltage might be off on purpose or due to trips or the readout stream for the MWPC system might be excluded from data taking. Of minor importance is the possibility of the selection of certain subtriggers, as a possible bias is checked later for each track individually. The finding of good, CIZ and COZ linked, isolated and unbiased tracks has already been explained in section 4.6.1 as well as the measurement of pad efficiencies. For each intercept of a track with a chamber, the local hitmap is extracted. From these $4 \times 9 = 36$ pads the pad–activity
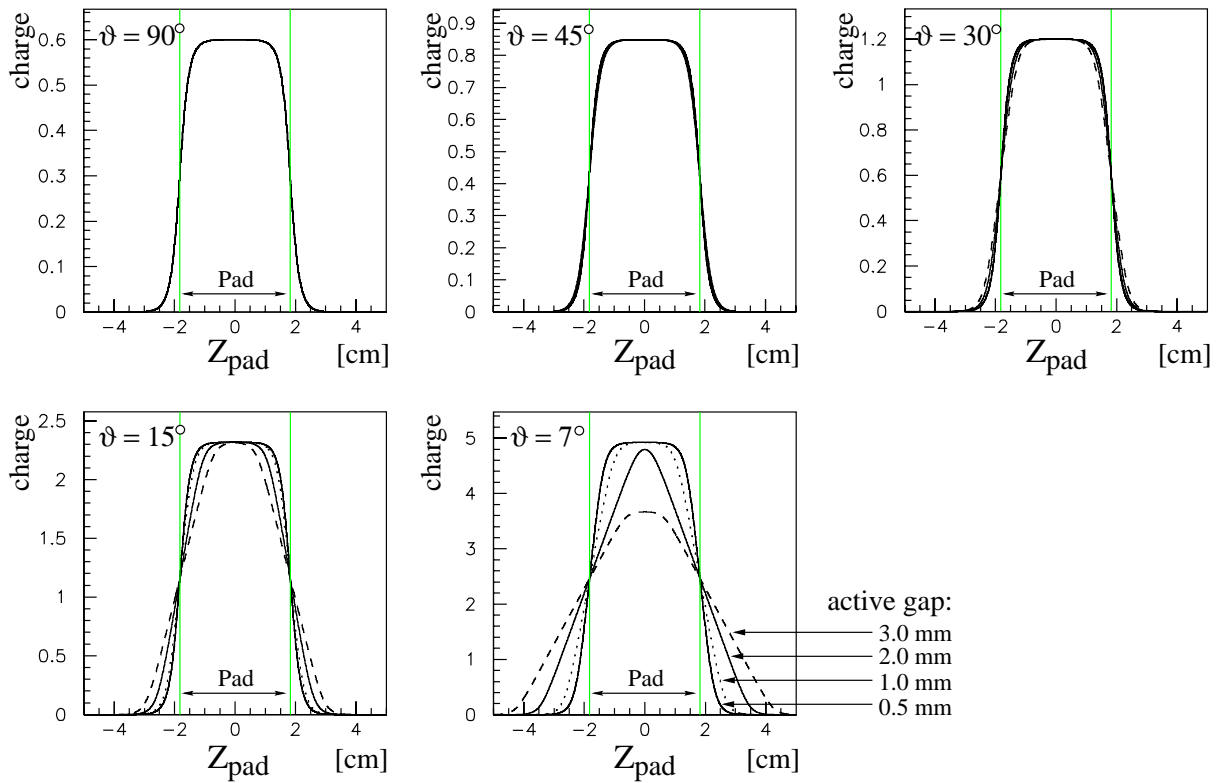

[†]DST = data summary tape

Figure 4.25: Charge distribution on CIP pads as function of the z–coordinate of the crossing particle track. ($z = 0$ cm if the track crosses the pad's center). The rôle of the *active gap* is relevant for flat tracks only.

and the number of active rays of the z–Vertex trigger per track is determined.

The heart of the program is the track simulation. The track parameters of each good, z–linked, isolated and unbiased track are used as input into the Monte–Carlo simulation scheme assuming the track to be a pion which is needed for the Monte–Carlo $\mathrm{d}E/\mathrm{d}x$ determination (an additional cut on the measured $\mathrm{d}E/\mathrm{d}x$ from the drift chamber selects mainly pions, see fig 4.17). In this way always identical distributions for data and Monte–Carlo of any track based variable is guaranteed. One systematic difference of such simulated tracks is, that they always point exactly to their intercept on the chamber, this is not the case for real data. Each track parameter is only measured to a certain accuracy and the true intercept is not identical to the one calculated from the track parameters. For that reason, the Monte–Carlo track gets the same parameters as the real track only up to a random correction derived from the covariance matrix resulting from the CJC track fit. All correlations between the track parameters are a result from the track fit and are considered in the random smearing of the Monte–Carlo track using appropriately correlated Gaussian distributions.
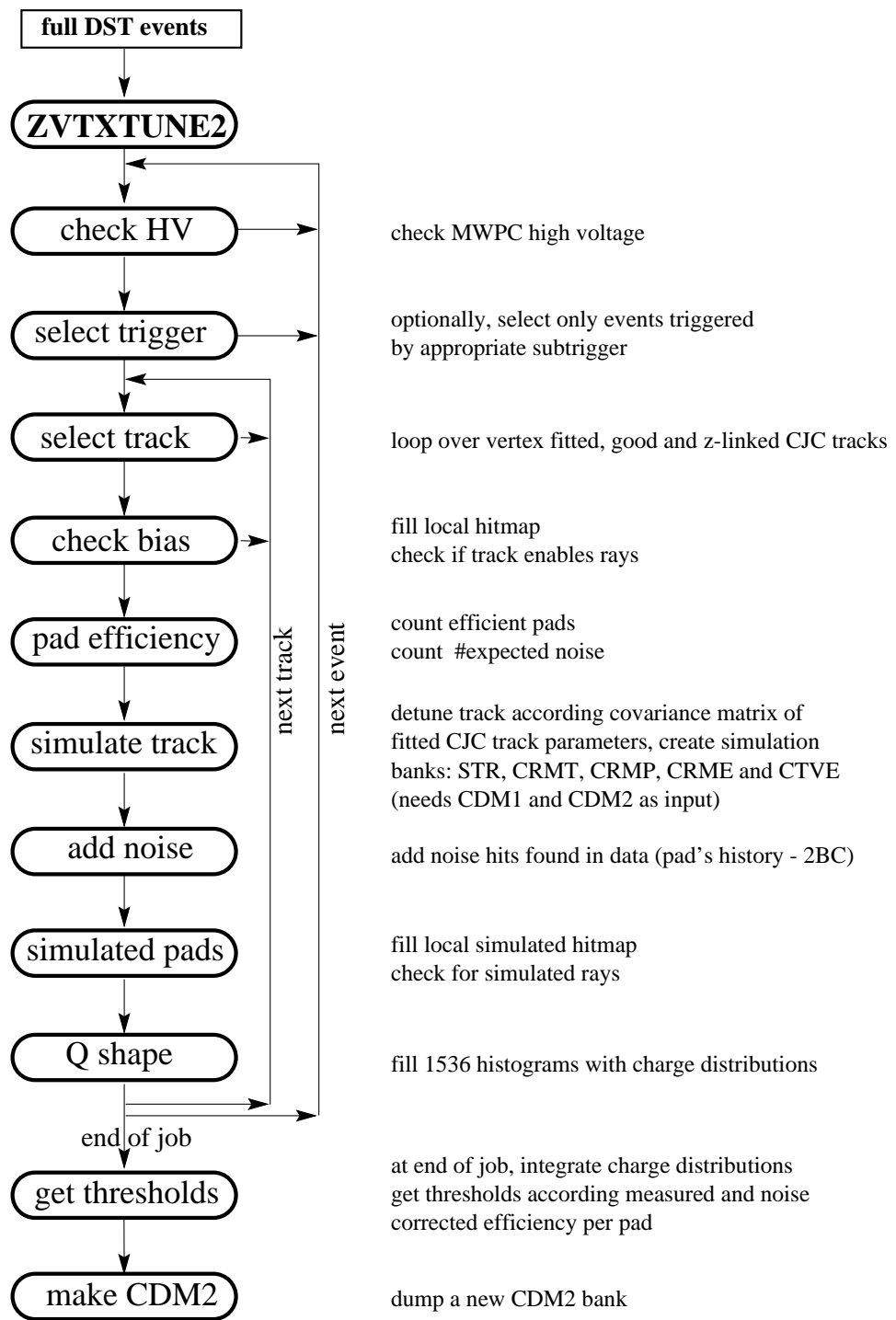
Figure 4.26: The program ZVTXTUNE2 determines the digitization parameters out of fully reconstructed ep–events. Each good, isolated and unbiased track is used as input into the simulation scheme.

From these smeared track parameters a STR and a CRMT bank are derived (see tables 4.12 and 4.13). A digitization of the MWPCs is now possible using all digitization parameters as input. For CDM1 this causes no problem whereas for CDM2 (the pad thresholds) a dummy input bank has to be provided.

Noise, as found in the pad's history from the real ep event, is added to the Monte–Carlo single track response of the MWPCs. Again a local hitmap can be derived from the simulated MWPC pads which then can be compared with the effective local hitmap from real data.

For a proper determination of the 1536 threshold values, the distribution of the total induced charge per pad is filled into 1536 histograms.

The last action is, after the last event has been worked through, the determination of the threshold values out of charge distributions and noise corrected efficiencies (see eq. (4.12)):

$$\varepsilon_{\mathrm{pad}} = \frac{\int\limits_{T_{\mathrm{pad}}}^{\infty} \left(\dfrac{\mathrm{d}n}{\mathrm{d}Q_{\mathrm{pad}}} \right) \mathrm{d}Q_{\mathrm{pad}}}{\int\limits_{0}^{\infty} \left(\dfrac{\mathrm{d}n}{\mathrm{d}Q_{\mathrm{pad}}} \right) \mathrm{d}Q_{\mathrm{pad}}} \tag{4.24}$$

with T_{pad} being the threshold values.

Figure 4.27 shows the typical charge distribution on a MWPC pad. The integrated and normalized charge distribution yields the relation between threshold and efficiency, from which the threshold for any given efficiency can be deduced.

At the end of the job, a new CDM2 bank is created. Rerunning the program over the same or a different data–set, using the new created CDM2 bank as input yields control plots, telling the quality of the tuning parameters deduced. Some of these plots can be seen in fig 4.28 to 4.30.

The tuning of the border regions since only the central region of CIP can be reached using CJC tracks has to be handled differently. One could in principle use tracks from the forward tracker. In practice these are so far not well understood and many technical problems are to be expected. On the other hand, flat tracks are more or less always efficient as it is apparent in figure 4.23. Therefore the threshold values determined from the central region of CIP are used for an estimate of the threshold values near the edges of CIP. This is done for each φ–segment separately excluding problematic channels (very low or very high threshold with respect to other channels). Dead channels of CIP outside the central region have to be recognized from the global hitmap (see fig 4.14) and can be removed afterwards via an arbitrary negative threshold value assigned to them.

The plots showing the pad efficiencies for both, data and simulation demonstrate only that the program ZVTXTUNE2 works properly. These quantities are expected to match.
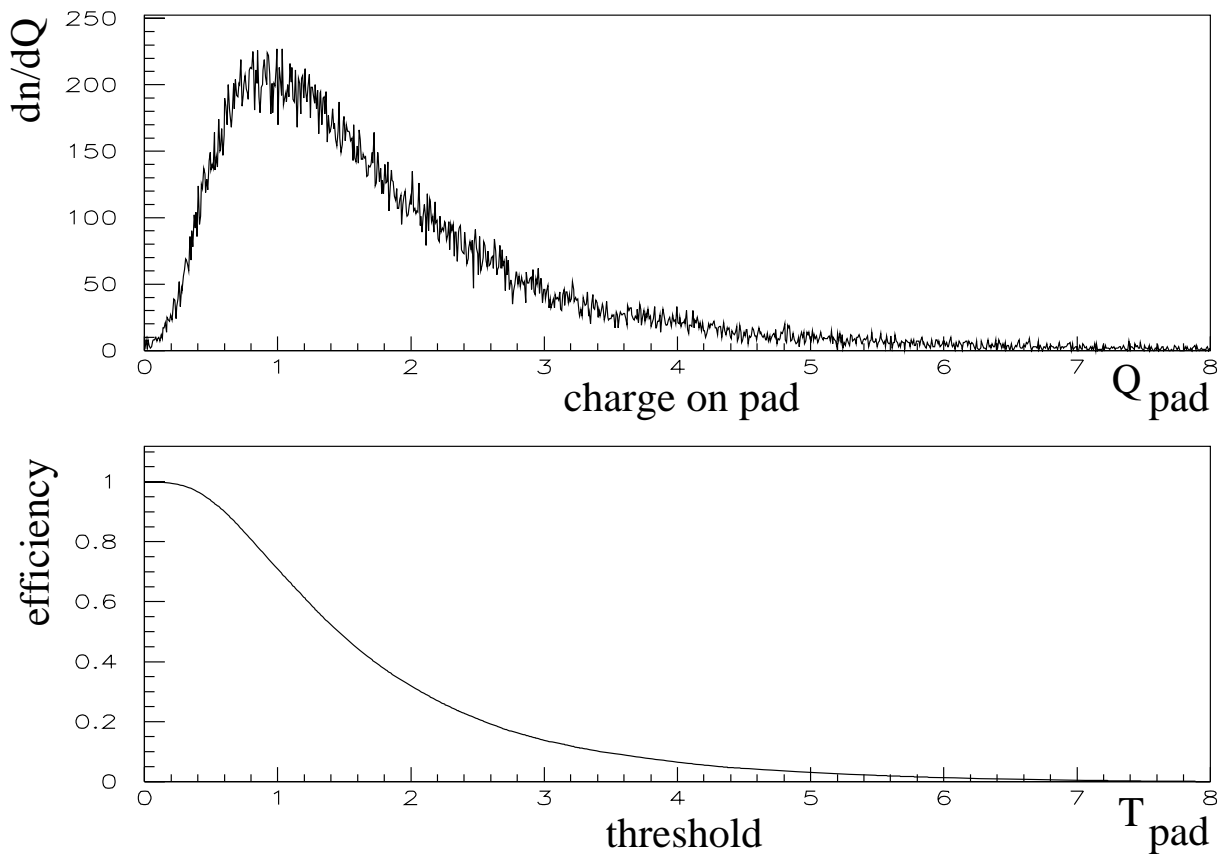
Figure 4.27: Charge distribution on a MWPC pad. Out of the integrated and normalized charge distribution, the relation between efficiency and threshold is obtained.

More relevant information on the quality of the tuning parameters can be derived from the efficiency plots in function of different track parameters (see fig 4.30).

As can be seen from figure 4.30, the efficiency as function of the polar angle ϑ is lower for tracks crossing perpendicular the MWPC layer planes. COP 0 looks different because a dead cable removes channels which are reached by flat tracks only. The simulation describes the data nicely.

The strange shape of the efficiency as function of d_{ca} for COP 1 is correctly described by the simulation and can be explained if one considers the correlation of d_{ca} with the azimuthal angle φ, which arises from the shift of the nominal interaction point in the r–φ–plane by 7 mm from the nominal H1 interaction point. Positive values of d_{ca} favor azimuthal angles φ from 180° to 360°, i.e. the sector which contains the broken anode wire of COP 1 and is therefore less efficient.

A critical quantity to look at is the average number of active pads per track crossing
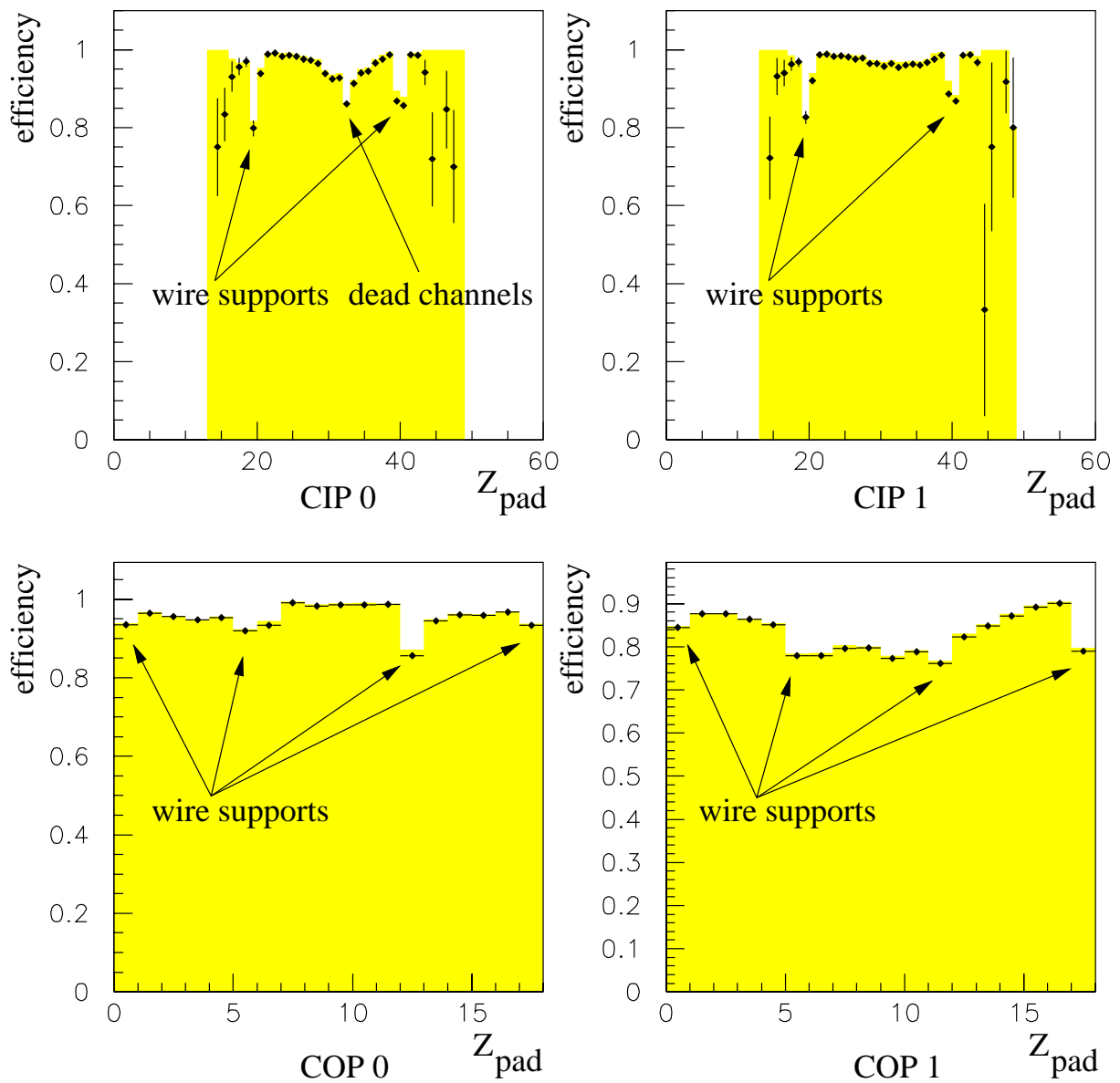
Figure 4.28: Tuned MWPC efficiencies. The measured efficiency from data is shown using bold symbols with error bars. The shaded histogram represents the measurement of the efficiency from simulation. Only the center region of CIP can be reached using CJC tracks.

the chamber plane. It is plotted against the azimuthal angle φ and the polar angle ϑ for data as well as for different simulations using various values for the active gap (see fig 4.31–4.32).

Typically more than one pad fires when a track crosses a chamber, which is also described by the simulation, but the absolute value is systematically a few % lower in simulation
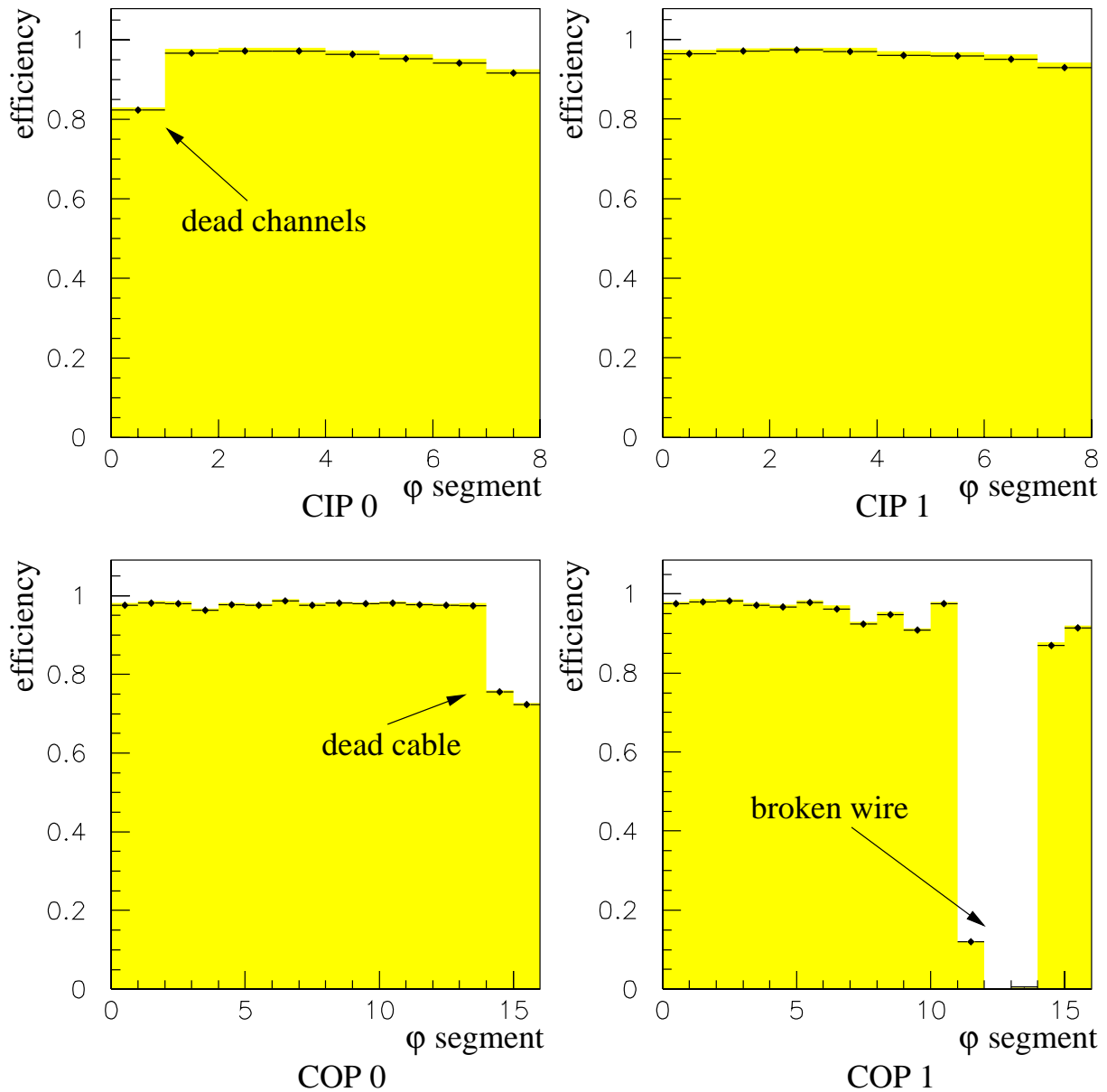
Figure 4.29: Tuned MWPC efficiencies. The measured efficiency from data is shown using bold symbols with error bars. The shaded histogram represents the measurement of the efficiency from simulation.

than in data. The shape of the simulation prediction follows the data reasonably well. The treatment of the stochastic noise seems to be adequate to describe the gross features of the chambers, but there are still regions (especially COP 0) which can not be described satisfactorily. We ascribe this to a high noise level in certain regions of the chambers, which is usually not sufficient to activate pads. When a track passes such regions deposited and
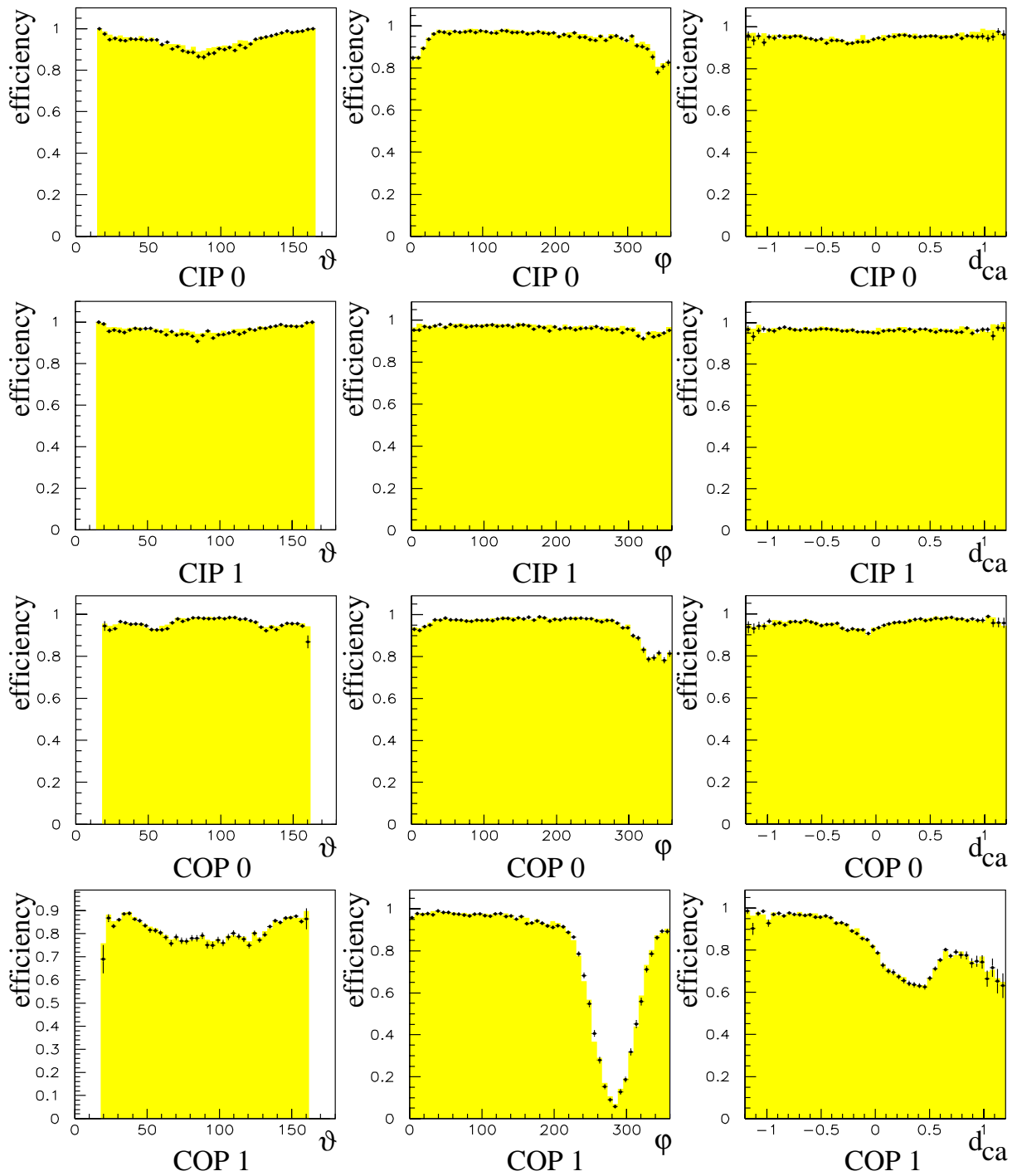
Figure 4.30: Tuned MWPC efficiencies as function of various track parameters. The measured efficiency from data is shown using bold symbols with error bars. The shaded histogram represents the measurement of the efficiency from simulation.
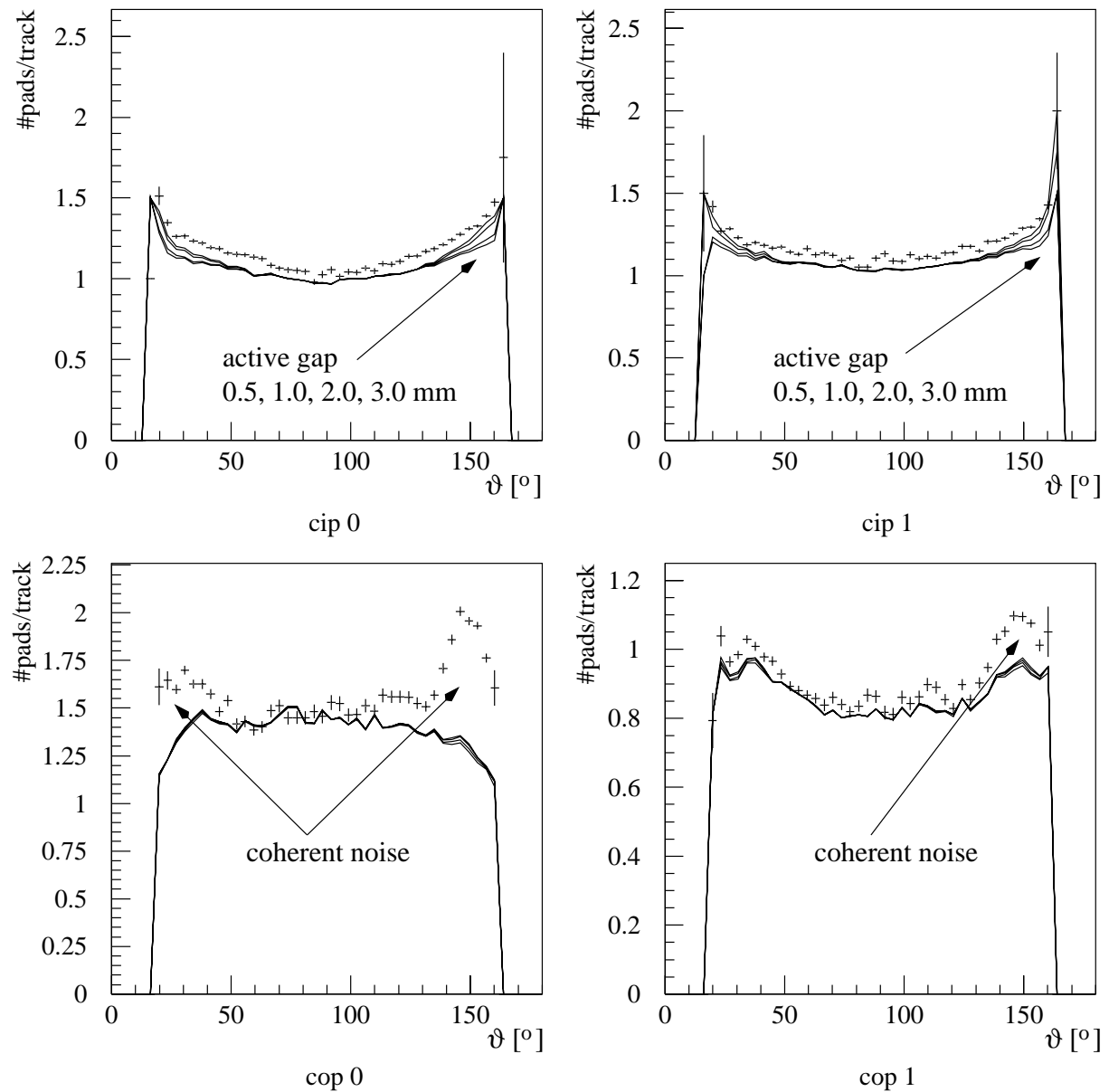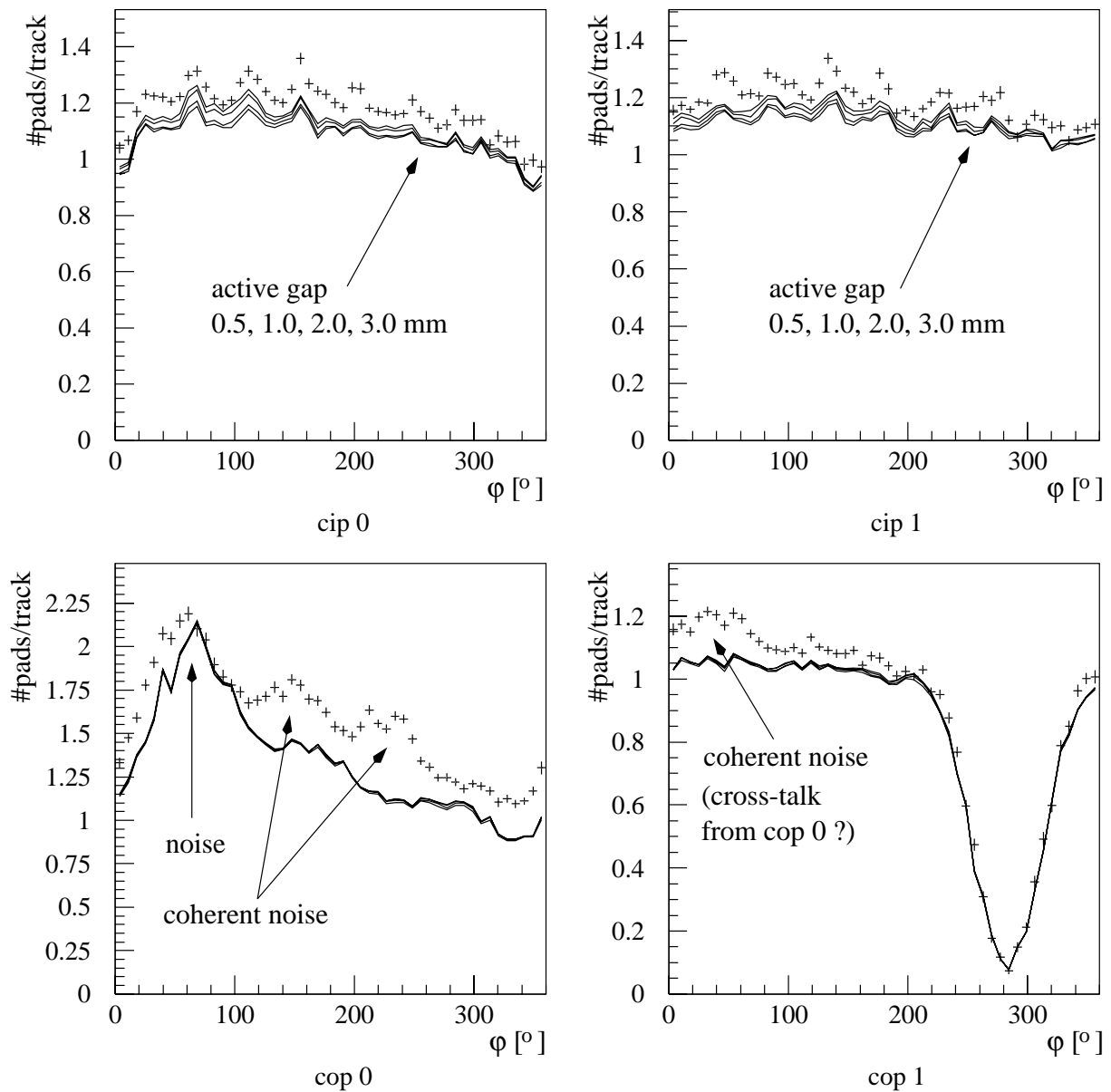
Figure 4.31: Average number of active pads vs. polar angle ϑ of track. Data points are shown as crosses, whereas the simulated predictions for various values for the active gap are shown as straight lines.

amplified charge combines with the noise and more pads are activated than expected. This is referred to as *coherent noise* within these plots.

As can be seen from figure 4.31, the rôle of the active gap is sizeable for flat tracks only and it controls the number of active pads per track. For CIP, a value of 3 mm for the active gap describes the data the best, which means that the full gap width has to be

Figure 4.32: Average number of active pads vs. azimuthal angle φ of track. Data points are shown as crosses, whereas the simulated predictions for various values for the active gap are shown as straight lines.

ascribed to the active gap. For COP, the rôle of the active gap is not as manifest, since the pad–size is too large to be sensitive on small changes of the (calculated) width of the charge distribution.

The critical plots to check the quality of the tuned digitization parameters for the z–Vertex trigger are of course the z–Vertex ray efficiencies. These are shown in figure 4.33. All

acceptances are reasonably described, even when the average number of active pads per track is not described to full satisfaction.

As a remarkable success, the number of active rays per track is correctly described, including the higher probability to find four rays compared to three rays.
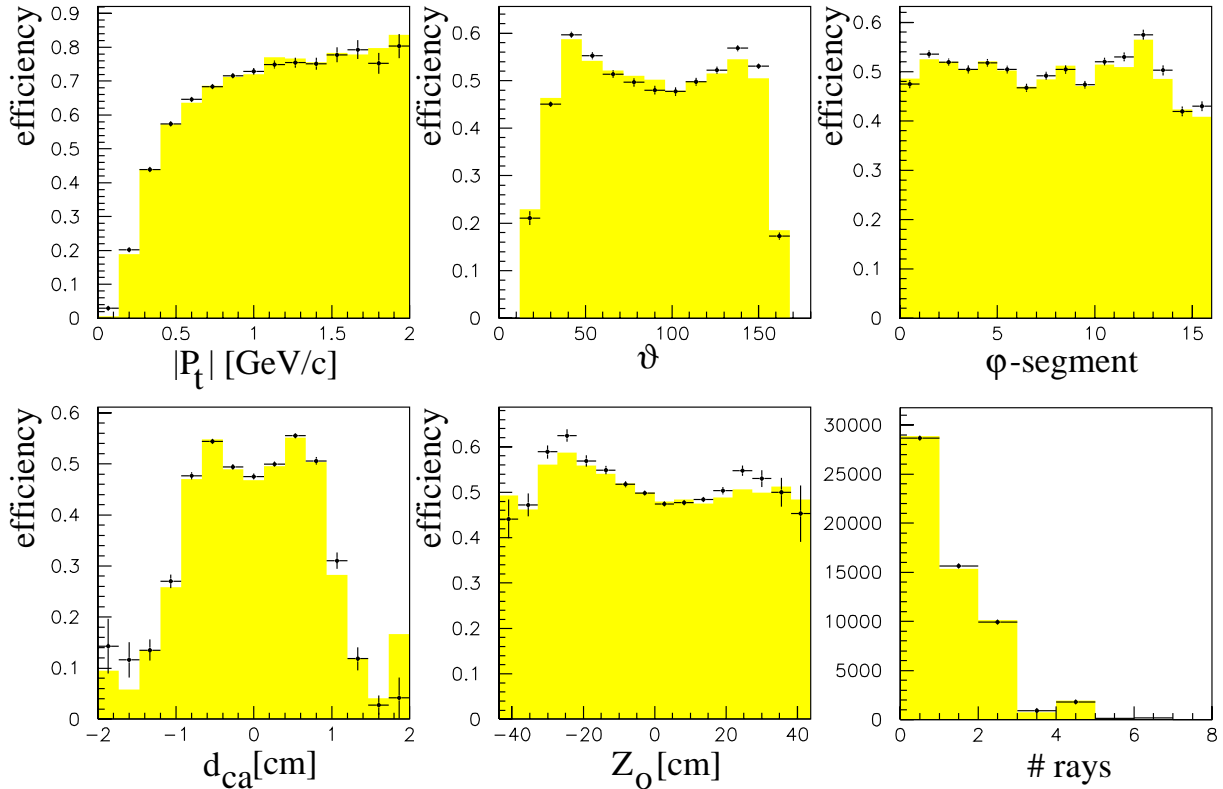

Figure 4.33: The tuned MWPC parameters fix the acceptance of single tracks for the z–Vertex trigger. The measured efficiency from data is shown using bold symbols with error bars. The shaded histogram represents the measurement of the efficiency from simulation.

4.7.4 Possible Improvements

For a possible improvement of the quality and consequent expansion of complexity of the Monte–Carlo digitization scheme for the MWPCs, the following points could be considered:

- The efficiency of CIP pads is only determined in its center region. Using high quality tracks from the forward tracker would cover the forward region of CIP and a better description of the actual number of active pads per track would be obtained. (The efficiency of CIP for forward tracks is anyhow close to one, such that no improvement for this number can be expected.) The same is true for the

backward region of CIP. With help of the backward driftchamber BDC which was installed 1995 (this analysis is performed using 1994 data only) an evaluation of the CIP efficiency in the backward region is feasible. These backward pads are not used for the z–Vertex trigger (cf. fig 4.19) but they are relevant for the CIP–backward veto trigger.

- The current digitization scheme assumes that all electrons from the total ionization drift towards exactly one anode wire, located such, that the wire crosses exactly the track in the middle of the gaseous volume of the chamber. Especially for low transverse momenta $p_\perp$ and for flat polar angles more than one anode wire should be considered. With a full width of the gap of 6 mm and an anode wire spacing of 2 mm for CIP up to $3 - 4$ anode wires are expected to accumulate charge. This leads to a more expanded charge distribution and more pads are expected to be activated per track. Equation 4.23 therefore, has to be rewritten as follows:

$$Q_{\text{pad}} \sim \frac{1}{|\cos\vartheta|} \frac{\mathrm{d}E}{\mathrm{d}s} \iint\limits_{\text{pad}} \sum_i \int\limits_{-D_i}^{D_i} \sigma_i(x, z - z_i') \,\mathrm{d}z_i' \,\mathrm{d}x \,\mathrm{d}z$$

where the sum has to be taken over all anode wires i with non–vanishing charge. The distribution of the charge densities σ_i has to be evaluated per anode wire.

- The current digitization scheme assumes a homogeneous charge density distribution along the anode wire. The intercepted pad then accumulates most of the induced charge and all nearest neighbors get less. This is not the case for real data, as can be seen from figure 4.34. Here, the efficiency of CIP and COP is plotted versus the polar angle ϑ of the track for those tracks only, where the hit pad was *not* active. In the current simulation scheme a non–vanishing efficiency in these plots is only then possible, when the track seems to point to the pad hit, but in reality, due to inaccurate track parameters, points to a neighboring pad, which then gets the most charge and is activated. For tracks crossing the chamber plane at right angles the simulation is able to describe the data, which indicates that the errors of the track parameters are correctly assumed. For flat tracks, the simulation completely fails to describe the data. Very flat tracks get here an efficiency of close to one, whereas the simulated efficiency (error matrix determined from CIZ and COZ linked high quality tracks) shows a flat distribution. This effect that the primary ionization process does not necessarily lead to a uniform distribution of charge along the anode wire. It can be non–uniform and does not have to peak in its center. This could be taken into account by taking several, independently Landau–distributed values for dE/dx, each valid only for a short sub–range along the trajectory rather than only one value for the entire track. For flat tracks, a large probability exists that the peak
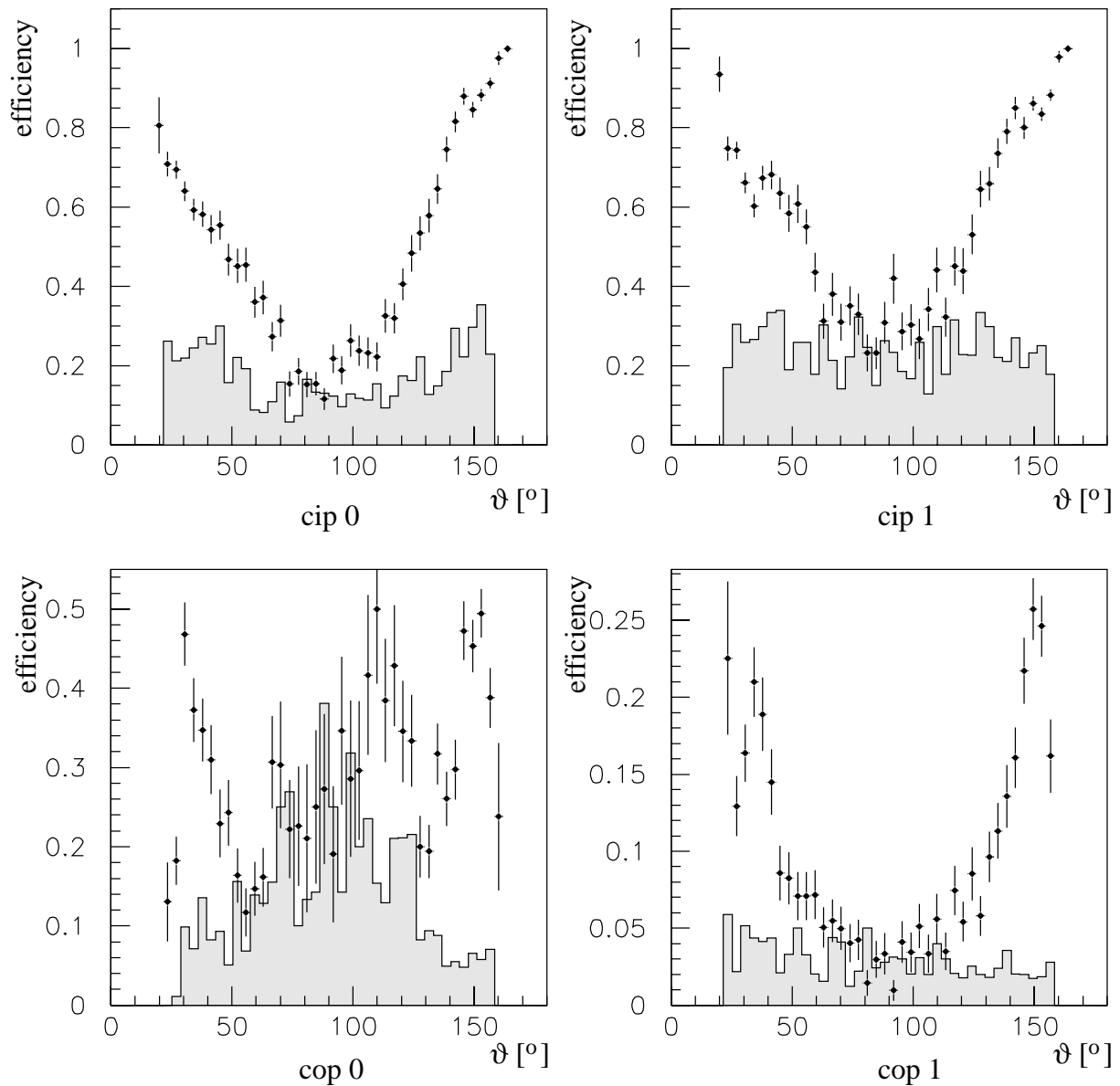
Figure 4.34: MWPC efficiency vs. ϑ determined from those tracks, where the intercepted pad was *not* active. The data are shown with crosses and the simulation is represented by the shaded histogram.

of the charge distribution is no longer inside the area of the intercepted pad. For CIP (COP), 7% (2%) of all tracks produce an inefficient center pad with at least one neighbor pad being active.

- Only one parameter for the (active) gap is ascribed per chamber. In reality, the MWPCs are not completely cylindrical with a constant gap width over the full azimuth, but a more egg–like shape has to be considered. This can be seen from

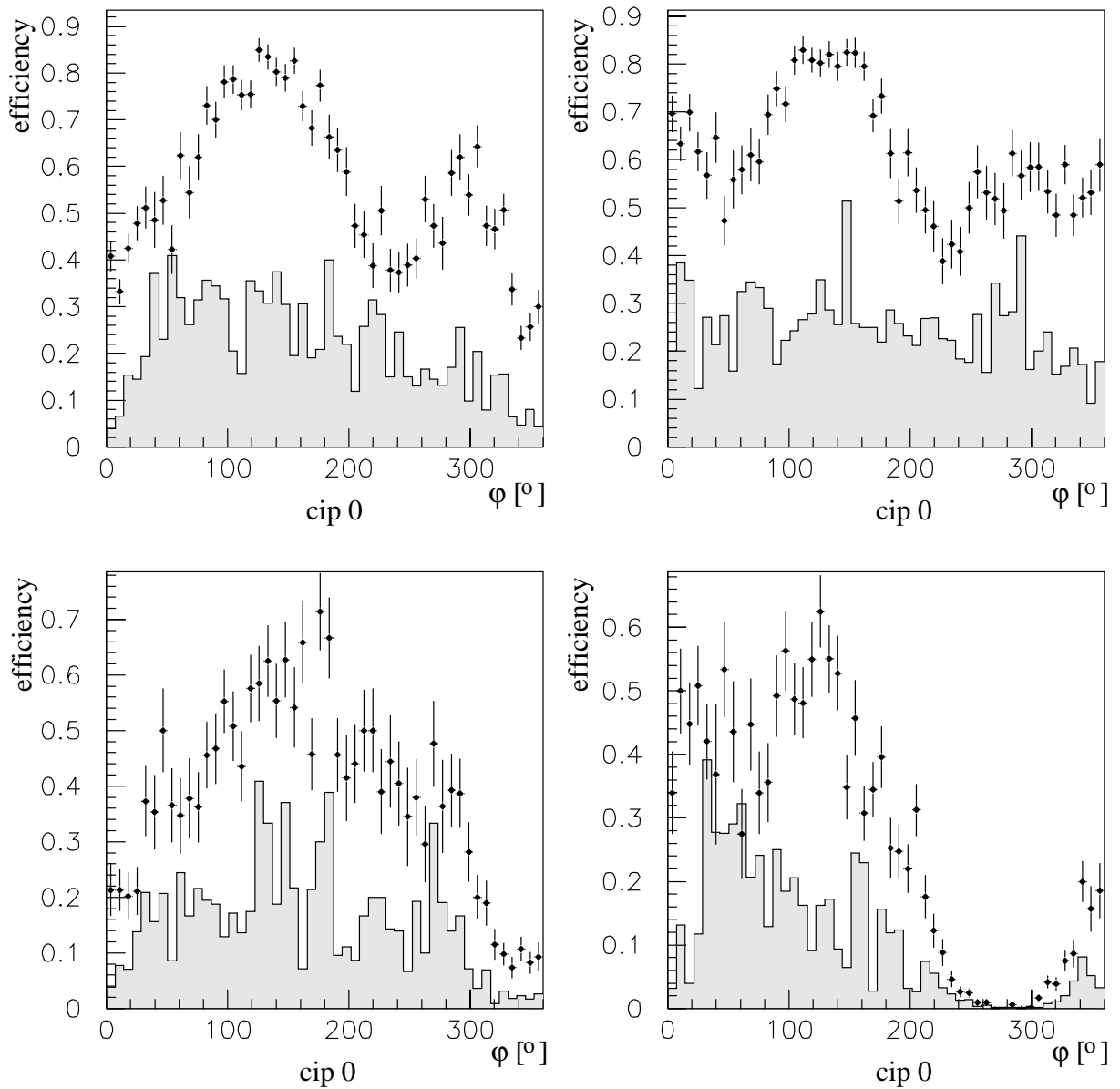a similar plot as the one above, where the efficiency, evaluated from those tracks

Figure 4.35: MWPC efficiency vs. φ determined from those tracks, where the hit pad was *not* active. The data is shown with crosses and the simulation is represented by the shaded histogram.

only where the hitten pad is *not* active, as function of the azimuthal angle φ, is shown (see fig 4.35). CIP data shows a much evaluated structure with peaks at 130° and 310° (separated by 180°). In these regions, the (active) gap is large, as the width of the charge distribution has to be larger to effectively become efficient in these plots. Around 0° an additional low efficient region is seen. This leads to a

possible geometrical interpretation, where the cylindrical double layers of CIP 0 and
CIP 1 are squeezed to elliptical shapes, with an azimuthal angle of the squeeze axis
being along 220º. Anyhow, several parameters for the (active) gap, each valid for a
sub–range in φ only, could describe even these structures (even if above geometrical
interpretation does not hold).

Chapter 5

Measurement of the $\sigma_{\mathrm{tot}}^{\gamma\mathrm{p}}$ cross section

The data used for the measurement of the total photoproduction cross section $\sigma_{\mathrm{tot}}^{\gamma p}$ was collected in a short dedicated run close to the end of the data taking period 1994 at H1. 153 colliding bunches of 27.6 GeV positrons and 820 GeV protons circulated the HERA machine. In addition, for an estimation of beam induced background, 32 pilot bunches (17 proton bunches and 15 positron bunches) had no colliding counterpart.

Since an important part of the total cross section measurements is the break up into the different sub processes already mentioned in section 1.7, we first discuss the typical topology. The characteristic distribution of the reaction products allows to identify the process, but also leads to quite different trigger probabilities. A proper determination of these trigger efficiencies is therefore of utmost importance. This is one of the reasons, why we went to such details in our description of the z–Vertex trigger performance in the preceding chapter.

5.1 Topology of γp–reactions

The total γp–cross section has substantial contributions from diffractive photon–proton reactions. The properties of diffractive photon–proton reactions are similar to those in diffractive hadronic events, therefore, the language of hadronic physics can be adapted to the photon–proton case. The following diffractive processes are distinguished in photoproduction:

- Elastic vector meson production (EL) $\gamma + p \rightarrow V + p$, where V stands for one of the vector mesons ρ^0, ω and ϕ. The true electro–magnetic elastic reaction $\gamma + p \rightarrow \gamma + p$ has a very low cross section and is neglected [11].

- Single photon diffractive dissociation (GD) $\gamma + p \rightarrow X + p$, where the photon diffractively dissociates into a hadronic state X and the photon stays intact.

- Single proton diffractive dissociation (PD) $\gamma + p \rightarrow V + X$, where the proton fragments into a hadronic state X and a vector meson is produced in photon direction.

- Double diffractive dissociation (DD) $\gamma + p \rightarrow X_1 + X_2$, where both photon and proton dissociate.

All processes $\gamma + p \rightarrow X$ not belonging to the contributions defined above are called non–diffractive (ND).

Since diffractive reactions involve no exchange of quantum numbers between the incident particles, their final state topology is radically different from the bulk of non–diffractive events. Large rapidity intervals between the incident particles (gaps with no hadrons) show up under pomeron exchange, since there is no color flow with corresponding hadronisation.

The different topologies of above described event–classes are depicted in fig 5.1–5.5. The escaping positron, which was the source of the quasi–real photon, can be detected in the electron tagger, located 33 m away of the nominal interaction point.
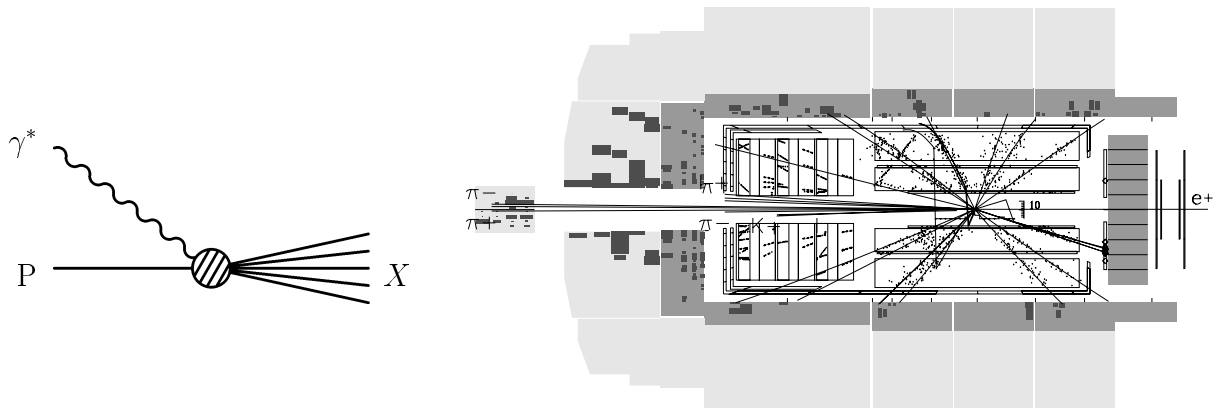

Figure 5.1: Non–diffractive γp–event (ND). All gaps in the hadronic flow are arbitrary.

5.2   Event selection

The basic requirement to tag quasi–real photoproduction events at H1 is the detection of a scattered positron (electron) under a very small scattering angle ϑ' ($\vartheta' = \pi - \vartheta$). A positron (electron) detected in the electron tagger (ET) guarantees for a very low $Q^2 < 10^{-2}$ GeV^2 and was therefore used as a first level trigger for a selection of photoproduction events.
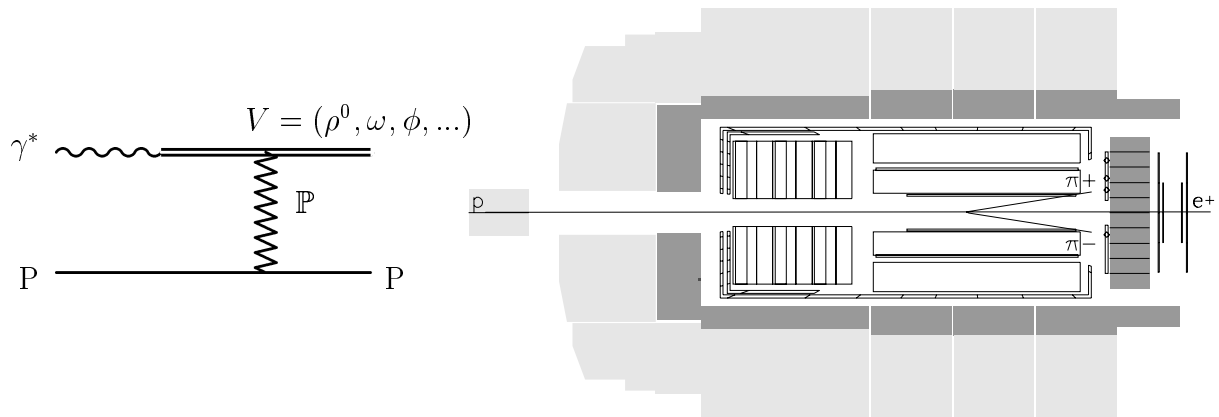
Figure 5.2: Elastic vector meson production (EL). The short living vector meson decays into a hadronic final state. Here, $V = \rho^0 \to \pi^+ + \pi^-$.
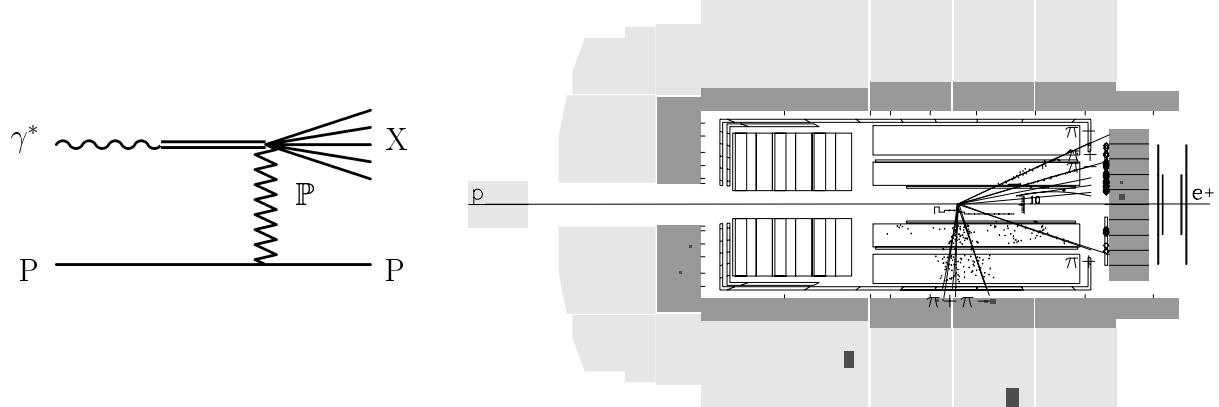

Figure 5.3: Single photon diffractive dissociation (GD). The photon dissociates, whereas the proton stays intact. No activity is seen in the forward part of the detector.
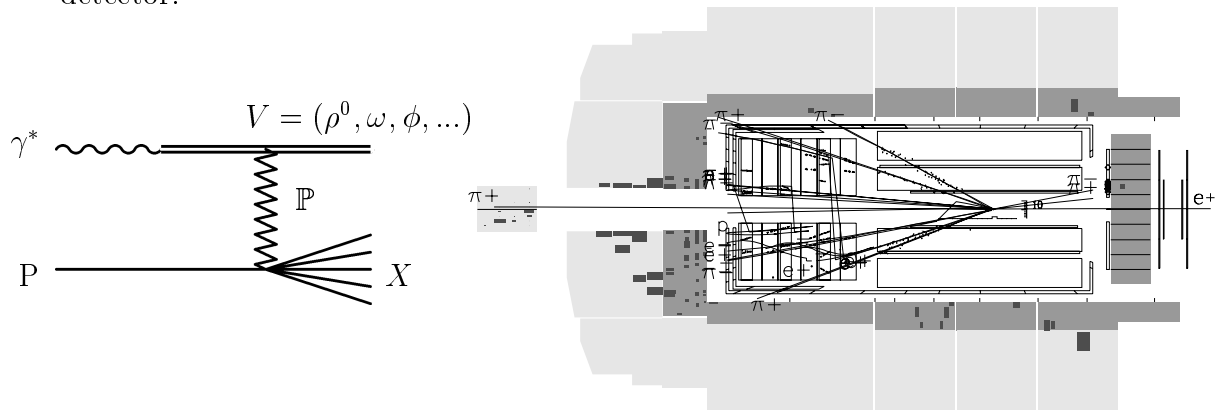

Figure 5.4: Single proton diffractive dissociation (PD). The proton dissociates, whereas the vector meson gets no diffractive excitation. The short living vector meson decays into its hadronic final state. Here, $V = \rho^0 \to \pi^+ + \pi^-$.
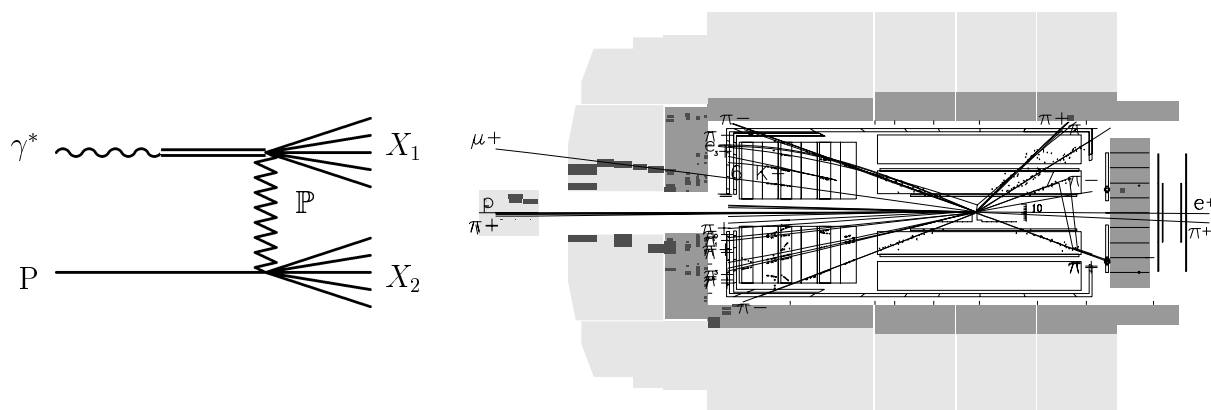
Figure 5.5: Double diffractive dissociation (DD). Both, the proton and the vector meson dissociate. A rapidity gap is seen in the central area of the H1 detector.

An additional veto in the photon–detector (PD) substantially reduces the size of QED radiative corrections and suppresses accidental coincidences of Bethe–Heitler ($ep \rightarrow ep\gamma$) events with proton induced background. (fig 3.6 shows the locations of both ET and PD.)

The electron tagger performs a double function. It tags γp–events and provides a measurement of the scaling variable y from which the center–of–mass energy of the photon–proton sub process is obtained. ($W^2_{\gamma p} = ys$, cf. eq. (1.34)).

Two additional and independent trigger conditions were used to collect three different sets of data samples. The first condition required the z–Vertex trigger with at least one *ray* present, i.e. the z–Vertex–T_0 condition (cf. section 4.3). The second condition required the ToF–trigger (cf. section 3.5) which asks for a signal from the scintillator planes located in back of the BEMC within the time–interval expected for ep–interactions. In the photoproduction case, the ToF–trigger is sensitive to hadrons originating from the photon remnant (see fig 5.1 to 5.5).

Two of these data samples were taken with the nominal interaction point for ep collisions located at $\bar{z} = +4$ cm, a third sample was taken with the nominal interaction vertex shifted along the z–axis towards $\bar{z} = +71$ cm. For the shifted vertex sample, only the ToF–trigger condition was used, since the z–Vertex trigger looses its acceptance for real tracks coming from upstream and only random coincidences of MWPC pads from different tracks would enable rays in the trigger. (It would be nearly impossible to derive a trigger efficiency for such events.) The acceptance of hadrons from the photon remnant in the ToF–planes is significantly higher for the shifted vertex sample with respect to the nominal vertex sample, as particles emerging under flat angles no-longer escape detection through the beam hole due to their longer base line.

Table 5.1 gives an overview of the event selection.

For triggered events, the fractional energy of the photon, as measured by the electron

interaction point	$\bar{z} = 4$ cm	$\bar{z} = 71$ cm	$\bar{z} = 4$ cm
trigger	Etag && z–Vertex–T_0 (central ray)	Etag && ToF	
event selection	$Z_{0,\,\mathrm{track}} > -100$ cm		
	energy in photon detector < 2 GeV		
	$0.3 < y < 0.7$		
	$|Z_{\mathrm{vtx}} - 4\text{ cm}| < 30$ cm	$|Z_{\mathrm{vtx}} - 71\text{ cm}| < 30$ cm	$|Z_{\mathrm{vtx}} - 4\text{ cm}| < 30$ cm
	at least one CJC track fitted to vertex	either CJC track or BPC hit	
$\mathcal{L}$uminosity	23.8 ± 0.3 nb^{-1}	24.0 ± 1.3 nb^{-1}	23.8 ± 0.3 nb^{-1}
# events	19450 ± 145	18560 ± 220	18038 ± 195
background			
e–induced	0%	4%	8%
p–induced	3%	0%	0%
other	0%	0.2%	1%

Table 5.1: Event selection for the three data samples.

tagger, is required to be within the interval $0.3 < y < 0.7$. Only within this range the acceptance of the electron tagger is known to high accuracy. This limits the accessible center–of–mass energy $W_{\gamma p}$ of the photon proton sub system to $W_{\gamma p} \in [163, 249]$ GeV, with a mean value of $\langle W_{\gamma p} \rangle = 200$ GeV. Additional requirements are either a reconstructed and vertex fitted CJC track or, only for the ToF triggered sample, at least one hit from the hadronic photon remnant in the BPC. The event vertex, which is reconstructed from CJC tracks, is required to be within 30 cm from the mean z–position of the interaction point.

For the sample triggered by the z–Vertex trigger, the trigger condition was tightened in demanding at least one trigger ray present, to which only CIP and COP cathode pads contribute, because for these events the z–Vertex–T_0 condition is understood very well, as we have shown in the previous chapter.

5.3   Background

The main source of background in the data samples taken with the TOF trigger are positron gas and positron beam–wall interactions. These contributions are easily estimated using pilot bunch data and, after correcting the different intensities of pilot bunch and colliding bunch data, results to be 8% (4%) for the nominal (shifted) interaction vertex sample. The contribution of positron pilot events in the z–Vertex triggered data sample is negligible.

More specific is the estimation of the proton induced background, as the trigger condition explicitly asks for an electron in the tagger, and no proton only event would fulfill such a requirement. Still, protons are a source of background and the contribution has to be estimated in a different way. Taking ep data with no further requirement but a tagged positron (etag monitor trigger events) yields in a first approximation only background data. The shape of the y–spectrum from such monitor data can be compared with the effective y–spectrum for real γp–candidates (see fig 5.6). The ratio of the background in the low y–region to the γp signal, i.e. the monitor sample normalized to the full γp sample near $y = 0.15$ gives an estimate of the contamination due to proton induced background. This method gives at least an upper limit for this contamination. The shape of the y–distribution from monitor data is very sensitive on the actual beam conditions and therefore, the proton induced background estimate was done in several steps, for small fractions of the final event sample only. Negligible amount of proton induced background was found in the TOF triggered samples and a value of 3% contamination resulted in the z–Vertex triggered sample.
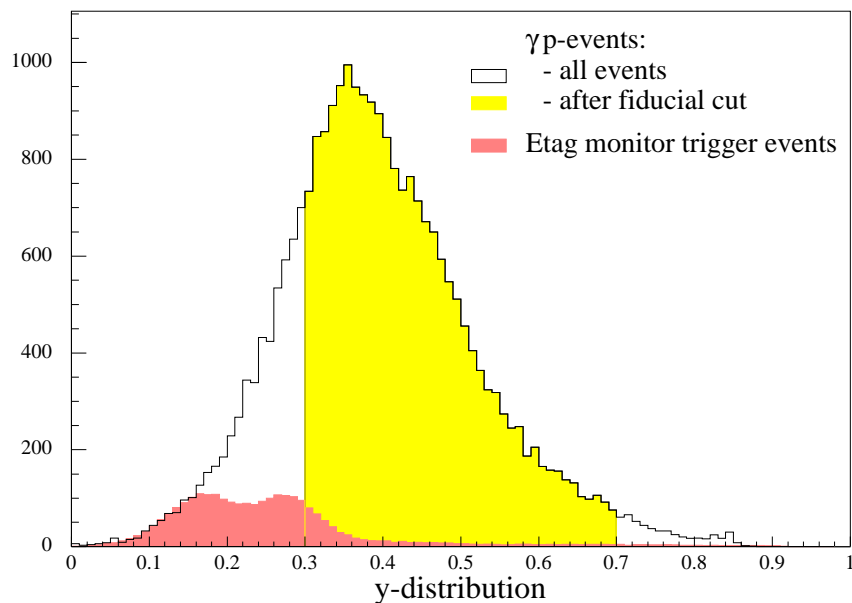

Figure 5.6: Estimation of proton induced background.

5.4 Monte–Carlo models for photoproduction

In principle a measurement of the total cross section is independent of theoretical models for the process. The measurement is of course performed to check the model predictions. However, since our apparatus does not cover the complete solid angle for the final reaction products, many detector parts have energy dependent thresholds and response functions and also our trigger selection produces further bias, Monte–Carlo models are already needed to estimate that part of the cross section, which escapes detection, i.e. we need Monte–Carlo models to estimate our acceptance.

In order to reduce or at least assess the model dependences of our calculations we use two different Monte–Carlo programs PYTHIA [67] and PHOJET [68]. Both programs describe all diffractive and non–diffractive contributions to the total cross section, but start from a completely different ansatz.

PYTHIA describes non–diffractive events using the multiple interaction model [73]. A hard scattering scale $p_{\perp \mathrm{min}} = 1.45$ GeV/c is introduced in line with the lower limit of the accessible range for a pQCD ansatz. Since photon and proton are thought to contain several partons more than one hard sub process is possible. Since these are essentially independent of each other, the number of interactions per collision follows a Poisson distribution. For soft non–diffractive events, an exchange of a soft gluon between the interacting particles is assumed.

PHOJET relies on a parameterization of the photon–proton scattering amplitude in the eikonal approximation using the dual parton model (DPM) [74] for a description of non–diffractive (multi-particle final state) events. Soft and hard sub processes are connected by an unitarization scheme.

Diffractive events are generated in both PYTHIA and PHOJET using the t–dependence $\frac{\mathrm{d}\sigma}{\mathrm{d}t} \sim e^{Bt}$, which is typical for hadronic physics (cf. section 1.7). For elastic vector meson production, the B–slope parameter is taken to be $B \approx 11\,\mathrm{GeV}^{-2}$. Since quasi–real photons are transversely polarized, the VMD vector meson (ρ, ω or ϕ) shows the same polarization (s–channel helicity conservation (SCHC) [11]) and therefore their decay products follow a typical angular distribution (e.g. $\rho^0 \rightarrow \pi^+\pi^-$: the distribution of the decay angle ϑ of the pions with respect to the direction of motion of the ρ^0 follows $\sim \sin^2 \vartheta$).

For single– and double diffractive events, PYTHIA takes the slope parameter B to be half of that for elastic events [29]. PHOJET assumes a mass dependent slope parameter, i.e. $B \approx 11\,\mathrm{GeV}^{-2}$ at $M_X = m_{\rho^0}$ and decreasing for higher M_X.

PHOJET uses a modified M_X dependence of the diffractive mass which corrects for the mass of the incoming vector meson and demands an effective, diffractive mass of at least two pion masses, whereas PYTHIA follows the conventional description (cf.

equations (1.51 ff.)):

$$\frac{\mathrm{d}^2\sigma}{\mathrm{d}M_X^2\,\mathrm{d}t} \sim \frac{1}{M_X^2}\,e^{Bt} \qquad \text{with} \quad M_X > M_{\mathrm{in}} + 0.2 \text{ GeV} \qquad \text{PYTHIA} \qquad (5.1)$$

and

$$\frac{\mathrm{d}^2\sigma}{\mathrm{d}M_X^2\,\mathrm{d}t} \sim \frac{1}{M_X^2 - M_{\mathrm{in}}^2}\,e^{Bt} \qquad \text{with} \quad M_X > M_{\mathrm{in}} + 2m_\pi \qquad \text{PHOJET} \qquad (5.2)$$

with M_{in} being the mass of the incoming vector meson (e.g. $M_{\mathrm{in}} = m_{\rho^0}$) or the proton mass for diffraction dissociation of the photon or the proton, respectively.

Further differences in the generation of diffractive events between PHOJET and PYTHIA lie in the treatment of resonant states within the diffractive system. PYTHIA does not explicitly describe single resonant states, but describes them in an average manner, whereas PHOJET explicitly allows for generation of excited particle states in the diffractive system. Applying the rules of the dual parton model for photon–proton scattering to pomeron–proton and pomeron–photon scattering, with the pomeron treated like an ordinary virtual meson, leads to additional diffractive multi–particle final states in PHOJET. Soft and hard diffractive scattering events are generated according to cross sections given by Regge phenomenology and QCD parton model respectively.

The generated events from both PYTHIA and PHOJET are fed into the H1 detector simulation program H1SIM and subsequently into the same reconstruction program H1REC and analysis chain as real ep–data.

The interaction point along the beam line for the generated events is smeared to match the measure z–position of the reconstructed event vertex (see fig 5.7).

A comparison of simulated distributions for the multiplicity n_{ch}, the transverse momentum $p_\perp$ and the pseudo–rapidity $\eta = -\ln(\tan\frac{\vartheta}{2})$ of charged tracks with the measured ones in the z–Vertex triggered data sample is shown in figure 5.7. The agreement between data and and simulation demonstrates that the event generators reproduce the main features seen in data. However, the data seem to imply a less strongly forward peaked angular distribution than predicted by the models.

5.5   Cross section calculation

The differential ep cross section is related to the total number of observed events by following expression:

$$\frac{\mathrm{d}^2N}{\mathrm{d}y\,\mathrm{d}Q^2} = \mathcal{L} \cdot \epsilon(y) \cdot A(y, Q^2) \cdot \frac{\mathrm{d}^2\sigma^{ep}}{\mathrm{d}y\,\mathrm{d}Q^2} \qquad (5.3)$$
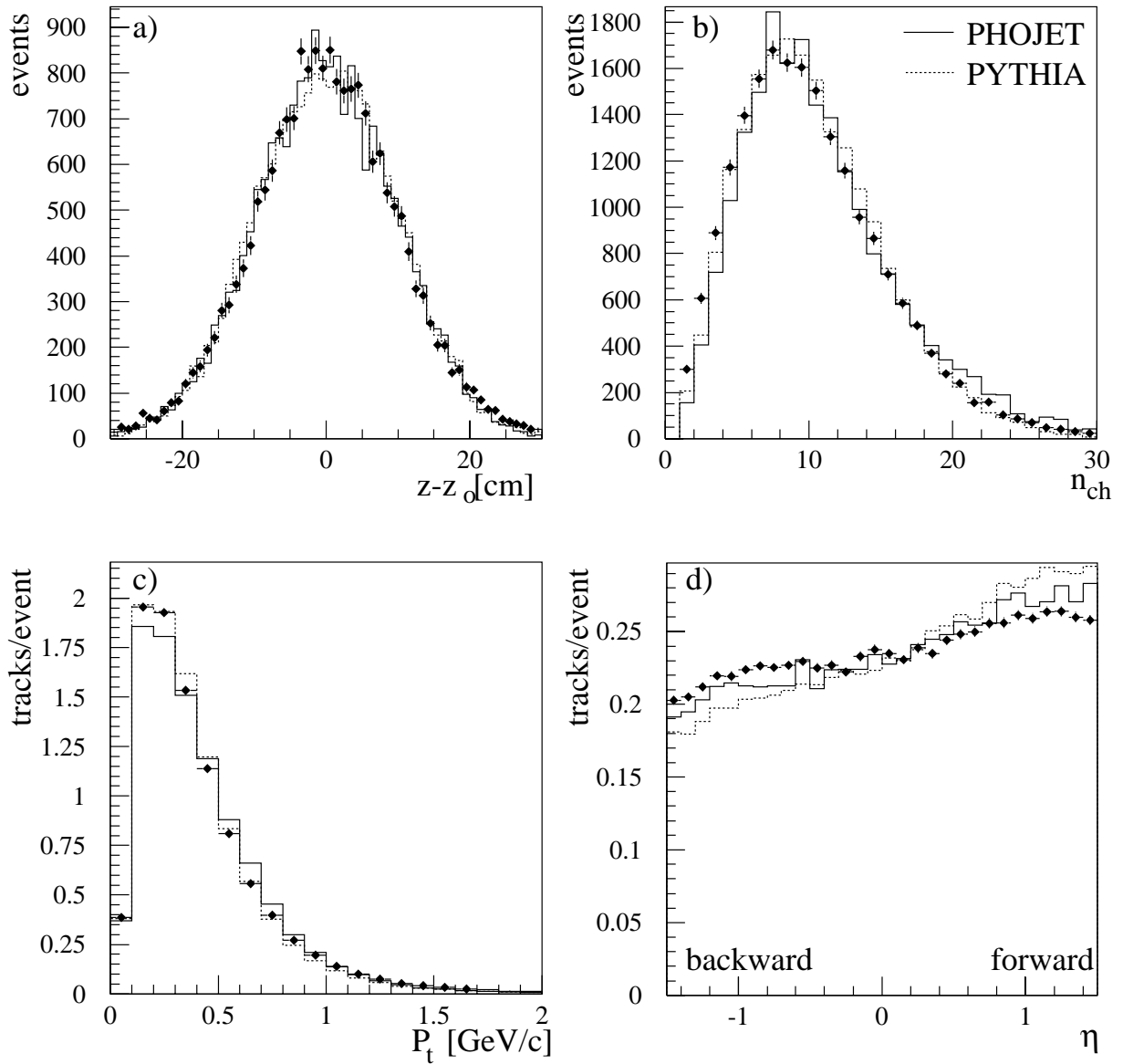
Figure 5.7: Comparison of z–Vertex triggered data (points) with Monte–Carlo simulation using PHOJET (full line) and PYTHIA (dotted line).

a) z–position of the reconstructed event vertex with respect to the nominal H1 interaction point.

b,c) multiplicity n_{ch} and transverse momentum $p_{\perp}$ of charged driftchamber tracks.

d) pseudo–rapidity η of charged driftchamber tracks. The data seem to imply a less strongly forward peaked angular distribution than predicted by the models.

with $\mathcal{L}$ being the total integrated luminosity, $\epsilon(y)$ being the efficiency of the z–Vertex (ToF) trigger and selection criteria, and $A(y, Q^2)$ being the acceptance of the electron tagger. The efficiency ϵ is assumed to dependent only on y, since Q^2 is always small for quasi–real photoproduction. Integration over y and Q^2 yields a relation between observed events and total photoproduction cross section:

$$N = \mathcal{L} \int_{y_{\min}}^{y_{\max}} \int_{Q^2_{\min}}^{Q^2_{\max}} \epsilon(y) \cdot A(y, Q^2) \cdot \sigma^{\gamma p}_{\mathrm{tot}}(ys) \cdot F(y, Q^2) \, \mathrm{d}y \, \mathrm{d}Q^2 \qquad (5.4)$$

where the differential ep cross section has been replaced with photoproduction cross section times photon–flux $F(y, Q^2)$. The photon–flux can be taken from equation (1.36) which improves the usual Weizsäcker–Williams approximation by 6–7%.

$$F(y, Q^2) = \frac{\alpha}{2\pi} \frac{1}{Q^2} \left(\frac{(1 - (1 - y)^2)}{y} - \frac{2(1 - y)}{y} \frac{Q^2_{\min}}{Q^2} \right) \qquad (5.5)$$

Following averaged values are introduced to handle the integration over y and Q^2:

$$\sigma^{\gamma p}_{\mathrm{tot}} = \frac{\iint \epsilon(y) \, A(y, Q^2) \, \sigma^{\gamma p}_{\mathrm{tot}}(ys) \, F(y, Q^2) \, \mathrm{d}y \, \mathrm{d}Q^2}{\iint \epsilon(y) \, A(y, Q^2) \, F(y, Q^2) \, \mathrm{d}y \, \mathrm{d}Q^2} \qquad (5.6)$$

$$A(y) = \frac{\int A(y, Q^2) \, F(y, Q^2) \, \mathrm{d}Q^2}{\int F(y, Q^2) \, \mathrm{d}Q^2} \qquad (5.7)$$

$$F(y) = \int F(y, Q^2) \, \mathrm{d}Q^2 \qquad (5.8)$$

$$\mathcal{F} = \iint F(y, Q^2) \, \mathrm{d}y \, \mathrm{d}Q^2 \qquad (5.9)$$

$$= \int F(y) \, \mathrm{d}y$$

$$\varepsilon\mathcal{A} = \frac{\iint \epsilon(y) \, A(y, Q^2) \, F(y, Q^2) \, \mathrm{d}y \, \mathrm{d}Q^2}{\iint F(y, Q^2) \, \mathrm{d}y \, \mathrm{d}Q^2} \qquad (5.10)$$

$$= \frac{\int \epsilon(y) \, A(y) \, F(y) \, \mathrm{d}y}{\mathcal{F}}$$

The observed number of events can then be related to the total photoproduction cross section:

$$N = \mathcal{L} \cdot \varepsilon\mathcal{A} \cdot \mathcal{F} \cdot \sigma^{\gamma p}_{\mathrm{tot}} \qquad (5.11)$$

An identical expression holds for any partial cross section σ_i with only ε_i being dependent on the sub process i. The total number of observed events may then be rewritten:

$$N = \mathcal{L} \cdot \mathcal{F} \cdot \sum_{\substack{i=\mathrm{ND,EL,} \\ \mathrm{GD,PD,DD}}} \varepsilon_i \mathcal{A} \cdot \sigma_i^{\gamma p} \tag{5.12}$$

The calculation of the flux–integral is straight forward. For the current integration limits of $y_{\min} = 0.3$, $y_{\max} = 0.7$ and $Q_{\min}^2 = m_e^2 \frac{y^2}{1-y}$, $Q_{\max}^2 = 0.01 \ \mathrm{GeV}^2$ the flux–integral results to the dimensionless number $\mathcal{F} = 0.0136$.

More difficulties arise in the calculation of the averaged acceptance of the electron tagger. The acceptance $A(y, Q^2)$ of the electron tagger for scattered electrons (positrons) depends strongly on the HERA beam optics and is most sensitive to the horizontal tilt θ_x of the e^+–beam and the horizontal offset Δx_{off} of the reference trajectory at the H1 interaction point. The e^+–beam tilt is measured to a precision of ± 0.02 mrad by monitoring the position of the photon spot at the photon detector. The offset of the reference trajectory is determined using H1LUMI a specialized Monte–Carlo program [75] for a description of both electron tagger and the HERA beam line (see fig 5.8). The acceptance $A^{\mathrm{BH}}(y)$, integrated over Q^2, can be determined from $ep \to ep\gamma$ events. However, $A^{\mathrm{BH}}(y)$ differs from the acceptance for photoproduction $A(y)$ due to different Q^2 dependences that they are integrated over. The tuned Monte–Carlo describing electron tagger and the beam line was then reused for a calculation of $A(y)$ for the photoproduction case. The shape of the so resulting acceptance of the electron tagger is depicted in figure 5.9. The error on the integrated acceptance $\int A(y) \, \mathrm{d}y$ is estimated using extreme but still acceptable values for the horizontal tilt θ_x and offset x_{off} in the calculation of $A(y)$. In a limited range of $0.3 < y < 0.7$ a conservative estimate of the precision of the electron tagger acceptance of 5% is determined.

The averaged efficiency $\varepsilon \mathcal{A}$ is calculated from Monte–Carlo. The relative contributions of the generated events follows the y–distribution of photon–flux, therefore:

$$\varepsilon_i \mathcal{A} = \frac{\displaystyle\sum_{\substack{\text{events of type } i, \text{ fulfilling} \\ \text{trigger and selection criteria}}} A(y_{\mathrm{event}})}{\displaystyle\sum_{\substack{\text{all generated events} \\ \text{of type } i}}} \tag{5.13}$$

The values for ε_i alone can be obtained using above formula without weighting each event with the acceptance of the electron tagger (e.g. $A(y) \equiv 1 \quad \forall \, y$).

For a proper determination of $\varepsilon \mathcal{A}$, the relative contributions of the different event classes have to be known.
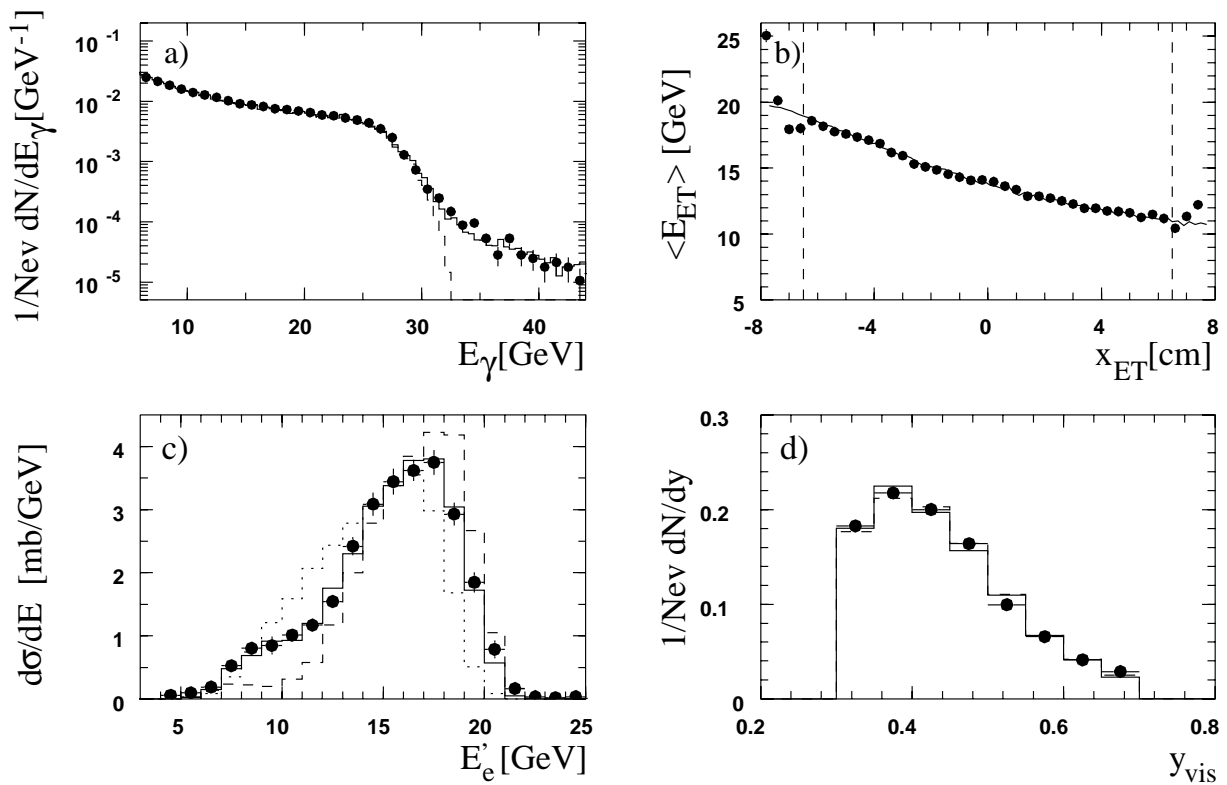
Figure 5.8: H1 luminosity system and electron tagger acceptance.

a) Normalized photon energy distribution for Bethe-Heitler events for data (symbols) and Monte–Carlo with (full line) and without (dashed line) event pile-up. (Several overlapping $ep \rightarrow ep\gamma$ events in the same bunch crossing.)

b) Correlation between the energy and the lateral coordinate of the impact point of scattered electrons in the electron tagger for data (symbols) and Monte–Carlo (full line). Vertical lines indicate the fiducial cut $|x_{ET}| < 6.5$ cm used in the analysis.

c) Energy spectrum in the electron tagger for Bethe-Heitler events. Data (symbols) is compared to Monte–Carlo with measured e-beam tilt $\theta_x = -0.13$ mrad and different offset values of the electron trajectory in the H1 interaction point: $x_{\text{off}} = $ -0.5 mm, +0.5 mm, +1.5 mm (dashed, full and dotted lines respectively).

d) y-distribution in the electron tagger for γp events in the range $0.3 < y < 0.7$ used in this analysis. The points represent the H1 data, histograms are Monte–Carlo predictions for PYTHIA (solid) and PHOJET (dashed) models.

The detector simulation program H1SIM tags each generated event with an unique run number, corresponding to an effective run number of H1 data taking. All varying run
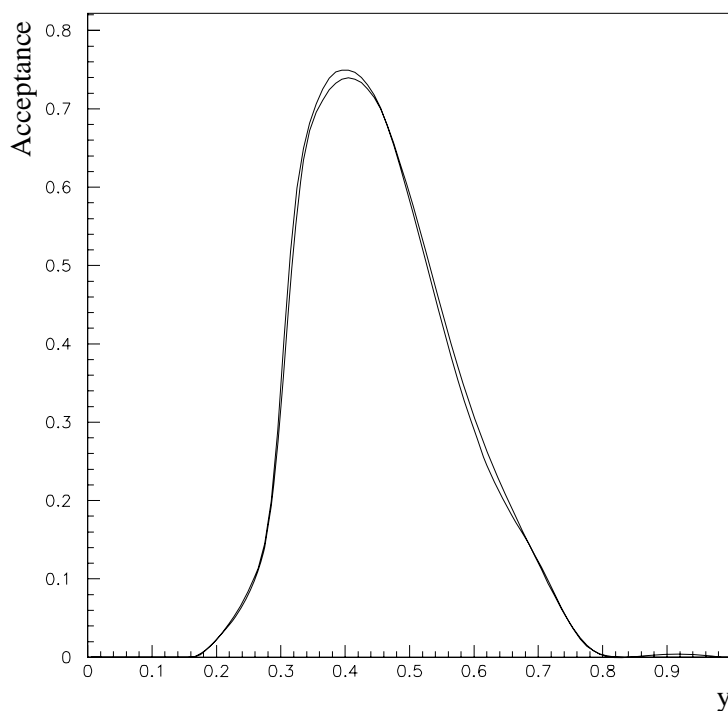
Figure 5.9: The acceptance $A(y)$ of the electron tagger is determined using Bethe–Heitler events ($Q^2 \equiv 0$) together with a Monte–Carlo transformation for a correct averaging of $A(y, Q^2)$ over Q^2 for the photoproduction case. Two different acceptance curves corresponding to two different run ranges have been evaluated to cope with systematics arising from varying beam conditions.

conditions (i.e. electron tagger acceptance, see fig 5.9) are averaged the same way in simulation as in data, since the relative contribution of simulation events per run corresponds to the actual integrated run–luminosity taken.

Equation (5.13) illustrates once again, that only the simulation of the trigger response sufficient accurate, the calculation of the average efficiency can be carried out.

The integrated luminosity $\mathcal{L}$ is determined from the continuous measurement of the rate of Bethe–Heitler events, the known cross section for Bethe–Heitler events and the acceptance of electron tagger and photon detector (see section 3.4). The final values for the integrated luminosity for the three event samples taken are listed in table 5.1.

5.6   Cross section measurement

For a measurement of the total photoproduction cross section, the knowledge of the relative contributions of the sub classes is of vital importance, as the final efficiency $\varepsilon \mathcal{A}$ is

calculated out of the weighted sum of the individual efficiencies $\varepsilon_i \mathcal{A}$ of the sub classes. Since the five sub classes can in principle be distinguished from their different topologies (see figs 5.1–5.5) a measurement is possible. It is found, that the most convenient variables to use, if one wants to distinguish the photoproduction sub classes, are $\eta_{\max}$ and $\eta_{\min}$, formed out of the rapidity distribution of the hadronic final state. In these variables the event distributions differ the most for the sub classes and the smallest model dependence is observed. For each event, $\eta_{\max}$ ($\eta_{\min}$) is defined as the maximum (minimum) pseudo–rapidity of all reconstructed charged tracks and all clusters in the LAr calorimeter with energy larger than 400 MeV (see fig 5.10).
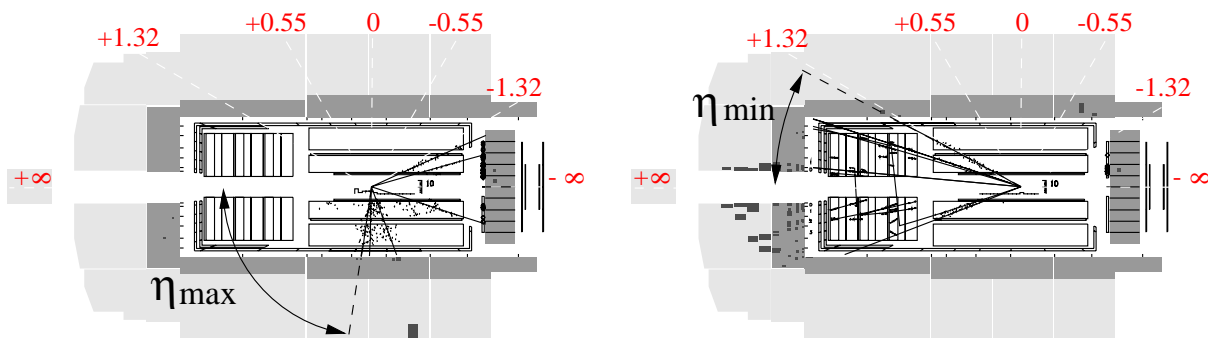

Figure 5.10: Definition of $\eta_{\max}$ and $\eta_{\min}$. The numbers indicate the value of pseudo–rapidity η corresponding to the angular position.

In diffractive events $\eta_{\max}$ indicates the maximum pseudo–rapidity of secondary hadrons from the photon fragmentation, whereas $\eta_{\min}$ indicates the minimum pseudo–rapidity of secondary hadrons from proton fragmentation. In proton diffractive (PD) events, the photon remnant consists out of the decay–products of the vector meson, traveling close the beam line in backward direction. For that reason, $\eta_{\min}$ excludes the region $\eta < -2$.

Table 5.2 presents the different efficiencies ε_i for various data samples as calculated from Monte–Carlo simulations based on both PHOJET and PYTHIA. Apparently, the z–Vertex trigger is most efficient and least model dependent for non–diffractive events, whereas elastic events escape detection completely. A separation of the different sub classes becomes possible using sub samples of the shifted vertex data, with $\eta_{\max} < 0$ and $\eta_{\min} > 1$.

The $\eta_{\max}$ and $\eta_{\min}$ distributions for the shifted vertex data sample is shown in figure 5.11. For the $\eta_{\max}$ spectrum, an additional cut, requiring the calorimetric energy with $\eta > 1$ to be less than 1 GeV, was applied to reduce the contribution from non–diffractive events. As additional condition for the distribution in $\eta_{\min}$ a reconstructed charged track with $\eta < -2.4$ for tagging low mass hadronic systems on the photon side was required.

All four diffractive reactions contribute to the $\eta_{\max}$ spectrum in the range $-3.5 < \eta_{\max} < 0$,

sample	sub sample	sub process				
		GD	PD	DD	EL	ND
nominal vertex z–Vertex trigger	all events	57(65)	8(14)	62(52)	0(0)	95(94)
nominal vertex ToF trigger	all events	66(73)	42(46)	68(72)	29(26)	65(70)
shifted vertex ToF trigger	all events	74(77)	68(71)	71(73)	57(54)	61(65)
	$\eta_{max} < 0$	31(28)	28(18)	15(17)	52(50)	0.1(0.1)
	$\eta_{min} > 1$	0.2(0.3)	21(26)	3.4(3.1)	0.4(0.4)	0.1(0.1)

Table 5.2: Efficiencies ε_i (%) of the different γp sub processes as calculated using Monte–Carlo simulation based on PHOJET (PYTHIA) for various data samples. The statistical errors on these numbers are due to the large data samples generated of minor importance ($\lesssim 1\%$) and are not shown here.

where the contribution from non–diffractive events is small[†].

Below $\eta_{\max} = -2$ the spectrum is dominated by elastic and single proton diffraction reactions. For both channels the variable $\eta_{\max}$ is determined by the decay products from the vector meson. For single proton diffraction events this means, that only those events with a small diffractive mass ($M_X < 10$ GeV/c^2), where secondary particles escape detection through the beam hole, contribute to the $\eta_{\max} < -2$ region. These two contributions have practically indistinguishable shape but have different efficiencies.

The region $-2 < \eta_{\max} < 0$ is dominated by single photon and double diffractive dissociation contributions, which have again similar shape but different acceptances.

The $\eta_{\min}$ distribution is dominated by non–diffractive contributions, which fall nearly exponentially with increasing $\eta_{\min}$. Proton diffraction dissociation processes cause a flat region in the spectrum with $\eta_{\min} > 1$, where the mass M_X of the hadronic system produced on the proton side is larger than about 5 GeV/c^2. Both, single proton and double diffractive dissociation contributions show a similar shape but have again different efficiencies.

A combined fit of the $\eta_{\max}$ and $\eta_{\min}$ spectra in the intervals $-3.5 < \eta_{\max} < 0$ and $1 < \eta_{\min} < 3.5$ using formula (5.12) yields the individual diffractive γp cross sections. The shape of the spectra for each partial contribution is taken from the simulation, while the cross sections σ_i for single diffractive dissociation and elastic reactions are left as free fit parameters. Only three of the four diffractive cross sections can be reliably extracted from this fit, therefore an assumption about the value of the double diffractive dissociation

---

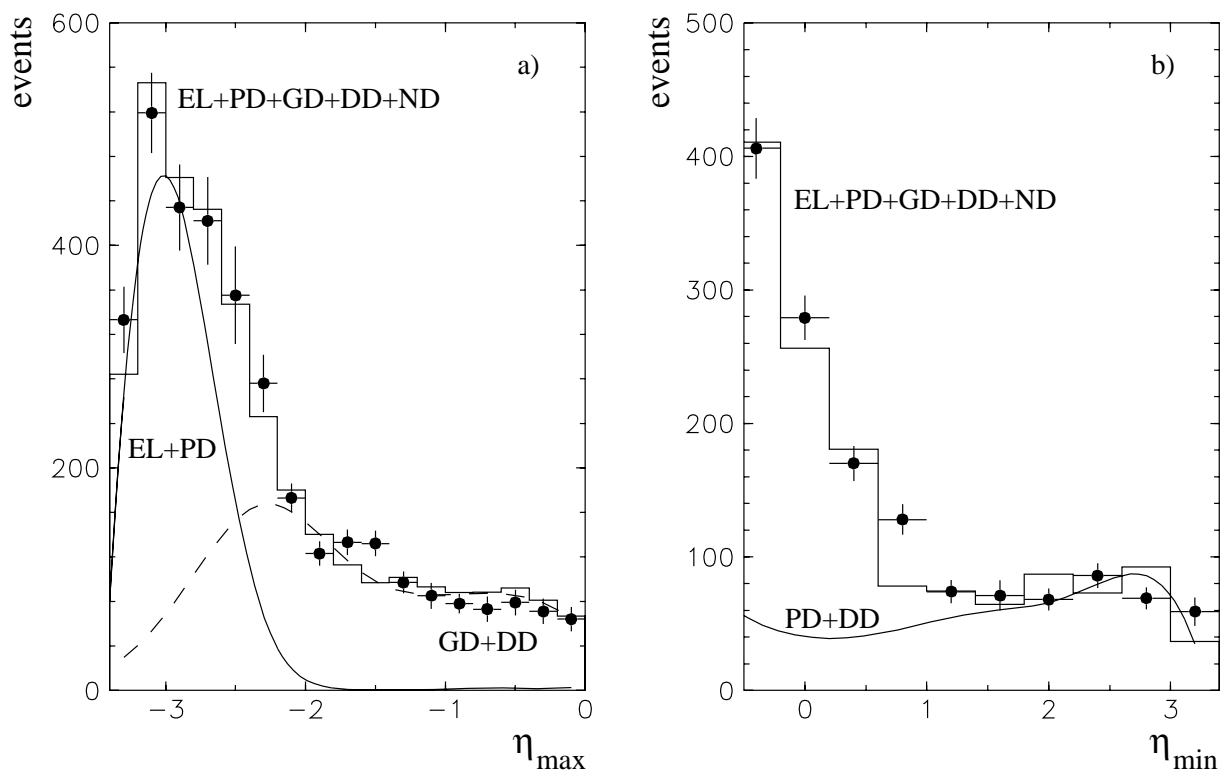[†]The spectrum of $\eta_{\max}$ for non–diffractive events falls nearly exponentially with decreasing $\eta_{\max}$ [76].

Figure 5.11: η_{max} and η_{min} distributions for the shifted vertex sample. Data points are shown using solid circles, the histogram represents the result of a combined fit based on PHOJET summing all five contributions and assuming $\sigma_{\mathrm{DD}} = 20\ \mu\mathrm{b}$.

a) The full line represents the sum of elastic and single proton diffraction, whereas the dashed line represents the sum of single photon and double diffraction.

b) The sum of single proton and double diffraction is shown by the full line.

cross section is needed. We varied it in the range from 0 to 40 μb. The upper value of 40 μb is chosen to be about twice as large as the value expected from extrapolating low energy measurements using equation (1.55).

We tried also to determine the double diffractive dissociation contribution directly from data by observing high mass dissociation on both the proton and the photon side. The results fall into the expected region, but are inconclusive.

To assess the systematic uncertainties due to model dependences, we compare, as was mentioned above, the two different Monte–Carlo generators (PYTHIA and PHOJET) but vary also the main parameters of the diffractive reactions within each model. These parameters are the value of the nuclear slope B, the minimum value for the mass of the dissociating system and the shape of the mass dependence of the cross section:

- The value of the *nuclear slope* was varied by $\delta B = \pm 4$ GeV^{-2} for elastic processes and half this range for single dissociation processes. This represents a conservative estimate of the uncertainty in the extrapolations of the measured slope B from low energy data [29].

- The uncertainty in the description of the *low mass part* of the dissociated mass spectrum [29, 31] was conservatively estimated by increasing the value of the minimum mass of the diffractively produced hadronic system by 0.2 GeV/c^2.

- For the *Mass dependence* of single and double diffractive dissociation we proceed as follows. Low energy photoproduction data [29] and hadron–hadron diffractive dissociation at $\sqrt{s} = 546$ GeV [77] are well described by a phenomenological $1/M_X^2$ dependence. However, predictions from Regge theory, give a $1/M_X^{2+2\Delta}$ dependence (see equation (1.52)). Using the Donnachie–Landshoff fit for the value Δ of 0.08 (see section 1.8, page 18) leads to a $1/M_X^{2.2}$ mass distribution in the Monte–Carlo for a save estimate on the uncertainty on this parameter.

For every variation of one of these parameters, the results are averaged and half the spread is taken as the corresponding possible systematic error. These errors are added in quadrature. Similarly, the results obtained from PYTHIA and PHOJET are averaged.

Taking the fit results for the cross sections of the sub reactions from the vertex shifted data together with the ToF triggered data sample for a determination of the non–diffractive contribution, in principle determines the total cross section. Having in mind, that the ToF trigger is only sensitive on the photon remnant passing the material of the BEMC for diffractive events and only on arbitrary particles traveling in backward direction for non–diffractive events, leads to take the relative contributions of the individual cross sections of the sub processes only for a final determination of the total cross section. Table 5.3 shows the fitted relative contributions of the different cross sections to the total cross section for various Monte–Carlo predictions. The value for the double diffractive contribution is used as input–parameter for the fit procedure, accordingly, for different assumptions on σ_{DD} different fit–results are observed.

The z–Vertex trigger is sensitive on hadronic final states reaching the central part of the H1 detector and can be used for a final determination of the total cross section, using the relative cross section contributions as input. The variation of the different model descriptions can then be used for a determination of systematic error. The efficiency for elastic events in the z–Vertex triggered data sample, independent from any model assumptions, is equal to zero, but with the known relative contribution of this reaction, the total cross section can still be evaluated.

EL : GD : PD : DD : ND	EL : GD : PD : DD : ND
PHOJET $1/M_X^2$	PHOJET $1/M_X^{2.2}$
12.8 : 31.4 : 10.4 : 0.0 : 100.8	10.0 : 26.5 : 11.9 : 0.0 : 104.0
13.7 : 27.1 : 8.5 : 10.0 : 96.8	11.5 : 21.2 : 9.4 : 10.0 : 101.1
14.2 : 24.4 : 7.5 : 16.3 : 94.0	12.2 : 18.5 : 8.2 : 15.6 : 99.0
14.5 : 22.9 : 6.9 : 20.0 : 92.3	12.7 : 16.5 : 7.3 : 20.0 : 97.1
15.2 : 19.0 : 5.5 : 30.0 : 87.5	13.7 : 12.1 : 5.5 : 30.0 : 92.5
15.8 : 15.3 : 4.1 : 40.0 : 82.4	14.7 : 7.8 : 3.7 : 40.0 : 87.8

PHOJET $\delta B_{\mathrm{EL}} = +4$ GeV^{-2}
            $\delta B_{\mathrm{D}} = +2$ GeV^{-2}
	PHOJET $\delta B_{\mathrm{EL}} = -4$ GeV^{-2}
	            $\delta B_{\mathrm{D}} = -2$ GeV^{-2}

11.5 : 30.3 : 11.7 : 0.0 : 99.6	14.5 : 34.9 : 11.0 : 0.0 : 92.7
12.7 : 26.1 : 9.3 : 10.0 : 95.0	15.1 : 29.9 : 9.2 : 10.0 : 88.9
13.6 : 23.0 : 7.8 : 17.7 : 91.2	15.4 : 26.6 : 8.1 : 17.0 : 86.0
13.8 : 22.1 : 7.3 : 20.0 : 89.9	15.6 : 25.2 : 7.6 : 20.0 : 84.8
14.6 : 18.3 : 5.7 : 30.0 : 84.5	16.1 : 20.9 : 6.0 : 30.0 : 80.2
15.4 : 14.8 : 4.2 : 40.0 : 78.7	16.5 : 16.9 : 4.3 : 40.0 : 75.4

PHOJET
        $M_X > M_{\mathrm{in}} + 2m_\pi + 0.2$ GeV/c^2
	PYTHIA
	                 $1/M_X^2$

14.2 : 30.2 : 9.7 : 0.0 : 99.1	17.4 : 34.5 : 8.3 : 0.0 : 90.5
14.9 : 26.0 : 8.3 : 10.0 : 94.0	18.0 : 28.9 : 7.1 : 10.0 : 87.6
15.2 : 24.0 : 7.6 : 15.1 : 91.2	18.3 : 26.7 : 6.7 : 13.7 : 86.4
15.5 : 22.1 : 7.0 : 20.0 : 88.5	18.6 : 23.1 : 6.2 : 20.0 : 84.4
16.0 : 18.6 : 6.0 : 30.0 : 82.6	18.8 : 17.8 : 5.6 : 30.0 : 80.8
16.4 : 15.2 : 5.1 : 40.0 : 76.5	18.9 : 13.0 : 5.2 : 40.0 : 76.8

Table 5.3: The relative contributions of the different sub processes to the total cross section as determined out of a combined fit of various Monte–Carlo predictions and different assumptions on the contribution of double diffractive dissociation to the $\eta_{\mathrm{max,min}}$ distributions of the shifted vertex data sample and the ToF triggered data sample.

5.7   Corrections

Before the final cross section can be given, a series of correction factors have to be taken into account:

- The contamination from p–pilot events has been estimated using the y–spectrum from ETAG–monitor data.

- The fraction of events lost due to the vertex cut $|Z_{\mathrm{vtx}} - 4\text{ cm}| < 30$ cm has been evaluated using the official H1 luminosity tools [78], which consider also the bunch structure of the proton satellite bunches.

- The resolution of the electron tagger scales with the energy of the scattered positron as $15\%/\sqrt{E'}$, this leads to a systematically wrong y–integration near the lower bound of the fiducial y–region. (The same effect at the higher bound is much smaller, but although considered.)

- QED radiative corrections, such as single photon emission from the incoming or outgoing positron or self energy corrections to the Born photoproduction cross section have been calculated using the HERACLES Monte–Carlo program [79].

- Inefficiency of the photon veto yields to a contamination with QED events which has been estimated using the measured rate of the Bethe–Heitler process.

Table 5.4 summarizes the correction factors with their errors.

Correction factors	
Background subtraction	$-3\%^{+3\%}_{-0\%}$
Z_{vtx} cut	$+3\%\pm0.3\%$
Electron tagger resolution	$+2\%^{[1]}$
Radiative corrections	$-1\%\pm1\%$
Photon veto	$+0.5\%\pm0.5\%$
Total corrections	$+1.5\%^{+3.2\%}_{-1.2\%}$

Table 5.4: Correction factors for the total cross section.
[1] error already included in overall etag acceptance.

An overall correction to the trigger efficiency for the z–Vertex trigger can be determined using the ToF triggered data sample. For each event from the ToF data sample, where additionally at least one driftchamber track was asked, it can be checked whether the z–Vertex trigger condition was also fulfilled, this can be done in data as well as in Monte–Carlo. The difference between these two efficiencies corrects the z–Vertex trigger efficiency determined from Monte–Carlo alone. From 16662 events from the ToF triggered data sample with at least one driftchamber track, 14216 events satisfy the trigger condition for the z–Vertex triggered data sample, which corresponds to a measured overall efficiency of 85.3% for the z–Vertex trigger. As the ToF and z–Vertex trigger work

independently from each other[†], the only bias in this correction is expected from the event topology itself[††]. But with a correct description of the event topology in Monte–Carlo, such a bias is already described and the correction factor determined from the overlap sample, where both trigger fired, can be applied to the whole sample.

The relative contributions of the sub reactions fix the weighted efficiency $\varepsilon\mathcal{A}$ and, after applying the different correction factors, the total cross section is determined up to the assumptions used in the Monte–Carlo models. Table 5.5 presents the resulting total cross section for various Monte–Carlo predictions and various assumptions on the relative contribution of double diffraction dissociation.

The total cross section is remarkably insensitive to the assumption about the contribution of σ_{DD} and changes only by 0.3 μb (3.9 μb) in PHOJET (PYTHIA). The average value for the cross section between the PHOJET $(1/M_X^2)$ and PYTHIA prediction is ascribed to the final number. A value of 164.6 μb is obtained.

5.8   Errors

The statistical error is determined from the measured number of photoproduction events and plays only a minor rôle in the full error (statistical and systematic error added in quadrature). The main source of systematic errors lies in the acceptance determination of the electron tagger. The systematic errors resulting from the different Monte–Carlo assumption can be retrieved directly from table 5.5.

The systematic error from the trigger efficiency from the z–Vertex trigger alone can be checked by varying the thresholds in the simulation of the proportional chambers CIP and COP (CDM2 bank, cf. section 4.7.3). A global variation of $\pm3\%$ around the values which fit the data best seems to be sufficient to contain all variations of the track acceptance within save bands, as can be seen in figure 5.12. Rerunning the Monte–Carlo for photoproduction using the altered thresholds leads to different results for the total cross section. This variation leads to a marginal effect of ±0.3 μb, since typically 10 charged tracks are observed in the central driftchamber on average, from which only one needs to enable at least one ray. A small variation of the thresholds leads therefore to a variation of the total number of active rays, which is typically far above one ray. The relatively large correction

---

[†]The ETAG signal is applied to both data samples the same way and does not influence the argumentation.

[††]No bias occurs in elastic and proton diffractive events, as the decay products from the vector meson never fulfill the z–Vertex trigger condition, but are only visible in the ToF scintillating layers. Non–diffractive events are essentially bias free because their trigger efficiency is close to 100%. The only two remaining channels are photon diffraction and double diffraction, which contribute typically 25% to the total cross section.

σ_{DD} [μb]	$\varepsilon\mathcal{A}$	$\varepsilon_{\text{zvx}|\text{ToF}}$	corr$_\varepsilon$	$\sigma_{\text{tot}}^{\gamma p}$ [μb]	σ_{DD} [μb]	$\varepsilon\mathcal{A}$	$\varepsilon_{\text{zvx}|\text{ToF}}$	corr$_\varepsilon$	$\sigma_{\text{tot}}^{\gamma p}$ [μb]
PHOJET			$1/M_X^2$		PHOJET			$1/M_X^{2.2}$	
0.0	44.2	89.5	4.9	162.7	0.0	44.4	90.0	5.5	160.1
10.4	44.2	88.8	4.1	162.6	10.4	44.7	89.6	5.0	159.8
16.9	44.1	88.4	3.6	162.6	16.2	44.8	89.2	4.6	159.8
20.8	44.1	88.1	3.3	162.6	20.8	44.8	89.0	4.3	159.8
31.1	43.8	87.3	2.3	162.8	31.2	44.7	88.3	3.4	159.9
41.4	43.6	86.5	1.4	163.0	41.6	44.6	87.6	2.6	160.1
PHOJET		$\delta B_{\text{EL}} = +4$ GeV^{-2}			PHOJET		$\delta B_{\text{EL}} = -4$ GeV^{-2}		
		$\delta B_{\text{D}} = +2$ GeV^{-2}					$\delta B_{\text{D}} = -2$ GeV^{-2}		
0.0	43.9	89.5	4.8	162.6	0.0	43.3	88.7	3.9	167.1
10.6	44.0	88.8	4.0	162.5	10.9	43.3	88.1	3.2	166.6
18.8	44.0	88.2	3.4	162.7	18.5	43.2	87.6	2.7	166.3
21.3	43.9	88.0	3.2	162.7	21.7	43.2	87.4	2.4	166.2
31.9	43.7	87.2	2.2	163.0	32.5	43.1	86.6	1.6	166.0
42.7	43.3	86.3	1.2	163.5	43.3	42.9	85.9	0.7	165.6
PHOJET					PYTHIA				
	$M_X > M_{\text{in}} + 2m_\pi + 0.2$ GeV/c^2							$1/M_X^2$	
0.0	44.4	89.6	5.0	164.0	0.0	44.8	88.5	3.7	164.6
10.7	44.2	88.8	4.1	164.3	10.9	44.2	87.3	2.3	165.4
16.2	44.1	88.4	3.6	164.4	15.0	44.0	86.9	1.8	165.9
21.5	43.9	88.0	3.1	164.6	21.9	43.5	86.1	0.9	166.5
32.4	43.4	87.0	2.0	165.2	32.8	42.6	84.8	-0.6	167.5
43.3	42.9	86.1	0.9	165.8	43.8	41.7	83.4	-2.2	168.5

Table 5.5: Total cross sections for various assumptions on the contribution of the double diffractive dissociation and for various Monte–Carlo predictions. Presented are the weighted efficiency $\varepsilon\mathcal{A}$ [%], the efficiency for the z–Vertex trigger for events already fulfilling the ToF trigger condition ε_{zvx} [%] determined from the Monte–Carlo and the correction to the trigger efficiency corr$_\varepsilon$ [%] determined by the latter. The final value for the total cross section is determined out of the average from the PYTHIA and PHOJET results.

to the trigger efficiency results therefore from the lack of knowledge about the hadronic final state in the central detector and does not result from a insufficient description of the proportional chambers.

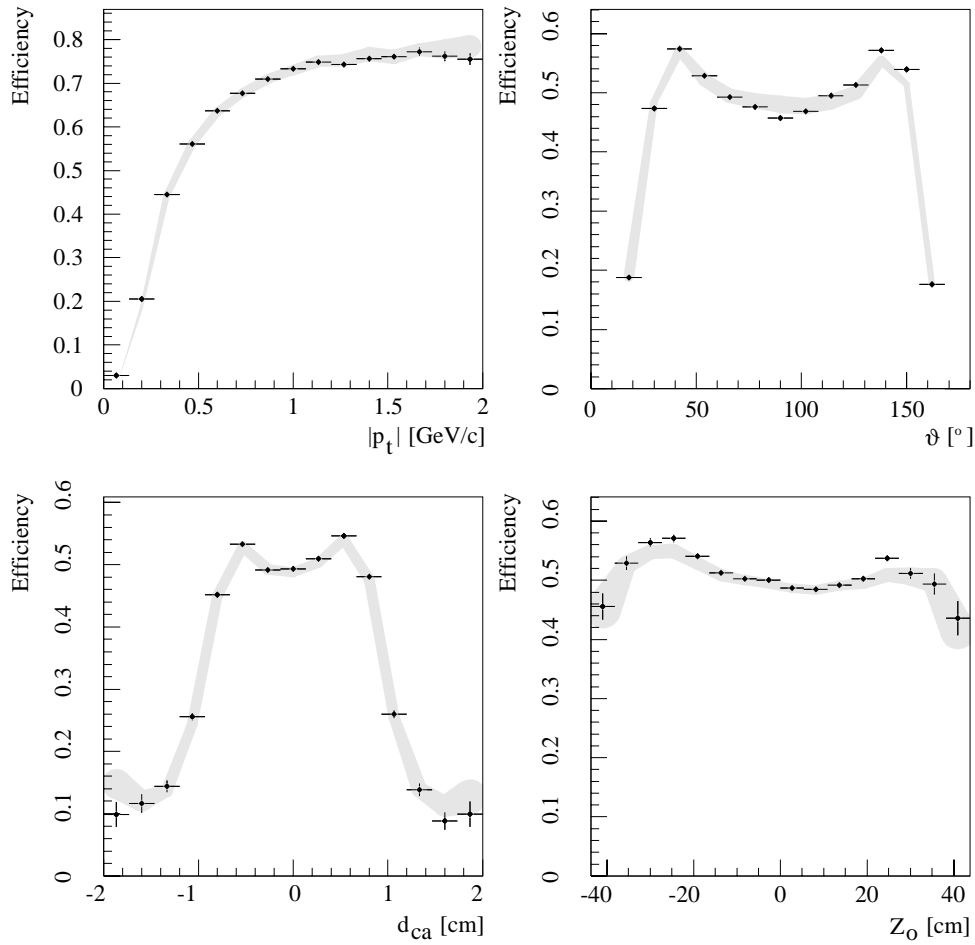Table 5.6 shows all errors which have to be added in quadrature to obtain the final error.

Figure 5.12: Systematic error due to z–Vertex single track acceptance. A variation of the CDM2 thresholds by $\pm 3\%$ yields to the gray band, showing the variation of the single track acceptance of the z–Vertex trigger. Data is shown using dots with error bars.

For the total photoproduction cross section at an average $W_{\gamma p}$ of 200 GeV a value of

$$\sigma_{\text{tot}}^{\gamma p} = 164.6 \ \pm \ 2.3 (\text{stat.}) \ {}^{+10.6}_{-\ 9.5} (\text{syst.}) \ \mu\text{b}$$

is obtained. The statistical error reflects the statistical uncertainties for the z–Vertex triggered data sample, as well as those from the Monte–Carlo calculations. The most dominant source is the uncertainty of the electron tagger acceptance.

Source	Error [%]	Error [μb]
assumption on contribution of double diffractive dissociation	1.2	2.0
uncertainty due to model dependence PYTHIA/PHOJET	1.2	1.9
systematic errors of diffractive cross sections		
$1/M_X^{2.2}$	0.9	1.4
$\delta B_{\mathrm{EL\,(D)}} = +4\ (2)\ \mathrm{GeV}^{-2}$	0.1	0.1
$\delta B_{\mathrm{EL\,(D)}} = -4\ (2)\ \mathrm{GeV}^{-2}$	0.2	0.3
$M_X > M_{\mathrm{in}} + 2m_\pi + 0.2\ \mathrm{GeV/c}^2$	0.6	1.1
error of efficiency correction $\mathrm{corr}_\varepsilon$	0.4	0.6
systematic error of trigger efficiency ε	0.2	0.3
background subtraction	$\left\{{}^{+3.0}_{-0.0}\right.$	$\left\{{}^{+4.9}_{-0.0}\right.$
Z_{vtx} cut	0.3	0.5
radiative corrections	1.0	1.6
photon veto	0.5	0.8
luminosity measurement	1.6	2.6
electron tagger acceptance	5.0	8.2
Total	$\left\{{}^{+6.5}_{-5.8}\right.$	$\left\{{}^{+10.6}_{-\ 9.5}\right.$

Table 5.6: Contributions to systematic errors of the $\sigma_{\mathrm{tot}}^{\gamma p}$ measurement.

5.9 Discussion

The energy dependence of $\sigma_{\mathrm{tot}}^{\gamma p}$ is illustrated in figure 5.13 with low energy data [28] and the present measurement together with a recent result from ZEUS [80]. The data is compared to predictions made by A. Donnachie and P.V. Landshoff (DL) [13] and by H. Abramowicz, E. M. Levin, A. Levy and U. Maor (ALLM) [22].

The DL curve presents the Regge parameterization, in which the high energy behavior of $\sigma_{\mathrm{tot}}^{\gamma p}$ is described by a function $W_{\gamma p}^{2\Delta}$ with $\Delta = 0.0808$. The dotted line represents a further DL–type parameterization, which takes the recent CDF measurement of the total $p\bar{p}$ cross–section [81] into account with $\Delta = 0.11$. The ALLM parameterization is also a Regge–type cross section parameterization, which describes real and virtual photon proton collisions with $\Delta = 0.045$.

The DL prediction is surprisingly well supported by our measurement, strengthening the concept of the soft, supercritical pomeron exchange as the dominant mechanism of ultra hard (real) photon proton reactions.
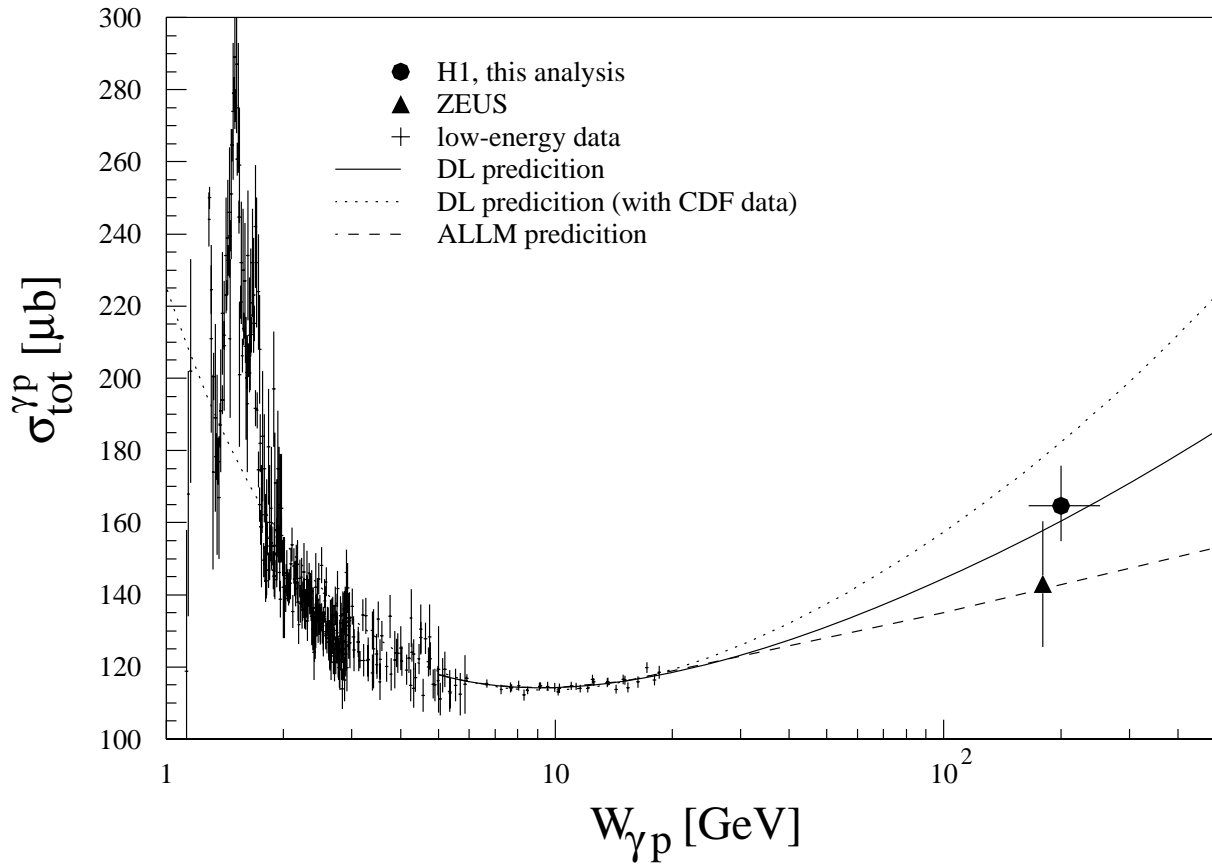
Figure 5.13: Total photoproduction cross section as function of the γp center–of–mass energy $W_{\gamma p}$.

Appendix A

Efficiency determination

A problem often encountered is the determination of an efficiency value for a detector part out of a finite number of events, where it was checked wether the detector was active (efficient) or inactive (inefficient). Let n be the total number of checks and let k be the total number where the detector was found to be efficient. The resulting efficiency ε and variance σ^2, as it can be found in any textbook on statistic [82], reads then as follows:

$$\varepsilon = \frac{k}{n} \qquad \sigma^2 = \frac{1}{n}\frac{k}{n}(1 - \frac{k}{n})$$

Unfortunatley above estimate for ε and σ does not lead to satisfactory results in the case where n is not large enough, or where ε is either close to 1 or 0. Take the case, where out of 5 measurements the detector was (by accident) 5 times efficient, then the efficiency reads as 1.0 ± 0.0, which is a good bluff in its best formulation.

A more realistic estimate can be found out of the Likelihood function for a binominal probability density distribution

$$L(\varepsilon) = \binom{n}{k}\varepsilon^k(1 - \varepsilon)^{n-k}$$

but instead of maximizing above function, which leads to above results, the expectation value can be ascribed for a new estimate on the efficiency and the width to a new estimate on the variance.

$$< \varepsilon > = \frac{\int\limits_0^1 \varepsilon \cdot L(\varepsilon)\,\mathrm{d}\varepsilon}{\int\limits_0^1 L(\varepsilon)\,\mathrm{d}\varepsilon} \qquad < \varepsilon^2 > = \frac{\int\limits_0^1 \varepsilon^2 \cdot L(\varepsilon)\,\mathrm{d}\varepsilon}{\int\limits_0^1 L(\varepsilon)\,\mathrm{d}\varepsilon} \qquad \sigma^2 = < \varepsilon^2 > - < \varepsilon >^2$$

These integrations can be performed analytically and yields to following values:

$$\varepsilon = \frac{k+1}{n+2} \qquad \sigma^2 = \frac{k+1}{n+2}\left(\frac{k+2}{n+3} - \frac{k+1}{n+2}\right)$$

In the limit of a large n, this result is identical to the classical result when k is not close to n or 0.

$$\lim_{n\to\infty} \frac{k+1}{n+2} = \frac{k}{n}$$

$$\lim_{n\to\infty,\, k\approx n/2} \frac{k+1}{n+2}\left(\frac{k+2}{n+3} - \frac{k+1}{n+2}\right) = \frac{1}{4n+12} \approx \frac{1}{4n}$$

$$\lim_{n\to\infty,\, k\approx n/2} \frac{1}{n}\frac{k}{n}(1 - \frac{k}{n}) = \frac{1}{4n}$$

Differences occur, when k is close to n or 0, here the classical result yields to a vanishing variance, whereas the new formulation yields to a more reasonable one.

$$\lim_{n\to\infty,\, k\approx n,0} \frac{k+1}{n+2}\left(\frac{k+2}{n+3} - \frac{k+1}{n+2}\right) = \frac{n+1}{(n+2)^2(n+3)} \approx \frac{1}{n^2}$$

This new formulation even gives a reasonable result before any measurement took place:

$$\varepsilon(0,0) = 0.5 \pm 0.3$$

Being completely naïve, the best is to put the value into the middle, with the error bars large enough to be compatible (within 2 sigmas) with either boundary.

This formulation of efficiency and standard deviation has been used throughout this thesis.

Index

Bibliography

[1] H1 Collaboration, "*A Measurement of the Proton Structure Function $F_2(x, Q^2)$*", Nuclear Physics **B439** (1995) 471.

[2] K. Müller, "*Measurement of the proton structure function F_2 at low Bjorken x at the H1 experiment*", PhD thesis, University of Zürich, 1994.

[3] H1 Collaboration, "*Total Photoproduction Cross–Section Measurement at HERA Energies*", Physics Letters **B299** (1993) 374.

[4] H1 Collaboration, "*Inclusive Parton Cross–Sections in Photoproduction and Photon Structure*", Nuclear Physics **B445** (1995) 195.

[5] H1 Collaboration, "*Measurement of the Total Photon Proton Cross Section and its Decomposition at 200 GeV Center of Mass Energy*", Zeitschrift für Physik **C69** (1995) 27, http://xxx.lanl.gov/ps/hep-ex/9509001.

[6] G. Ingelman *et al.*, "*Deep Inelastic Physics and Simulation*", In Peccei [83], p. 3.

[7] ZEUS Collaboration, "*Observation of Events with a large Rapidity Gap in Deep Inelastic Scattering at HERA*", Physics Letters **B315** (1993) 481.

[8] H1 Collaboration, "*Deep Inelastic Scattering Events with Large Rapidity Gap at HERA*", Nuclear Physics **B429** (1994) 477.

[9] NMC Collaboration, "*Precision Measurement of the Structure Function Ratios $F_2(He)/F_2(D)$ and $F_2(Ca)/F_2(D)$*", Zeitschrift für Physik **C51** (1991) 387.

[10] E–665 Collaboration, "*Saturation of Shadowing at very low x_{Bj}*", Physical Review Letters **68** (1992) 3266.

[11] T. H. Bauer, R. D. Spital, D. R. Yennie, and F. Pipkin, "*The hadronic properties of the photon in high–energy interactions*", Reviews of Modern Physics **50** (1978) 261.

[12] G. A. Schuler and T. Sjöstrand, "*Towards a Completer Description of High–Energy Photoproduction*", Nuclear Physics **B407** (1993) 539.

[13] A. Donnachie and P. Landshoff, *"Total cross sections"*, Physics Letters **B296** (1992) 227.

[14] T. Regge, *"Introduction to Complex Orbital Momenta"*, Nuovo Cimento **14** (1959) 951.

[15] T.Regge, *"Bound States, Shadow States and Mandelstamm Representation"*, Nuovo Cimento **18** (1960) 947.

[16] G. F. Chew and S. C. Frautschi, *"Principle of Equivalence for all Strongly Interacting Particles within S–Matrix Framework"*, Physical Review Letters **7** (1961) 394.

[17] C. G. Callan, Jr. and D. J. Gross, *"High–Energy Electroproduction and the Constitution of the Electric Current"*, Physical Review Letters **22** (1969) 156.

[18] F. Halzen and A. D. Martin, *"Quarks & Leptons"*, J. Wiley & Sons, New York, Chichester, Brisbane, Toronto, Singapore, 1984.

[19] L. N. Hand, *"Experimental Investigation of Pion Electroproduction"*, Physical Review **129** (1963) 1834.

[20] C. F. v Weizsaecker, *"Ausstrahlung bei Stössen sehr schneller Elektronen"*, Zeitschrift für Physik **88** (1934) 612.

[21] E. J. Williams, *"Nature of the High Energy Particles of Penetrating Radiation and Status of Ionization and Radiation Formulae"*, Physical Review **45** (1934) 729.

[22] H. Abramowicz, E. M. Levin, A. Levy, and U. Maor, *"A parametrization of $\sigma_T(\gamma^* p)$ above resonance region for $Q^2 \geq 0$"*, Physics Letters **B269** (1991) 465.

[23] A. Capella, A. Kaidalov, C. Merino, and J. Tran Thanh Van, *"Structure Functions and Low x Physics"*, Physics Letters **B337** (1994) 358.

[24] S. Frixione, *"Improving the Weizsäcker–Williams approximation in electron proton collisions"*, Physics Letters **B319** (1993) 339.

[25] J. R. Smith, *"Polarization Decomposition of Fluxes and Kinematics in ep Reactions"*, 1993, H1 internal report H1–04/93–282.

[26] J. R. Smith and B. D. Burow, *"Photon Fluxes with Beam Mass Effects and Polarizations"*, 1994, H1 internal report H1–01/94–338.

[27] I. I. Pomeranchuk, *"Equality of the Nucleon and Antinucleon Total Interaction Cross Section at High Energies"*, Soviet Physics JETP **34(7)** (1958) 499.

[28] *"Plots of Cross-Sectios and Related Quantities"*, In Particle Data Group [85], p. 1327, data points in computer readable form from: http://pdg.lbl.gov/xsect/contents.html.

[29] T. J. Chapin, R. L. Cool, K. A. Jenkins, J. P. Silverman, G. Snow, H. Sticker, S. N. White, and Y. H. Chou, *"Diffraction Dissociation of Photons on Hydrogen"*, Physical Review **D31** (1985) 17.

[30] B. D. Burow, M. Erdmann, R. Kaschowitz, S. Levonian, and L. Stanco, *"Photopro-duction Physics at HERA"*, 1994, DESY-94-215.

[31] K. Goulianos, *"Diffractive Intractions of Hadrons at High Energies"*, Physics Reports **101** (1983) 169.

[32] Y. Akimov *et al.*, *"Analysis of diffractive pd → Xd and pp → Xp interactions and test of the finite–mass sum rule"*, Physical Review **D14** (1976) 3148.

[33] K. Goulianos, *"Diffractive Dissociation"*, Nuclear Physics **B12** Proc. Suppl. (1990) 110.

[34] G. Alberi and G. Goggi, *"Diffraction of Subnuclear Waves"*, Physics Reports **74** (1981) 1.

[35] M. Froissart, *"Asymptotic Behavior and Subtractions in the Mandelstamm represen-tation"*, Physical Review **123** (1961) 1053.

[36] A. Martin, *"Unitarity and High-Energy Behavior of Scattering Amplitudes"*, Physical Review **129** (1963) 1432.

[37] J. Pumplin, *"Eikonal Models for Diffraction Dissociation on Nuclei"*, Physical Review **D8** (1973) 2899.

[38] F. E. Low, *"Model of the bare Pomeron"*, Physical Review **D12** (1975) 163.

[39] S. Nussinov, *"Colored–Quark Version of Some Hadronic Puzzles"*, Physical Review Letters **34** (1975) 1286.

[40] E. A. Kuraev, L. N. Lipatov, and V. S. Fadin, *"The Pomeranchuk Singularity in Nonabelian Gauge Theories"*, Soviet Physics JETP **45** (1977) 199.

[41] Y. Y. Balitsky and L. N. Lipatov, *"The Pomeranchuk Singularity in Quantum Chro-modynamics"*, Soviet Journal of Nuclear Physics **28** (1978) 822.

[42] WA91 Collaboration, *"Observation of a Narrow Scalar Meson 1450 MeV in the Re-action $pp → p_f(\pi^+\pi^-\pi^+\pi^-)p_s$ at 450 GeV/c using the CERN Omega Spectrometer"*, Physics Letters **B324** (1994) 509.

[43] B. H. Wiik, *"HERA Status"*, In Buchmüller and Ingelman [84], p. 1.

[44] ZEUS Collaboration, *"The ZEUS Detector"*, 1993, Status Report, DESY.

[45] H1 Collaboration, *"The H1 Detector at HERA"*, 1993, DESY-93-103.

[46] HERMES Collaboration, *"The HERMES Experiment: From the Design to the first Results"*, 1995, DESY-HERMES-95-02.

[47] HERA–B Collaboration, *"An Experiment to Study CP Violation in the B System Using an Internal Target at the HERA Proton Ring"*, 1994, Proposal, DESY-PRC-94-02.

[48] P. Robmann, *"The central inner z–chamber of the H1 Experiment at HERA"*, PhD thesis, University of Zürich, 1994.

[49] S. Eichenberger, *"A Fast Pipelined Trigger for the H1 Experiment at HERA Based on Multiwire Proportional Chamber Signals"*, PhD thesis, University of Zürich, 1993.

[50] S. Eichenberger *et al.*, *"A Fast Pipelined Trigger for the H1 Experiment Based on Multiwire Proportional Chamber Signals"*, Nuclear Instruments and Methods **A323** (1992) 532.

[51] K. Müller *et al.*, *"Construction and Performance of a Thin Cylindrical Multiwire Proportional Chamber with Cathode Pad Readout for the H1 Experiment"*, Nuclear Instruments and Methods **A457** (1992) 456.

[52] H. Bethe and W. Heitler, *"On the Stopping of Fast Particles and the Creation of Positive Electros"*, Proceedings of the Royal Society **A146** (1934) 83.

[53] A. Campbell, *"A RISC multiprocessor event trigger for the data acquisition system for the H1 experiment at HERA"*, 1991, International Conference on Real Time '91, Jülich.

[54] The VMEbus specification, IEEE standard 1014.

[55] R. Gerhards, C. Kleinwort, U. Krüner-Marquis, and F. Niebergall, *"Data Storage and Data Access at H1"*, Contribution to International Conference on Computing in High Energy Physics CHEP95, Rio de Janeiro, Brasil, September 1995.

[56] Creative Electronics System SA, Fast Intelligent Controller FIC 8330/8232, Geneva, Switzerland, 1987/1992.

[57] *"American National Standard Programming Language FORTRAN"*, ANSI X3.9, New York, 1978.

[58] V. Blobel, *"The BOS System"*, 1987, Hamburg DESY - internal report F14-86-02.

[59] R. Eichler *et al.*, *"The First Level MWPC Trigger for the H1 detector"*, 1987, Hamburg DESY - H1 internal report H1-04/87-61.

[60] S. Egli, *"What is available in the H1 UTIL library - a brief overview"*, 1994, Software–note 46, H1 internal.

[61] V. Blobel, *"Online Monitoring and Determination of Run–Dependent Calibration Constants within Reconstruction Modules"*, 1993, Software–note 41, H1 internal.

[62] F. Sauli, *"Principles of Operation of Multiwire Proportional and Drift Chambers"*, 1977, CERN Report 77–09.

[63] H. Bethe, *"Zur Theorie des Durchgangs schneller Korpuskularstrahlen durch Materie"*, Annalen der Physik **5** (1930) 325.

[64] F. Bloch, *"Bremsvermögen von Atomen mit mehreren Elektronen"*, Zeitschrift für Physik **81** (1933) 363.

[65] J. Moyal, *"Theory of Ionization Fluctuations"*, Philosophical Magazine **46** (1955) 263.

[66] I. Endo *et al.*, *"Systematic Shifts of Evaluated Charge Centroid for the Cathode Read–Out Multiwire Proportional Chamber"*, Nuclear Instruments and Methods **188** (1981) 51.

[67] T. Sjöstrand, *"Pythia 5.7 and Jetset 7.4: Physics and Manual"*, 1995, Lund University, LU-TP-95-20, http://xxx.lanl.gov/ps/hep-ph/9508391.

[68] R. Engel, *"Photoproduction within the two Component Dual Parton Model. 1. Amplitudes and Cross–Sections"*, Zeitschrift für Physik **C66** (1995) 203.

[69] G. Marchesini *et al.*, *"HERWIG: A Monte–Carlo Event Generator for Simulating Hadron Emission Reactions with Interfering Gluons"*, Computer Physics Communications **67** (1992), and Hamburg DESY 91–048.

[70] L. Lonnblad, *"ARIADNE Version 4: A Program for Simulation of QCD Cascades Implementing the Color Dipole Model"*, Computer Physics Communications **71** (1992), and Hamburg DESY 92–046.

[71] Application Software Group, *"GEANT: Detector Description and Simulation Tool"*, 1994, Geneva CERN, Computing and Networks Division.

[72] G. Lynch and T. Trippe, *"Monte–Carlo Particle Numbering Scheme"*, In Particle Data Group [85], p. 1325.

[73] T. Sjöstrand and M. van Zijl, *"A Multiple–Interaction Model for the Event Structure in Hadron Collisions"*, Physical Review **D36** (1987) 2019.

[74] A. Capella, U. Sukhatme, C. Tan, and J. Tran Thanh Van, *"Dual Parton Model"*, Physics Reports **236** (1994) 225.

[75] S. Levonian, *"H1LUMI - A Fast Simulation Package for the H1 Luminosity System"*, 1993, H1 internal report H1–04/93–287.

[76] H1 Collaboration, *"Observation of Hard Processes in Rapidity Gap Events in γp Interactions at HERA"*, Nuclear Physics **B435** (1995) 3.

[77] UA4 Collaboration, *"The Cross–Section of Diffraction Dissociation at the CERN SPS Collider"*, Physics Letters **B186** (1987) 227.

[78] S. Levonian and A. Panitch, *"Treatment of the Proton Satellite Bunches in 1994 Data"*, 1995, H1 internal report H1–09/95–454.

[79] A. Kwiatkowski, H. Spiesberger, and H. Möhring, *"HERACLES. An Event Generator for ep Interactions at HERA Including Radiative Processes"*, In Buchmüller and Ingelman [84], p. 1294.

[80] ZEUS Collaboration, *"Measurement of Total and Partial Photon Cross–Sections at 180 GeV Center of Mass Energy"*, Zeitschrift für Physik **C63** (1994) 391.

[81] CDF Collaboration, *"Measurement of the Anti–Proton Proton Total Cross–Section at $\sqrt{s} = 546$ GeV and 1800 GeV"*, Physical Review **D50** (1994) 5550.

[82] S. Brandt, *"Datenanalyse"*, BI–Wissenschaftsverlag, Mannheim, Leipzig, Wien, Zürich, 1992.

[83] R. D. Peccei, editor, *"Proceedings of the HERA Workshop, Hamburg, October 12–14, 1987"*, volume 1 and 2, DESY, 1988.

[84] W. Buchmüller and G. Ingelman, editors, *"Proceedings of the workshop on Physics at HERA, Hamburg, October 29–30, 1991"*, volume 1,2 and 3, DESY, 1992.

[85] Particle Data Group, editor, *"Physical Review D Particle and Fields"*, The American Physical Society, 1994, Part 1, Review of Particle Properties.

Acknowledgment

It was a pleasure to work within the stimulating atmosphere of the many people involved with the H1 experiment. The fruitful time I've spent inside the international collaboration gave me the possibility to evolve my skills in and outside the matter of physics. Particularly I want to express my gratitude to

Prof. Dr. P. Truöl, my advisor, for the chance he gave me to work within the H1 collaboration. He gave me large degrees of freedom in finding and defining my way.

Ueli Straumann for his excellent technical support.

Stefan Eichenberger for introducing me into the depths of z–Vertex trigger.

Curtis Meyer for guiding my first steps into the overwhelming H1 software.

Stephan Egli for his patience in software and physics advises.

Katharina Müller for all that time we've spent solving each others daily puzzles.

Christian Dollfus and Peter Robmann for many discussions on physics and other topics.

Martin zur Nedden and David Müller for their intrepidity in taking over the responsibilities for those detector and software components built by the Zürich group.

Roland Bernet and Josef Riedlberger from the ETH part of the H1 collaboration. It was a pleasant time in Hamburg.

Andrei Rostovtsev and Alexandre Fedotov for guiding me into the framework of this analysis.

Too many people are involved into such large scale experiments, as this list could be complete. To all the colleagues and friends who helped me in many ways to complete this work: Thanks!

Curriculum vitae

<u>Personalien:</u>

Name	Beck
Vorname	Hanspeter
Geboren	19. 1. 1965 in Luzern
Bürgerort	Neuenkirch und Menznau LU

<u>Bildungsgang:</u>

1972 - 1978	Primarschule in Weggis LU, Wolfenschiessen NW und Dietikon ZH
1978 - 1980	Sekundarschule in Dietikon ZH
1980 - 1984	Mathematisch-Naturwissenschaftliches Gymnasium Rämibühl in Zürich
1984	Matura, Typus C
1984 - 1991	Studium der Physik (Mathematik, Astronomie) an der Universität Zürich
1989 - 1990	Diplomarbeit in Experimentalphysik
	Titel: Konstruktion, Bau und Inbetriebnahme einer computergesteuerten Gasmischanlage
1991	Diplom in Experimentalphysik
1991 - 1996	Wissenschaftliche Mitarbeit beim H1 Experiment am Elektron-Proton Speicherring HERA in Hamburg (DESY)
1996	Dissertation bei Prof. Dr. P. Truöl

<u>Dozentenverzeichnis:</u>

C. Amsler	P.F. Meier	G. Scharf
D. Brinkmann	H.H. Müller	H.R. Schwarz
E. Brun	U. Niederer	J.O. Stenflo
B. Derighetti	H. Nussbaumer	N. Straumann
R. Engfer	B.D. Patterson	U. Straumann
R. Holzner	R.E. Pixley	K. Strebel
W. Jaus	H. Pruys	A. Thellung
H. Keller	G. Rasche	P. Truöl
H.H. Keller	W. Reichert	F. Waldner
W. Kündig	J. Roos	D. Wyler